3.2 Å Cryo-EM Structure of Cyanobacterial Monomeric Photosystem I: Monomerization Unravels the Red Chlorophylls

(シアノバクテリアのモノマー光化学系Ⅰの 3.2Å クライオ EM 構造：モノマー化によって明らかになった長波長クロロフィルの構造)

MEHMET ORKUN ÇORUH

Graduate School of Science, Osaka University

February, 2021

3.2 Å Cryo-EM Structure of Cyanobacterial Monomeric Photosystem I: Monomerization Unravels the Red Chlorophylls

(シアノバクテリアのモノマー光化学系Ⅰの 3.2Å クライオ EM 構造：モノマー化によって明らかになった長波長クロロフィルの構造)

A Doctoral Thesis

By

MEHMET ORKUN ÇORUH

Submitted to the Graduate School of Science, Osaka University

February, 2021

ACKNOWLEDGMENTS

Even though this study includes a professional training and research by the nature of a Ph.D degree, it was very important to keep a peaceful state of mind in order to succeed. This accomplishment was very much dependent on the environment. I would like to express my deepest gratitutes to Professor Genji Kurisu for providing such a welcoming, peaceful and balanced environment and accepting me to his laboratory. As a keen observer of his communications and attitude, I did not only get a chance to experience a very well designed research that i dreamed of, but i also gained a role-model for my future interactions.

As a person coming from a physics engineering background, i had difficulties in adapting myself to biological experiments. Without the guidance and support of Professor Hideaki Tanaka, Professor Akihiro Kawamoto and Professor Christoph Gerle, it would be very difficult to enjoy the interdisciplinary merits of structural biology in such a short period.

This study, is a follow up of a long pursued research and I did the initial experiments with Professor Hisako-Kubota Kawai, who was a former PhD in this laboratory. I would like to thank her and Yuko Misumi who kindly helped me a lot both in grasping structural biology experiments and learning the lab environment, for their time and kind support. Secretaries in our laboratory Miho Tsutsui, Kazuko Shimoke and Satoe Tomita were very helpful in every aspect of daily life and learning about the rules of a different country, making life in Japan much easier for me.

A part of my study was conducted in Ruhr University, Bochum, where I was a visitor for one month. I would like to express my gratitutes to people of Nowacyzk laboratory, specifically Anna Frank and Professor Marc Nowacyzk for their hospitality. Also, I had the rare chance of meeting one of the initiators of this long study, Emeritus Professor Matthias Rögnar and learn from his wisdom. It was an honor for me to be able to make scientific discussions with him. Our colloborators Professor Takayuki Kato and Professor Keiichi Namba made it possible to finalize our structural analysis with their kind support in cryo-EM measurements.

My collegues Nam Ratana, Jiannan-Li, Linda Juniar, Rei Toda, Yusuke Ohnishi were the excellent coworkers to find around while doing such a heavy research with their helpfulness and friendliness. I feel the urge to share this graditute with all the members of Kurisu lab.

If my friends Jen Neumann and Seolmin Ko, in addition to out-of lab friends Steffen Bach and Marvin Arens were not in my life, it would not be possible to deal with the regular life of a PhD student.
Most importantly, my dear family Orkide, Orkud, Nimet and Ula Çoruh will always have my gratitute for their never ending support to fulfill my dreams, and more importantly making me what I am.
I hope with the power of this rich support, this study will make at least a small contribution to the understanding of nature and a more peaceful world.

Signature

Orkun Çoruh

Feburary, 2021

CONTENTS

PAGE

INDEX OF FIGURES

PAGE

INDEX OF TABLES

PAGE

SYMBOLS AND ABBREVATIONS

µ	Micro
Å	Angstrom
µl	Microliter
ml	Milliliter
M	Molar
mM	Millimolar
µM	Micromolar
^{o}C	Celcius Degrees
Da	Dalton
KDa	Kilodalton
kV	Kilovolt
PSI	Photosystem I
PSII	Photosystem II
$NADP^{+}$	Nicotinamide adenine dinucleotide phosphate
NADPH	Dihydronicotinamide adenine dinucleotide phosphate
FNR	Ferredoxin-$NADP^{+}$ reductase
Chl	Chlorophyll
Bcr	Carotenoid
WT	Wild type
SDG	Sucrose Density Gradient
HPLC	High Performance Liquid Chromatography
mg Chl^{-1}	Per milligram of Chlorophyll
ml h^{-1}	Militer Per hour
s	Second
m	Minute
A.M.	Absorption Maximum
MGDG	Monogalactosyldiacylglycerol
DGDG	Digalactosyldiacylglycerol
SQDG	Sulfoquinovosyl diacylglycerols
PG	Phosphatidylglycerol

CHAPTER I.

PROTEINS THAT CHANGED THE PLANET

1 INTRODUCTION

The fact that photosynthesis has a remarkable effect on the transformation of Earth from an inhabitable planet to the terrene cultivating the life and synergy of a diversity of species has inspired many questions and research activities in Earth sciences[1,2], geoscience[3], biology[4,5], chemistry[6,7], physics[8,9], engineering[10,11] and even space sciences[12,13]. Temporally tracing the energetic processes furnishing the life shows that oxygenic photosynthesis virtually transformed an oxygenless atmosphere into an oxygen containing one, shaping all the environmental conditions. Before this transformation, instead of relying on the oxygen-water cycle, existing organisms were osculant to other molecules in an austere anaerobic biochemistry. The appearance of O_2 in the atmosphere approximately 2.4 billion years ago, radically changed the red-ox balance on Earth, and organisms faced extinction in case they failed to adapt to oxygen or retreat to anaerobic ecological niches[14]. However, with an evolution towards tolerating O_2 and eventually to employing the enormous amount of energy available upon using it as a terminal oxidant, organisms greatly expanded their repository of metabolic processes[15,16].

Photosynthesis is the conversion of light energy into chemical energy stored in the chemical bonds of sugar molecules and is one of the most critical natural processes on our planet. While purple and green sulfur bacteria generate elemental sulfur making use of hydrogen sulfide and sunlight in the anaerobic form of photosynthesis, cyanobacteria, algae, and plants implemented an oxygenic variant to convert water and carbon dioxide to sugars and release oxygen as a by-product[17], producing almost all reducing equivalents of our biosphere and the oxygen needed to power life. Even though the real ancestor of photosynthetic bacteria, and thus the ancestor of its proteins' are not known, the accessible part of the evolution of these proteins is well-understood. Still ongoing discussions on the topic lead to the conclusion that a protein family called the "reaction center" is responsible for photosynthesis. Figure 1-1 shows a current model of the evolution and diversification of these proteins.

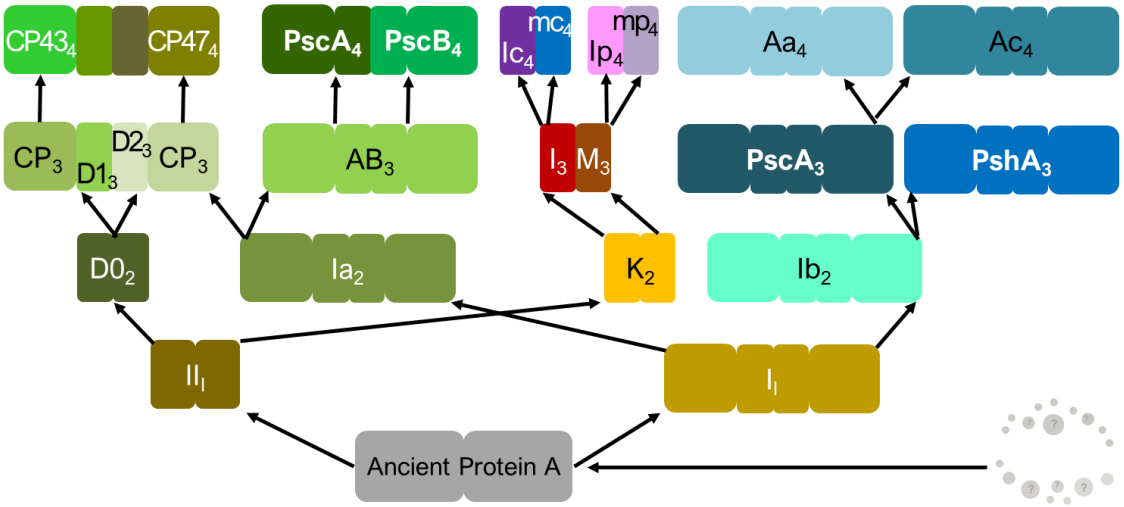

Figure 1-1 Schematics of Oxygenic and Anoxgenic Evolution of Reaction Center Proteins[18], spheres with question marks represent the earliest evolutionary events that led to the evolution of the chlorophyll and bacteriochlorophyll synthesis pathway and the first reaction center proteins. The subscript indicates transitional stages away from ancestral protein A

Recently, conventional anticipation is that the structure of this main engine was preserved over evolution of a long time. However many variations amongst the species have been discovered. These differences can supposedly be related to the "endosymbiotic hypothesis", showing that the machinery found in plants is a result of symbiosis, turning cyanobacteria to an organelle within the plant cell. As a result, lost genes and new adaptations result in new variations (Figure 1-2). Consequently, despite the similarities of the main concept, behavior, products, and the frame of action, there are some alterations at different levels between plant and cyanobacterial photosynthesis schemes. The process is known to be localized to thylakoid membranes and orchestrated by four main components embedded in the membrane (Figure 1-3).

The light energy necessary to ignite the process is harvested by two large pigment-binding membrane protein complexes identified as photosystem I (PSI) and photosystem II (PSII)[21]. PSI is a light-driven oxido-reductase chauffeuring the electrons from water-soluble plastocyanin or cytochrome c_6 on the lumenal side of the thylakoid membrane to ferredoxin or flavodoxin on the stromal side. This electron transfer facilitates the reduction of $NADP^+$ to NADPH by FNR for fixation of CO_2 aiding the procuration of the reductive pentose phosphate

cycle[22,23,24,25]. Although cyanobacterial PSI is in the thylakoid membrane was also observed to exist in monomeric and dimeric forms, its usual oligomeric state is trimeric[26,27,28]. The occurance of PSI in plants and algae strictly in monomeric form and is regarded as an outcome of symbiotic evolution that provides the benefit of the capability of attachment of light harvesting complexes as external antenna, to deal with variable light conditions. [29,24].

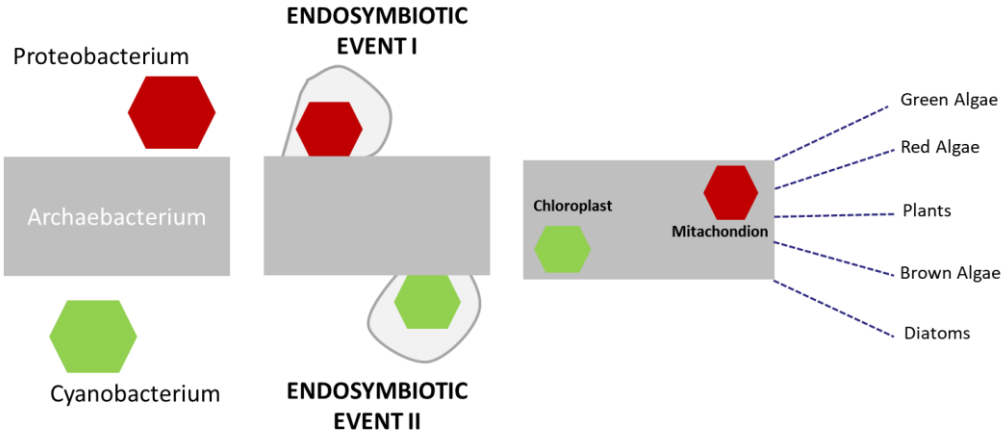

Figure 1-2 Proposed Schematics of The Endosymbiotic Event[19]. The different endosymbiotic events in a predicted order. Cyanobacterium is transformed into "Chloroplast" (green box) and Proteobacterium is transformed into "Mitochondria" (red box).

Even though the reason and mechanism behind this change are not yet fully understood, this remarkable difference in oligomeric states and mode of light harvesting has been the framework of several molecular scenarios in the evolution of photosynthesis from its beginning in cyanobacteria ~3 billion years, over algae to the emenation of plants on land[30,31]. Yet, the advantage of monomeric structure over oligomeric structures is not clear. The structure of cyanobacterial trimeric PSI from *Thermosynechococcus elongatus* (hereafter referred to as trimer crystal structure) was revealed at 2.5 Å resolution almost two decades ago[28], providing a detailed description of almost all of its amino acid residues and bound ligands. One monomer of a PSI trimer consists of 12 protein subunits; PsaA, PsaB, PsaC, PsaD, PsaE, PsaF, PsaI, PsaJ, PsaK, PsaL, PsaM, and PsaX, 96 chlorophylls, more than 20 carotenoids, four structural lipids, and three [Fe_4S_4] iron-sulfur clusters. A trimer has a total molecular mass of 1,080 kDa. The chlorophyll content consists of two functionally distinct groups. The first

group is consists of six chlorophylls of the electron transfer chain (ETC) including the special pair chlorophylls Chla and Chla' (P700) and is involved in electron pumping. The rest of the chlorophylls are defined as the light harvesting antenna and are engaged in excitation energy transfer as well as light capturing. The antenna chlorophylls are organized into the chlorophylls of the core and the peripheral antenna with respect to their positions. Peripheral chlorophylls are arranged as lumenal and stromal side networks. Unlike chlorophylls, the carotenoids of PSI do not populate the periphery of the protein and the core of the complex and traverse the transmembrane region between lumenal and stromal sides.

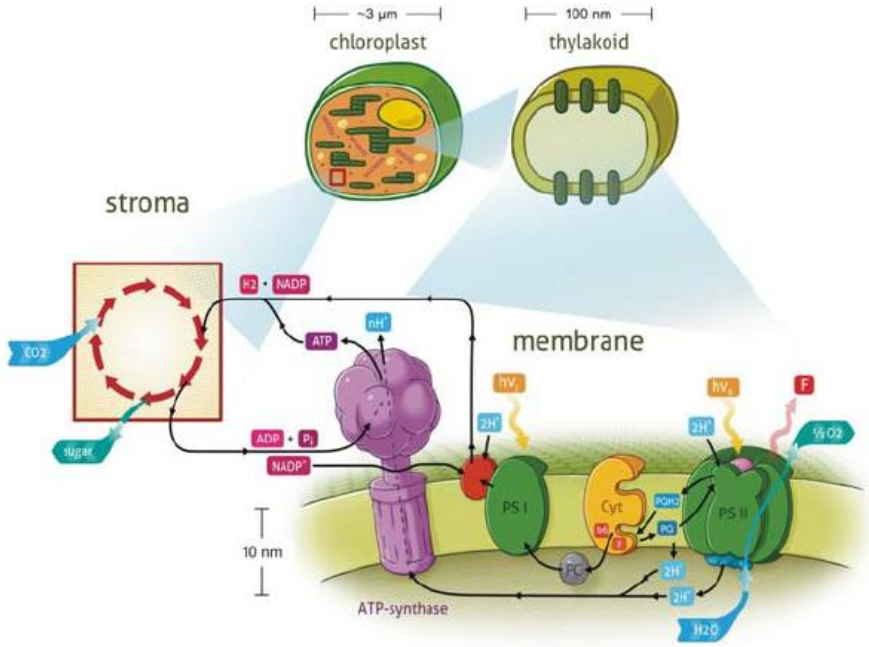

Figure 1-3 Spatial Organization of The Main Photosynthetic Apparatus[20], light harvesting PSI and PSII are shown in dark green since the chlorophyll molecules they involve is the reason of the green color of chloroplasts.

Once the positions of the cofactors and geometry of the protein was resolved, more precise studies detailing the harvesting of light, designation of the excess energy, transfer of excitation energy and charge seperation, become possible[32]. Nevertheless, despite the overall mechanism is well understood, there are still controversy about some prospects. This overall mechanism is explained by a model of the system, founded on the electron pumping function and mechanism of PSI from reduced plastocyanine or cytochrome c_6 to ferredoxin or

flavodoxin[25,33] and explains how light is captured by the chlorophylls, how the resultant excitation energy is transferred to other chlorophylls by Förster Resonance Energy Transfer (FRET)[34] along with the uphill and a downhill transfer pathways[38], how the excitation energy induces the electron transfer from special pair to ferrodoxin through iron sulfur clusters, and how the special pair chlorophylls return to their ground state by taking the electron transferred from the luminal docked plastocyanin[35]. This intricate organization allows an efficiency close to unity [pumping of nearly one electron per harvested one photon]. is highly dependent on time. Specific mechanisms of temporal control have been developed for keeping the lost photon energy at minimum levels like trapping the excited energy in some locations for a period of time (red chlorophylls: chlorophylls with red-shifted absorption spectra), or quenching the excess energy (carotenes). Additionally, PSI is capable of using energy from wavelengths different than chlorophyll a absorption[36], and this is attributed to the presence of carotenoids and red chlorophylls[37].

One important aspect of oligomeric states and the possible structural differences between them stems from the observation that monomeric and trimeric PSI from the same species may have differences in the long wavelength absorption[50,51,52]. The long wavelength absorption describes the absorption of light with a lower energy than that of the special pair chlorophylls, and naturally includes an uphill transfer of the energy gained from the long wavelength photon. The entities promoting PSI with this extraordinary ability are termed “'Red' chlorophylls” or “long wavelength chlorophylls”. Accomplishing the absorption from longer wavelength is observed by either differantiation in pigment structure or a specific organization and clustering of pigments. The uphill transfer of energy from these lower energy sinks is supposedly alleviated by the vibrational energy from the environment and actuates the oxidation of P700 by photons with a wavelength beyond 700 nm. Photosynthetic organisms benefit from this as an effective expansion the light spectrum available for electron pumping[53,54,55]. To date, at least three discrete bands of long wave-length absorption at 708 nm, 715 nm, and 719 nm of PSI has been identified by spectroscopy[56,57,58]. An example of differentation in pigment structure is reported for *Halomicronema hongdechloris* as a divergence of a portion of the chlorophylls as chlorophyll *f*[59], which in

principle can be identified in high-resolution structures[42,43,60]. However, PSI of *T. elongatus* contains only chlorophyll *a*, and the long wavelength absorption is hypothesized to be tuned by their local chemical environment and close range interactions. Thus, direct structural observation of the 'red' chlorophylls in PSI of *Thermosynechococcus elongatus* is not possible.

In addition to the questions about the physiological necessity of monomeric PSI, the lack of understanding in the details of the mechanisms of PSI function despite the high resolution oligomeric structures and aforementioned observable differences between monomeric and trimeric PSI resulted in a long-standing interest in the isolation, biochemical characterization, spectroscopic analysis, and high-resolution structure determination of monomeric cyanobacterial PSI. However, to date, with a notable exception of the PSI monomer structure from *Synechocystis sp.* PCC 6803 solved at 4.0 Å resolution by X-ray crystallography[39], all structures of cyanobacterial PSI[28,40,41,42,43] have been determined from trimeric complexes or the recently discovered tetrameric PSI from *Anabaena sp. PCC 7120* and *Chroococcidiopsis sp. TS-821*[44,45,46,47]. This situation implies hindrance in both the purification of monomeric PSI and the growth of well-ordered 3D crystals for high-resolution structure determination.

Concurrently, cryo-electron microscopy (cryo-EM) technique emerged as a breakthrough with the ongoing 'Resolution Revolution', liberating a huge number of specimens from the necessity of crystallization[48]. As a result, structure determination of large integral membrane protein complexes became feasible even without crystals. Furthermore, the ability of cryo-EM single particle to solve structures of soluble and membrane proteins using relatively inexpensive 200 kV cryo electron microscopes is now well established[49,]. A detailed structural analysis of monomeric PSI may permit not only a better understanding of the mechanism and biological meaning of PSI oligomerization, but also render insights in indeterminate details of PSI function.

In this study, the aim was to achieve a complete structural analysis of monomeric PSI from cyanobacteria. *Thermosynechococcus elongatus* is chosen as the source due to vast amount of literature about its trimeric and monomeric forms PSI. The fact that trimeric PSI from the same species is resolved at 2.5 Å makes a comperative analysis attainable. Moreover, the thermophilic character grants

the proteins with stability. Two prominent structural biology methods, cryo electron microscopy and X-ray crystallography were utilized for complementary analysis. Two different purification methods were used to acquire the best possible sample quality and high yield necessary for high resolution analysis. Purified proteins are assessed by denaturing and native electrophoresis, mass spectrometry, negative stain electron microscopy and crystallization and behavior is investigated by UV-VIS and fluorescence spectroscopies as well as the activity measurements.

The aim is revealing the structure of a PSI monomer seperated from a trimer and observe the structural differences and potentially disorders of the structure induced by the disturbance of the process. The structural differences will be used to find clues about identities of red chlorophylls, oligomerization mechanism and evolutionary selection of monomeric state in plants.

The purification methods used in this study will be referred as Protocol I and Protocol II hereafter. Proteins obtained by both methods were crystallized, however crystals diffracting to relatively high resolutions were only possible to grow from the purification by Protocol I. These crystals were used to build a model at 6.5 Å resolution. The proteins obtained by the second purification were investigated by single particle cryo electron microscopy and were used to build a model at 3.2 Å resolution. The outcomes of this research are organized into six chapters, each focusing on introduction and background, purification and sample quality, X-ray analysis, cryo-EM analysis, structural outcomes and conclusions, respectively.

CHAPTER II.

ISOLATION OF PHOTOSYSTEM I MONOMERS

2 ISOLATION AND BIOCHEMISTY OF MONOMERIC PHOTOSYSTEM I

2.1 Introduction

Bacteria capable of oxygenic photosynthesis are termed “Cyanobacteria”. There are over 1500 species with a diversity of morphologies and species-specific characteristics such as cell movement, cell differentiation, and nitrogen fixation. Amongst the cyanobacteria, some of them are equipped to survive in extreme conditions, like unicellular rod-shaped cyanobacterium *Thermosynechococcus elongatus* strain BP-1[61] that inhabits hot springs and has an optimum growth temperature of approximately 55 °C. According to the phylogenetic analysis of Honda *et al*. using 16S rRNA sequences, “*T. elongatus* is branched very close to the origin of cyanobacteria.”[62] It is a photoautotrophic organism accomodating chlorophyll *a*, carotenoids and phycocyanobilin as pigments, and is accepted as a model organism for the study of photosynthesis[63,64,65]. It is one of the few cyanobacterial organisms that allows transformation by electroporation, an aspect indicating the ability of this organism to undergo natural transformation making it possible introduce exogenous DNA into the cell[66]. The regulation of the physiological activities in *T.elongatus* is also very well understood, providing a comprehension of its response to light conditions and temprature[67]. Modulations in the saturation, content and the organization of their membranes as the aftermath of temprature variations[68] has already been reported as well as its mechanism of detecting the light[69]. Moreover, photosystem I and II complexes from this organism have successfully been crystallized and analyzed by X-ray diffraction[28,63].

In order to define an isolation strategy, identifying the location of PSI is crucial. Aa mentioned before, the photosynthetic machinery is located in the thylakoid membranes. The structure of the thylakoid membrane has been identified with microscopy and is visualized in Figure 2-1.

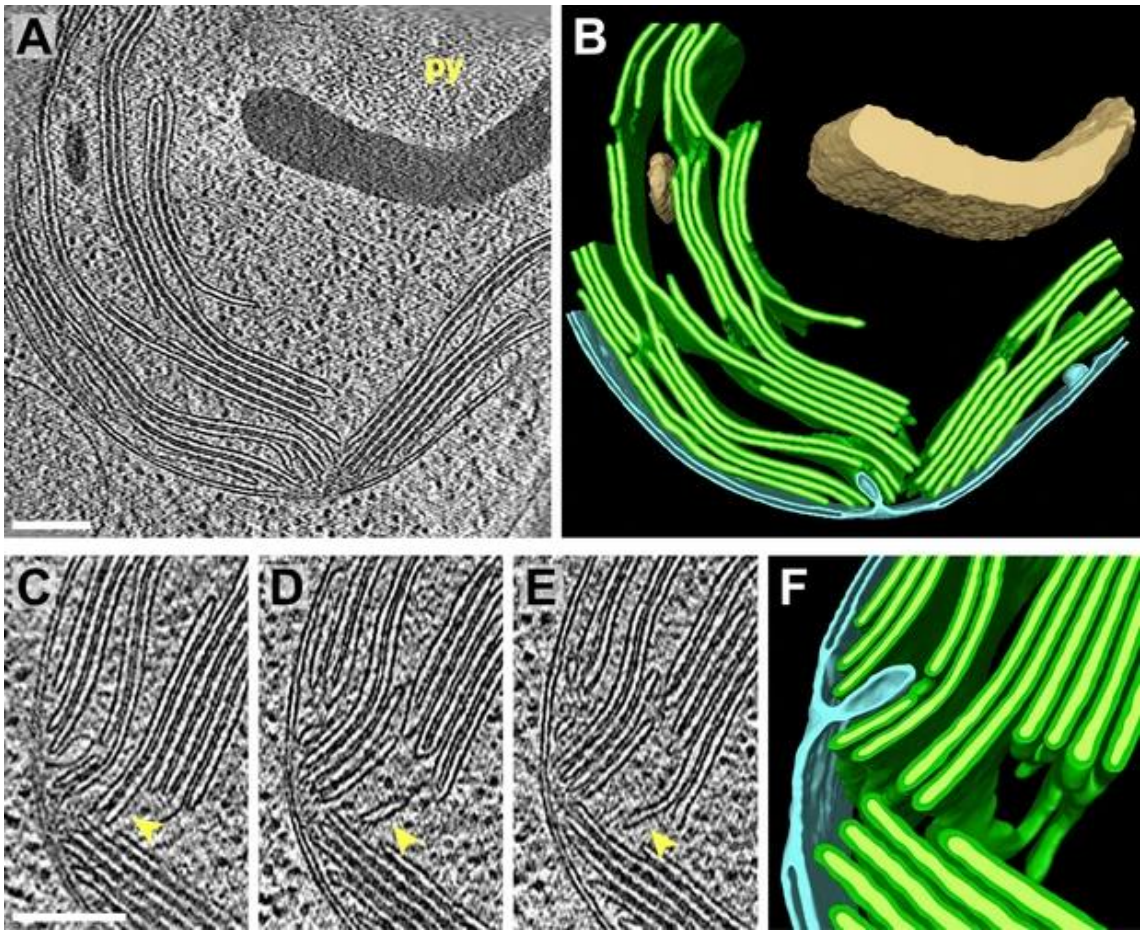

Figure 2-1 3D Organization of thylakoid membrane in chloroplast of *Clamydomonas Reinhardtee* [198], (A) A slice from the volüme (B) Visualization of thylakoid membrane (C-E) Three sequential slices from the volume and (F) another 3D segmentation showing the thylakoid in green.

It has also been reported that cyanobacteria change the thylakoid membrane organization and architecture depending on the protein content as a measure of inurement to environmental conditions. Change of the membrane structure depending on the phycobilisome content is shown in Figure 2-2.[71]

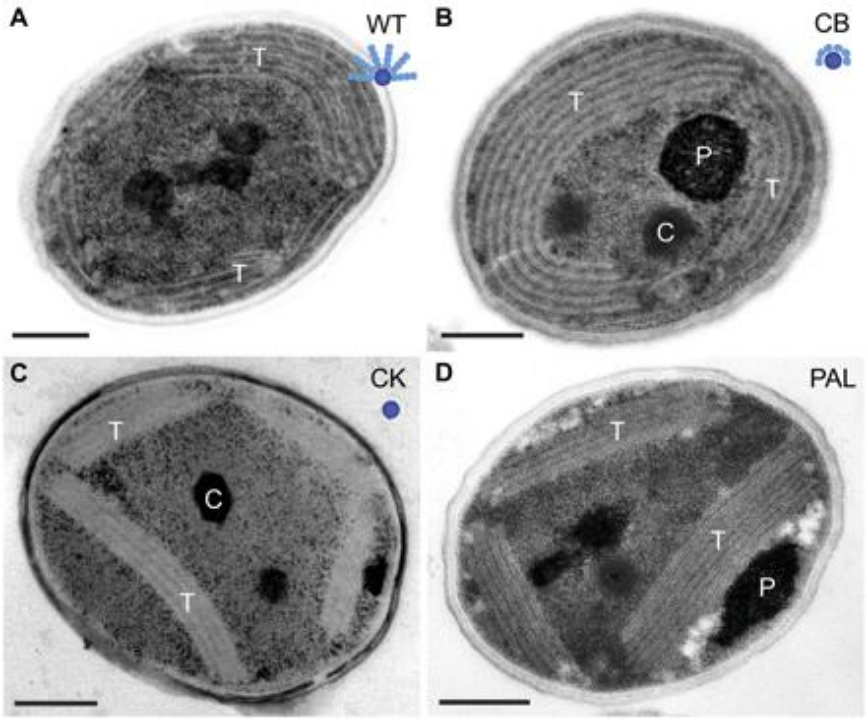

Figure 2-2 Changes in The Organization of Cyanobacterial Thylakoid Membrane[71](Material is copyright by the American Society of Plant Biologists.), A Wild-type (WT) cyanobacteria intact phycobilisomes. B, C, D, Mutants with less or non-intact phycobilisome content. Labeled are thylakoid membranes (T), polyphosphate bodies (P), and carboxysomes (C). A cartoon model of the phycobilisome structure in each strain is shown as an inset. Bars = 250 nm.

The differences between plant-type photosynthesis and bacteria-type photosynthesis incorparate the thylakoid membranes framework from amino acid level to bilayer level. Cyanobacterial thylakoid membrane is a simpler organization of layers paralleling the contour of the cells, whereas in the plants it is organized in a much more complex manner as grana and lamellae structures[72]. With the emergence of a variety of high resolution visualization tools, observation of the thylakoid membrane at the molecular level is possible. A recent study of Zhao *et al.* [73] investigates the topology of cyanobacterial thylakoid membrane using atomic force microscopy and clearly shows the organization of photosynthetic proteins and their oligomeric abundance in Figure 2-3. This study revealed how abundant monomeric PSI is in the thylakoid membrane, and moreover, the IsiA-PSI monomer complex formation is an important finding that proves the physiological significance and functionality of the monomers (Figure 2-3 g).

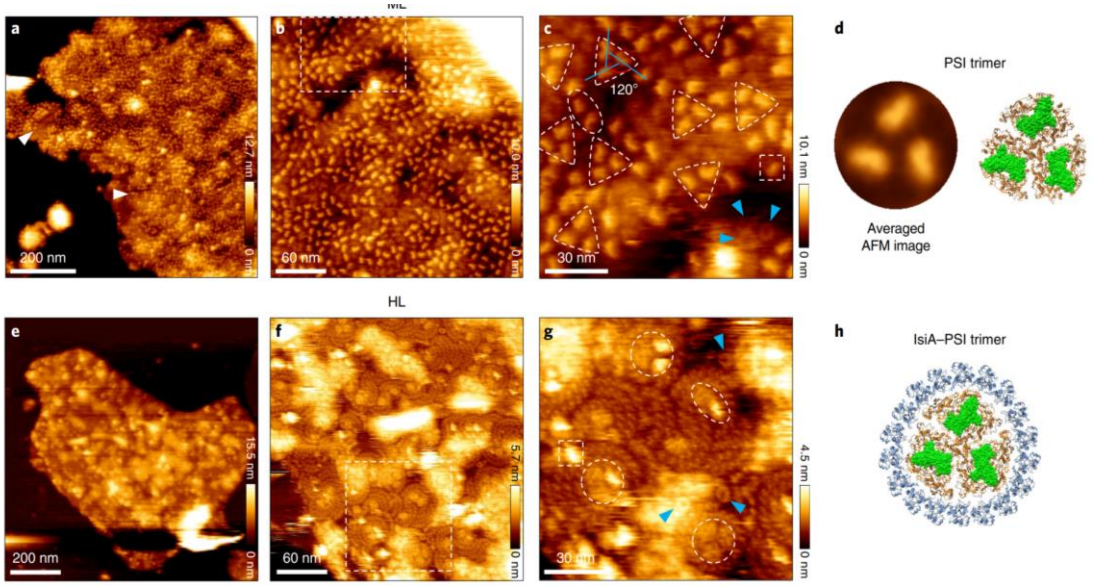

Figure 2-3 Atomic Force Microscopy Topographs of Cyanobacterial Thylakoid Membrane[73] a, AFM topograph of medium light adapted thylakoid membrane fragment the densely packed photosynthetic membrane proteins. Structures with ordered organization are indicated by arrowheads. b, AFM image of the cytoplasmic surface of a thylakoid membrane. The white box is shown in c. c, The trimeric (triangle), dimeric (oval) and monomeric (square) PSI complexes. Small ring-like structures, speculated to be ATPase membrane domains, are indicated by blue arrowheads. d, Threefold symmetrized and correlation-averaged AFM topograph of PSI from the cytoplasmic surface of thylakoid membranes (left). Atomic structure of the trimeric PSI complex from the cytoplasmic surface (right, PDB: 1JB0). e, Topograph of high light adapted thylakoid membrane fragment. f, High-resolution AFM image of the cytoplasmic surface of thylakoid membrane. The white box is shown in g. g, The trimeric (circle), dimeric (oval) and monomeric (square) PSI complexes in more detail. Small ring-like structures highlighted with blue arrowheads, speculated to be ATPase membrane domains. h, Atomic structure of the IsiA−PSI supercomplex from the cytoplasmic surface (PDB: 6NWA). Representative AFM imaging was derived from a minimum of five biologically independent membrane preparations.

Current level of knowledge shows how the condition, content and organization of the membrane changes easily in order to adapt to environmental conditions. So in order to succesfuly purify a protein, controlling the condition of the thylakoid membrane at the culture period is of utmost importance.

Extraction of the proteins out of their embedding membrane is the second step. This is usually achieved by a detergent treatment. In order for proteins to be released from the membrane, lipids of the membrane should be replaced by some molecules to protect the hydrophobic parts from solvent. The organizational behaviour of detergent molecules is the key to success in this process. The

choice of the detergent molecule is critical to provide the protein a similar environment to the membrane, for better stability.

Lipid content of cyanobacterial membranes is mostly glycolipids. The majority of the thylakoid and cytoplasmic membrane lipids are MGDG, DGDG, SQDG and PG as the inner envelope membranes and thylakoid membranes of chloroplasts in higher plants[74]. This knowledge is very useful in designing the purification experiments. However, detergent treatment does not specifically extract a particular protein, instead most components embedded in the membrane are extracted. After securing the stability of the proteins by the solubilization, it is usually crucial to make additional seperations. It is possible to achieve this by using the specific properties of a protein like metal affinity, size, electrical charge or hydrophobicity[75].

The rich scientific literature on isolation procedures show that purification of a PSI monomer is a delicate scientific problem which needs a careful design. Past experiences in the Kurisu laboratory and related literature shows that yields of monomer isolation are not as high as trimer isolation. The reason is not well understood yet. Studies about PSI monomers show that many approaches were applied to increase the yield. These can be listed as;

- Changing growth conditions[24]
- Using genetic tools[39,76,77,78]
- Physically breaking trimers into monomers[79]

To keep the protein as intact as possible, in its native state and physiologically active, breaking the trimers into monomers was chosen as the most promising strategy in this study. The method explained in El-Mosnawy *et al.* paper (Protocol I) and a new method developed in the Molecular Mechanisms of Photosynthesis Laboratory of Ruhr University Bochum (Protocol II) were chosen and both protocols were adapted to structural analysis aim.

2.2 Materials and Methods

2.2.1 Cell Culture and Purification

In this study, two methods were applied for purification. These methods will be referred as Protocol I and Protocol II hereafter. Protocol I is designed for His-

tagged PSI to use metal affinity chromatography. In Protocol II, wild type cells are used. For both protocols, cultivation procedure is the same and is summarized in Figure 2-4. The ingredients for culture medium are shown in Table 2-1 and 2-2. For incubation of culture, a Panasonic MLR-352 incubator set to 50 °C was used with a TAITEC NR-2 rotary shaker and a NISSIN SLQW SW600 N-1 stirrer, both set to 120 min^{-1} frequency inside the growth chamber. Rotary shakers are used in small and medium scale culture, stirrers are used for large scale culture. In the Large Scale Culture II step, continious bubbling with 2% CO_2 was provided to the culture bottles through a MVP-751 pump from Asahi Techno Glass and a Hitachi Oilfree Bebicon bubbling system.

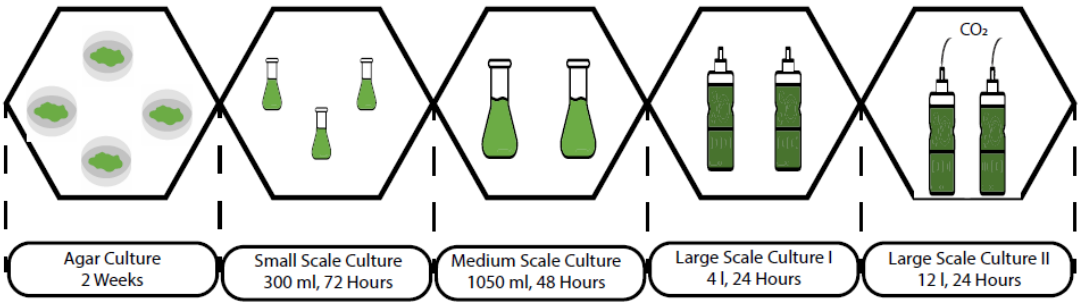

Figure 2-4 Culture Workflow for Both Types of Cells Used in This Study.

Table 2-1 Stock Solutions for Cultivating *Thermosynechoccus elongatus*

SOLUTION NAME	INGREDIENT	AMOUNT
Iron Solution	$FeNH_4$ citrate	57 mM
	Na citrate	0.8 g/100 mL
	Na EDTA	1.25 mM
BG-FPC	$NaNO_3$	1.76 mM
	$MgSO_4.7H_2O$	30.43 mM
	$CaCl_2.2H_2O$	24.49 mM
	Na citrate.$2H_2O$	3.12 mM
	Na EDTA (pH=8.0)	1.12 mL/lt from 0.25 M solution
	Trace Minerals	%10 (v/v)
Trace Minerals	H_3BO_3	46.3 mM
	$MnCl_2.4H_2O$	9.2 mM
	$ZnSO_4.7H_2O$	772.1 µM
	Na_2MoO_4	1.6 mM
	$CuSO_4.5H_2O$	316.4 µM
	$Co(NO_3)_2.6H_2O$	169.8 µM
-	K_2HPO_4	175 mM
-	Na_2CO_3	190 mM
-	HEPES pH:8.2	1 M
-	TES-KOH pH:8.2	1 M

Table 2-2 Buffers for Cultivating *Thermosynechoccus Elongatus*

CULTURE MEDIUM		INGREDIENT	AMOUNT
Liquid BG11		BG-FPC	20 ml
		Iron Solution	3 ml
		Na_2CO_3	2 ml
		K_2HPO_4	2 ml
		HEPES	10 ml
		MilliQ	Fill to 2 liters
Solid BG11*	Bottle A	BG-FPC	10 ml
		Iron Solution	1 ml
		Na_2CO_3	1 ml
		K_2HPO_4	1 ml
		TES-KOH (pH=8.2)	10 ml
		MilliQ	Fill to 500 ml
	Bottle B	Bacto Agar	15 g
		Na-thiosulphate	3 g
		MilliQ	Fill to 500 ml

**After autoclaving, Bottle A and Bottle B are mixed and transferred to plates.*

In Protocol I, PSI trimers were monomerized in the thylakoid membrane after isolation of the membrane, by an ammonium sulfate and heat treatment. After monomerization, an extraction with β-DDM was applied at room temprature. Solubilized proteins were seperated first by metal affinity chromotography (hand made column with Ni-NTA Sepharose from Qiagen) to yield in monomeric and trimeric proteins. A sucrose density gradient was used to seperate monomers and trimers. After a PEG precipitation step, the buffer was exchanged by a spin-down and resuspension step. The resulting proteins were used for crystallization. For all steps involving ultracentrifugation, a Beckman Coulter Optima L-90K Ultracentrifuge and for other cetrifuges, a Beckman Coulter Avanti HP-20 XP Centrifuge were used with the relevant rotors. The workflow of this protocol with the buffer contents is shown in Table 2-3.

Table 2-3 Flowchart of Protocol I

Cell Distruption and TM Isolation	• Lysozyme Treatment [90 mins, 40 ◦C] • Parr bomb, [13 Mpa, N_2 atmosphere, 30 mins] • Washing [Buffer 3 x3, Buffer 4 x2, 8000 rpm, 15 mins, 4 ◦C]
Monomerization	• Resuspension in Buffer 6 [1 mg chl/1 ml Buffer 6] • Water bath, [20 mins, 50 ◦C, Dark] • Cooling to room temprature
Solubilization	• Extraction [%0.6 β-ddm] • Incubation [60 mins, 20 ◦C, dark] • Ultracentrifuge [1 hour, 18000 g, 4 C]
PSI Isolation	• Sample-Ni-NTA mixture [60 mins, dark, rotary shaker, 20 ◦C] • Precipitation [26000 g,15 minutes, 4 ◦C, PEG] • Resuspension in Buffer 4 [%0.4 β-ddm]
Oligomeric Seperation	• Sucrose linear gradient • Ultracentrifuge [36000 g, 13-16 hours, 4 ◦C]

This method provided monomers, but the yield was not enough to establish systematic crystallization experiments. In order to improve the yield, the bead

beater method for cell disruption was tested, but the increase in the resulting protein amount was not significant. It is notable that the size difference of thylakoid membranes extracted with both methods differ, and the resulting surface area difference changes the solubilization dynamics and thus the necessary amount of detergent has to be recalibrated in this regard. Additionally, the smaller sized membrane particles produced by the bead beater method necessitates a change in the centrifuge conditions in the washing step.

In order to improve the yield, Protocol II was established. The method is transferred from my collaborators in the Molecular Mechanisms of Photosynthesis Laboratory (Nowacyzk Laboratory), Ruhr University Bochum, Germany[80]. Although this method improved the yield, it did not result in better crystals compared to the ones obtained using the former protocol. In order to get better crystals, the protocol is redesigned with some minor modifications on methods and the buffers. The protocol and the adjustments are summarized in Table 2-4. For the centrifuge after solubilization a Hitachi Micro Ultracentrifuge C5100FNX, for sucrose density gradients, a Hitachi CP80WX and for other cetrifuges a Beckman Coulter Avanti HP-20 XP Centrifuge was used with the relevant rotors. For hydrophobic interaction chromatography, Thermoscientific HIC POROS 50 Resin in a Waters AP-2 column was used in ÄKTA Explorer system with a Unicorn 5.31 software and for desalting, a Hi-prep 26/10 Desalting column attached to ÄKTA Purifier was used.

Table 2-4 Workflow for Protocol II and Optimizations

	ORIGINAL PROTOCOL	OPTIMIZED PROTOCOL
Cell Distruption and TM Isolation	• Lysozyme Treatment [90 mins, 37 ◦C] • Parr bomb, [12 Mpa, N_2 atmosphere, 30 mins] • Washing [8000 rpm, Buffer]	• No changes
Phycobilisome Elimination	• Pre-extraction [%0.05 β-ddm, Buffer B] • Centrifuge, [30 mins, 13000 rpm]	• β-ddm removed from the procedure.
Solubilization	• Extraction [%0.5 LDAO, extraction buffer, C= 1 mg Chl/1ml] • Incubation [30 mins, 20 ◦C] • Ultracentrifuge [1 hour, 42K rpm, 4 ◦C]	• Ca not used in the buffers.
Carotenoid Elimination	• Sucrose Step Gradient* [(%14 sucrose,45 ml) + (%80 sucrose,5 ml)] • Ultracentrifuge [32.5K rpm, 18 Hours, 4 ◦C]	• Ca not used in the buffers. • Step gradient changed to linear gradient. • Detergent of SDG changed to LDAO from β-ddm • Upper and lower bands collected and treated as different samples.

Hydrophobic Elimination	• Concentration to 10-20 ml. • Ammonium sulfate treatment [%65 AMS buffer + %35 sample] • Hydrophobic Interaction Column	• AMS concentration optimized to 1 molar in sample, 1.5 M in HIC buffer • Centrifuge step after treatment to eliminate phycobilisomes • Ca not used in buffers
Desalting	• Concentration to 10-20 ml • Desalting column	• No changes

** There are four bands. Upper and lower green bands are collected and mixed, the rest is discarded here.*

Differences between Protocol I and II can be listed as;

- Monomerization procedure: In Protocol I, thylakoid membrane is treated with ammonium sulfate, in Protocol II, extracted proteins are treated with ammonium sulfate.
- Density Gradient : In protocol I, purified proteins are applied to density gradient as a last seperation method. In Protocol II, solubilized proteins are applied to density gradient an even though there is a seperation in the green bands, after removal of caretenoids, phycobilisomes and other small proteins, these green bands are mixed again.
- Solubilization detergent is β-DDM in Protocol I and LDAO in Protocol II. During the HIC column, detergent is exchanged to β-DDM again.
- Protocol I includes heat treatment to thylakoid membranes. All protocol II experiments are held at room temprature or 4 ◦C in Protocol II.

The changes in Protocol II can be listed as;

- In order to minimize unknown interactions, the pre-extraction step was changed and the only detergent in contact with the proteins until the HIC column is LDAO.

- Sucrose density gradient is redesigned as a linear gradient instead of a step gradient to improve the seperation. The detergent used in the gradient is changed from β-DDM to LDAO with the same reason. To minimize possible heterogeneity, resulting upper (possibly native PSI monomers and PSII dimers) and lower green bands (PSI trimers) are collected seperately. Instead of mixing, they are applied to HIC column as different samples.
- Ca^{+2} ion is removed from the ingredients of all purification buffers.
- Ammonium sulfate concentration both in high salt buffer and HIC column buffer were optimized to the minimum molarity that the seperation can work.

2.2.2 Characterization

2.2.2.1 Blue native polyacrylamide gel electrophoresis (BN-PAGE)

Blue native polyacrylamide gel electrophoresis experiments were designed as explained in the standard protocol[167] to identify PSI proteins and their final oligomeric state as well as their purity. Novex NativePAGE Bis-Tris Gels Kit with 3-12% Bis-Tris content were used for experiments. After the addition of BN-sample buffer (50 mM BisTris, 6 N Hcl, 50 mM NaCl, 10% (w/v) Glycerol, 0.001% (w/v) Poinceau S) to the samples, they were applied on the gel and separated in an electric field at an initial voltage of 100 V. The inner gel chamber was initially filled with blue cathode buffer (50 mM Tricine, 15 mM Bis-Tris, 0.02% (w/v) Coomassie BB G-250), while the outer space contained anode buffer (50 mM Bis-Tris). After 30 min, the blue cathode buffer (containing Coomassie Brilliant Blue G250) was exchanged with clear cathode buffer (50 mM Tricine, 15 mM Bis-Tris) to discolor the gel. The voltage was raised to 150 V for about one hour until an adequate separation of the protein bands was achieved.

2.2.2.2 SDS-PAGE

To analyze the subunit composition of the isolated proteins, the standard method of polyacrylamide gel electrophoresis was carried out as described previously[168]. The samples were mixed with SJ-sample buffer, heated at 60 °C for 30 min, and, after a short centrifugation, applied on the polymerized SDS gel. Separation was achieved in an electric field at a voltage of 100 V in one hour.

2.2.2.3 UV/Vis Spectroscopy

The absorption spectra of *T.elongatus* PSI monomer and trimer were measured via UV-2450 spectrophotometer (SHIMADZU) in the range between 300 nm and 750 nm in Nowacyzk Laboratory of Ruhr University Bochum. In an additional UV-VIS measurement was done in Kurisu Laboratory of Osaka University with a JASCO-V630 spectrophotometer in the same range with the same amount of proteins. This second measurement was done to understand if there were additional free pigments captured in detergent micelles and not bound to protein.

2.2.2.4 Fluorescence emission spectra at 77 K

Fluorescence emission spectra were measured with a JASCO FP-6500 spectrofluorometer in Nowacyzk Laboratory of Ruhr University Bochum. Trimeric and monomeric PSI complexes were diluted in buffer B with 0.03% (w/v) β-DDM to a final concentration of 120 µg/ml. Subsequently, the diluted samples were flash-frozen in liquid nitrogen and immediately used for the measurements. P700 excitation was achieved by an actinic light at 436 nm while fluorescence emission spectra were measured from 650 to 780 nm with a step size of 1 nm and a bandpass filter of 5 nm.

2.2.2.5 MALDI-Time of Flight (ToF)-Mass Spectrometry

The mass spectrometric analysis of the cyanobacterial PSI monomer and trimer was carried out with the Ultraflex III, MALDI-ToF/ToF-Mass spectrometer (Bruker) in Nowacyzk Laboratory of Ruhr University Bochum. Initially, the samples were treated with a saturated matrix solution of sinapic acid (sinapic acid in 0.1% (w/v) trifluoroacetic acid and 34% (v/v) acetonitrile). Sequantally, 2 µl of a 1:1, 1:5, and 1:10 dilution of purified samples with the matrix were applied on a Matrix Assisted Laser Desorption Ionization (MALDI) -ToF target and air-dried for 30 min. The isolated proteins were then ionized by the internal MALDI 200 nitrogen-laser, creating a 337 nm light pulse with an output power of 150 kW. By applying a high voltage, the mass of the peptides could be detected by their time-of-flight in the high vacuum.

2.2.2.6 Activity Measurements

Time-dependent oxygen consumptions PSI monomer and trimer were measured by a PST3 sensor (PreSensTM) with a FIBOX 3 oxygen electrode (PreSensTM) in Nowacyzk Laboratory of Ruhr University Bochum. For the measurement, 5 µg

Chl/ml of the protein samples were applied in 1 ml activity buffer (25 mM Hepes, 500 mM NaCl, 3 mM $MgCl_2$ and 330 mM Mannitol) with DCPIP and sodium ascorbate as sacrificial electron donors and methyl viologen as electron acceptor (final conc. NaAsc: 5 mM, DCPIP: 0.8 mM, MV: 0.5 mM). Thereby the sample mixture was prepared inside a tempered, opaque cuvette at 30 °C under constant stirring. After an incubation time of 2 min the measurement was started by switching on the measuring light (λ=680 nm) for 1 min. The oxygen consumption was calculated via the linear slope.

Spectroscopic, Maldi-TOF and activity experiments and related calculations are conducted in Nowaczyk Laboratory of Ruhr University Bochum, Germany as a part of the colloboration. Relevant results are also published in a master thesis[80], and will be published in a collaborative paper.

2.3 Results

In Figure 2.5 resulting sucrose density gradients after the ultracentrifugation are shown. Since the SDG of Protocol I is the last step of purification (Figure 2-5 left), the band sizes provide a rough idea about the monomer/trimer ratio.

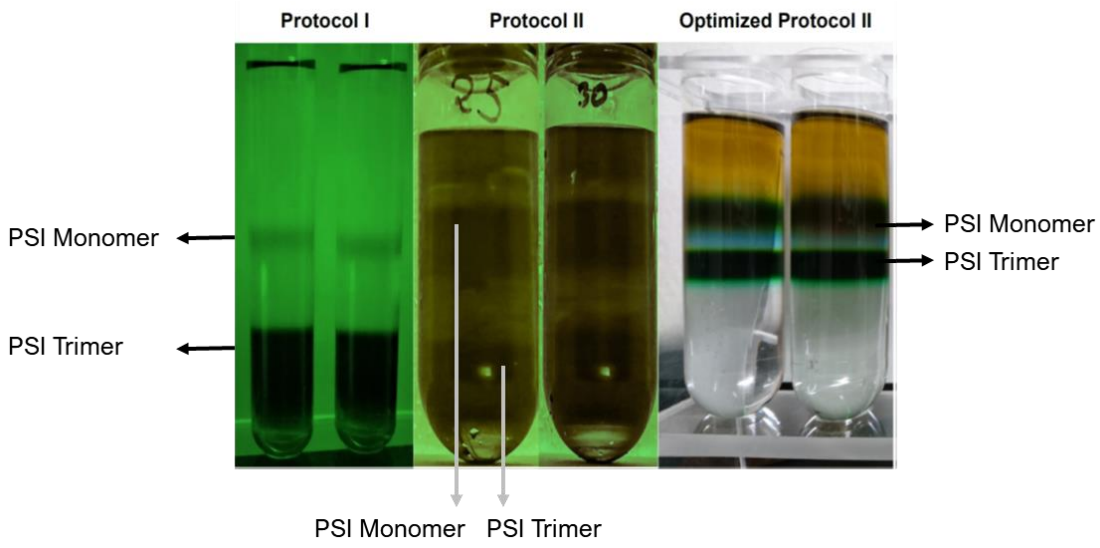

Figure 2-5 Comparisons of Sucrose Density Gradients From Different Protocols. The first SDG is the final seperation step of Protocol I. The second SDG is from Protocol II and is followed by mixing the darg green bands. The third SDG is from the optimized Protocol II and the green bands are purified seperately.

(Upper band monomer, lower band trimer) The SDG of Protocol II (Figure 2-5 middle) shows a larger amount of dark bands (band II and Band IV). In Protocol II, these bands are collected and mixed. Rest of the SDG is discarded. After the optimization of the SDG, resulting two green bands (Figure 2-5 right) are collected seperately and purified seperately.The SDG is followed by HIC column application in Protocol II. Sample chromatograms of the hydrophobic seperation are shown in Figure 2-6. In the panel a of Figure 2-6 , the chromatogram is from non-optimized Protocol II whereas panel b shows a chromatogram after optimizing the buffer conditions of chromatography to seperate the proteins better. In both of the experiments, used sample is a mixture of the green bands of SDG. Panels c and d show chromatograms from the final version of the Protocol 2, in which the buffer conditions of all experiment and SDG are optimized and the upper (panel c) and lower (panel d) bands of SDG are used as different samples. The chromatogram consists of a contuction level indicator and indicaters for the absoption of the sample leaving the column. The pink, blue and red indicators correspond to the absorption at 680 nm, 280 nm and 260 nm respectively. The first decrease in the conduction indicates the sample application to the column and the corresponding intensity of the UV-Vis peak shows the amount of protein that is washed away from the column. As the conductivity level gradually decreases, the least hydrophobic proteins are collected from the column. The the first peak bolongs to least hydrophobic entities, sometimes phycobilisomes and carotenoids followed by a peak observed at ~175 mS/cm is the point where PSII proteins are collected. Varying between 140-120 mS/cm depending on the buffer condition, PSI monomer is seperated from the column. And the least hydrophilic entitty, trimeric PSI is seperated from the column when the conductivity level is around 85 mS/cm. As observed from the first two chromatograms, mixing the seperated bands results in a relatively larger trimeric peak. The separation of the peaks was achieved by the optimization of buffer and sample conditions. In the third panel, only the upper band of SDG sample is applied to the column, and the fourth panel shows the resulting chromatogram for the lower band of the SDG. Separation of the samples with the optimization of the chromatography conditions resulted in well separated peaks and thus more homogenious samples. In the last chromatograms, the ammonium sufate level of the buffer used in the separation (HIC buffer) is also

optimized. The relative intensity of the trimeric peak indicates the possibility that the monomerization is still going on during the column process. After optimizations were finished, as observable from the last two chromatograms, the monomer/trimer ratio drastically increased.

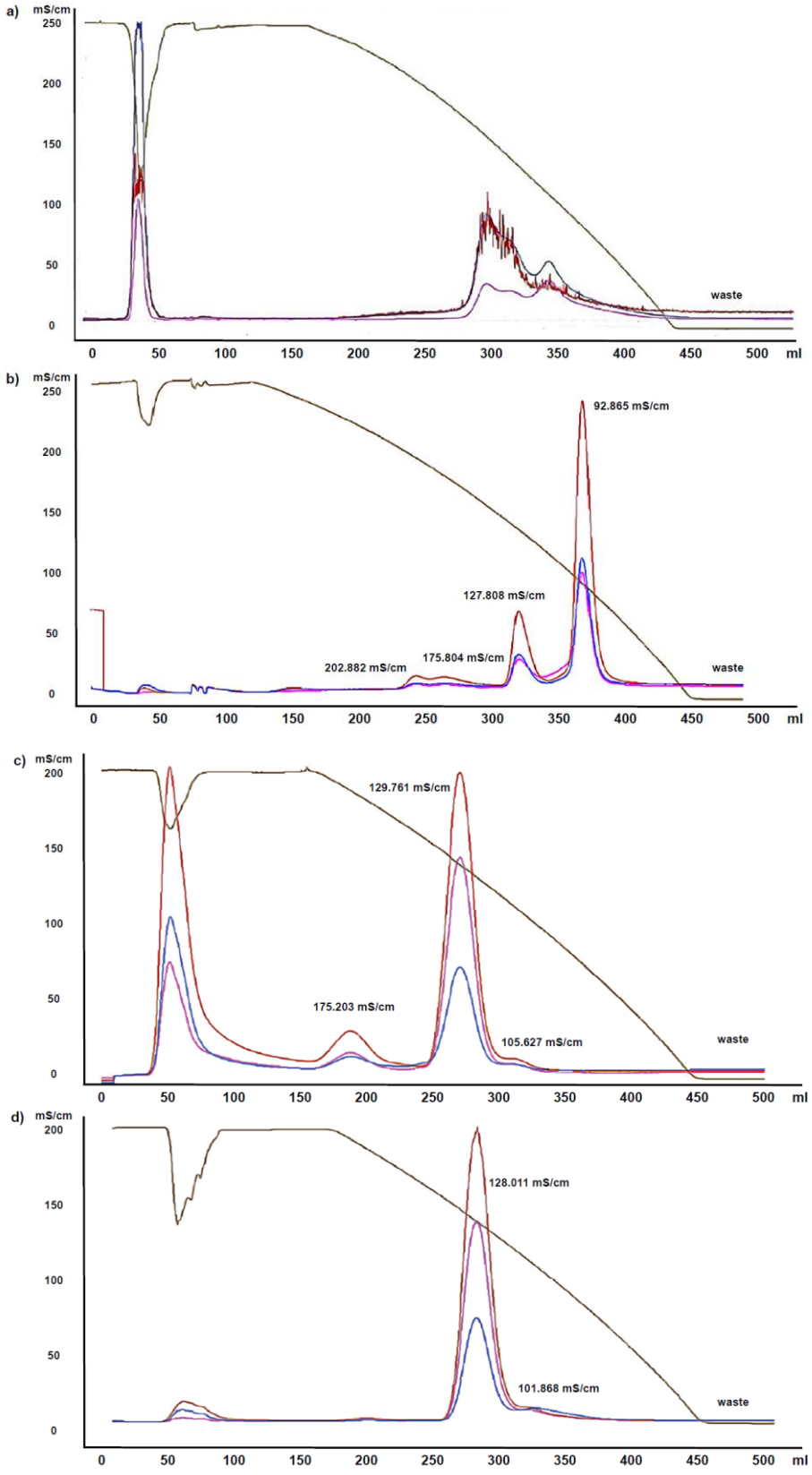

Figure 2-6 HIC Chromatograms, a Initial trials, b Chromatogram of sample from a mixed SDG bands c Chromatogram of sample from upper band of SDG, d Chromatogram from lower band of SDG. Brown peak displays the conductivity, blue, purple and red peaks show the UV-Vis signals at 280 nm, 680 nm and 260 nm

Figure 2-7 shows an SDS-PAGE from the optimization process of Protocol II. Control Monomer and Control Trimer are samples from Protocol I purification. The lanes labelled as Band II, Band III and Band III wash are samples after the hydrophobic interaction column. Second inlet visualizes the SDS-PAGE and BN-PAGE of the resulting proteins from Optimized Protocol II. Upper and lower band refer to the samples seperated in the SDG (Supposedly upper band should include Native PSI Monomers and PSII dimers, lower band should include trimers)

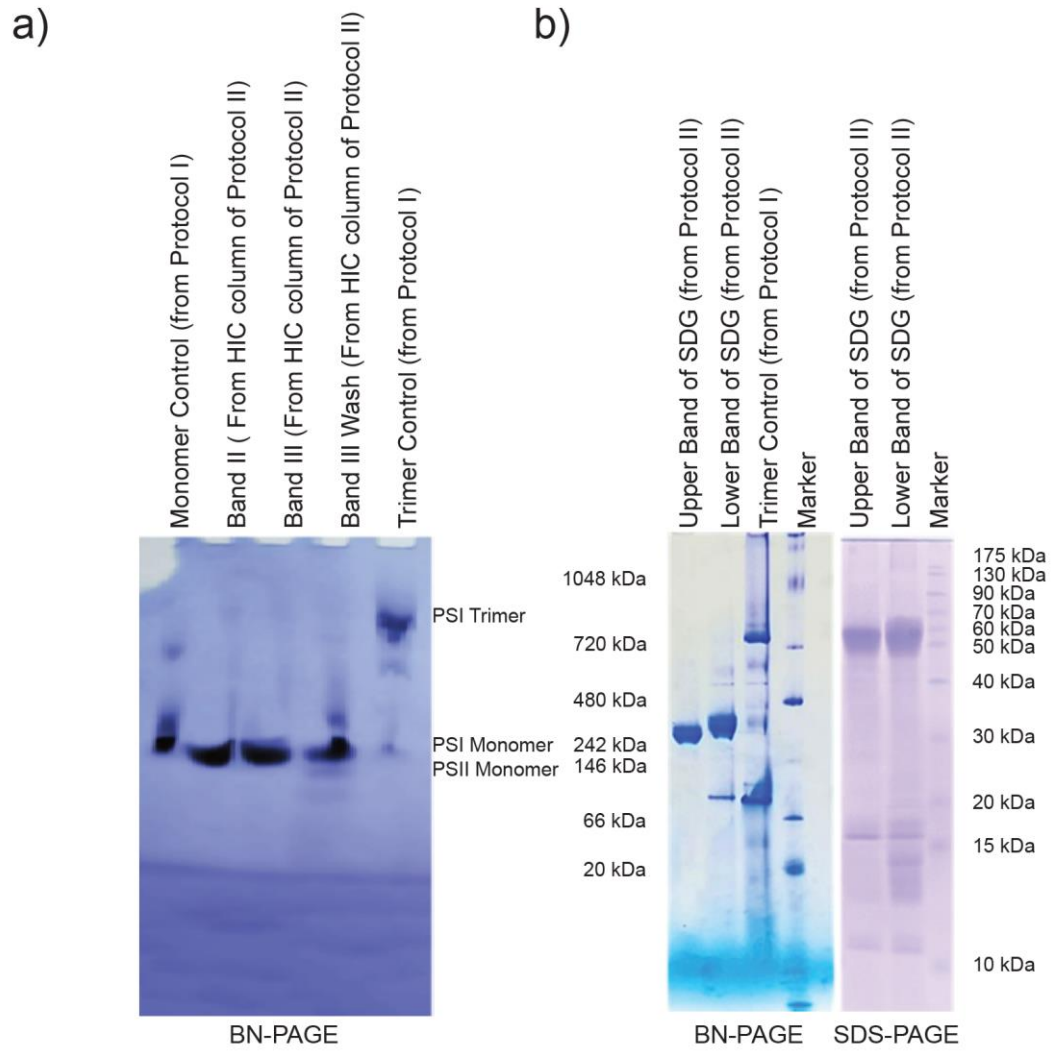

Figure 2-7 Electrophoresis Analysis of Purified PSI a) A BN-Page showing monomers and trimers from Protocol I with proteins from the HIC column of Protocol II in the optimization process b) BN-Page and SDS-page analysis of proteins purified by Optimized Protocol II.

Figure 2-8 shows the mass spectrometric comparison of PSI monomer and PSI trimer by MALDI-ToF mass spectrometry. The peaks determined by MALDI-ToF analysis accurately correspond to the masses of the PSI subunits known from the published high-resolution X-ray crystal structure[28]. Minor differences were interpreted as post-translational modifications. All theoretically calculated and practically determined masses are summarized in Table 2-5. The results confirmed the presence of all PSI subunits except for PsaA and PsaB, which are not in the detection range of the MALDI-ToF instrument. However, presence of these subunits was confirmed by SDS-PAGE analysis (Figure 2-7 b). Particularly, the presence of PsaK and PsaL, which are easily lost, confirms gentle purification of the complex. The functionality of purified PSI was validated by the measured activities, which are 1970 (± 306) µmol O_2 mg Chl^{-1} ml h^{-1} for the monomeric and 1793 (± 219) O_2 mg Chl^{-1} ml h^{-1} for the trimeric complex.

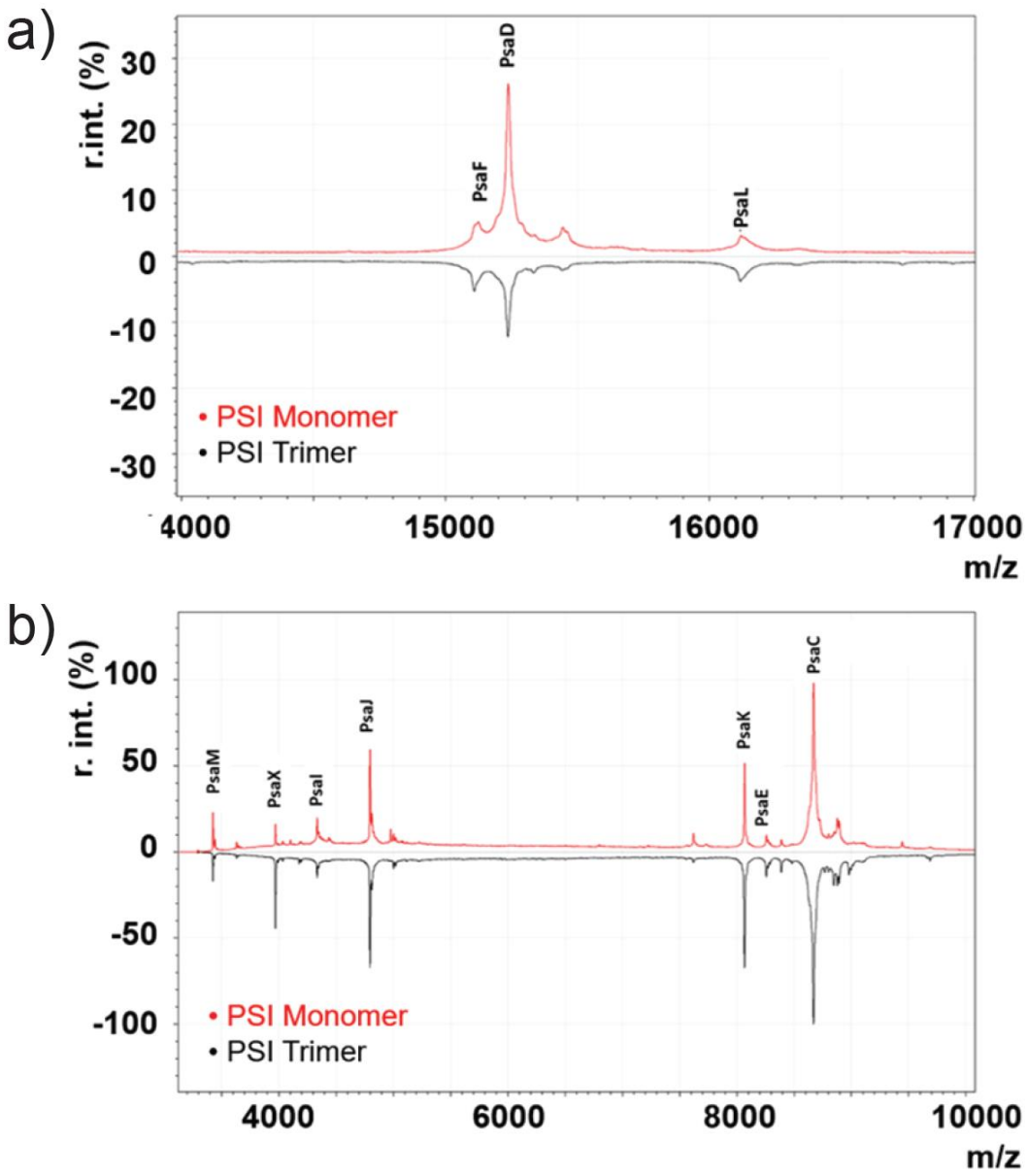

Figure 2-8 Comperative MALDI-TOF Analyses for PSI monomer Purified by Protocol II a) Abundance of PsaF, PsaD and PsaL subunits in the samples, b) Abundance of PsaM, PsaX, PsaI, PsaJ, PsaK, PsaE, PsaC in the samples

Table 2-5 Calculated and Determined Masses of PSI Subunits

Subunit	Calculated Mass (Da)	Determined Mass (Da)	Difference	Modification
PsaA	84872	Not Detected		
PsaB	83044	Not Detected		
PsaC	8800.1	8667.37	-132.73	*N*-methionine deleted
PsaD	15370.5	15237.49	-133.01	*N*-methionine deleted
PsaE	9388.5	8255.43	-133.07	*N*-methionine deleted
PsaF	15113.4	15108.52	-4.88	-
PsaI	4166	4332.97	+35.97	Acetyl group added
PsaJ	4755.7	4793.64	+26.94	Formyl group added
PsaK	8480	8065.36	-414.64	-(N-MVLA)
PsaL	16251	16.114.90	-131.10	*N*-methionine deleted
PsaM	3424.1	3423.10	-1.00	-
PsaX	4100.9	3968.79	-132.11	*N*-methionine deleted

All data calculated via https://web.expasy.org/protparam/

In Figure 2-9, UV-Vis spectra and 77 K Fluorescence spectra of PSI monomer and trimer are shown. UV-Vis spectra of both trimeric and monomeric PSI measured at room temperature revealed the differences in the range between 450 and 650 nm (Figure 2-9 a). The stronger peaks of trimeric sample around 490 and 630 nm, imply a slightly higher amount of carotenoids (A.M. around 500 nm) and phycobilisomes (A.M. around 650 nm). Additionally, a shift in the absorption of trimeric PSI towards longer wavelengths is detectable around 700 to 725 nm. This shift is an indicator of a higher amount 'red' chlorophylls in the PSI trimers and is in accordance with previous results[79,169]. Fluorescence emission spectra of both trimeric and monomeric PSI were measured at 77 K (Figure 2-9 b). Characteristic peaks around 730 nm (trimer) and 720 nm (monomer) were observed. The blue shift of chlorophyll fluorescence confirms the loss of 'red' chlorophylls in PSI monomers.

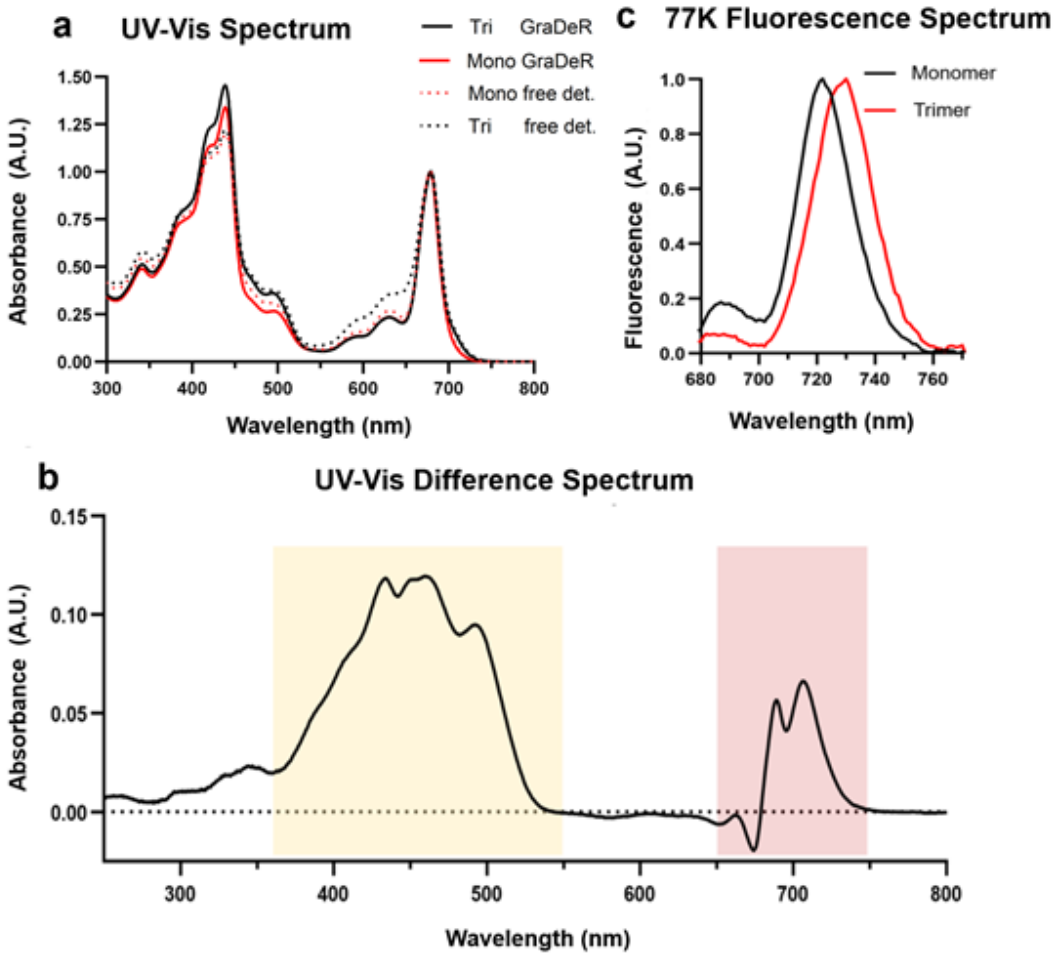

Figure 2-9 Comparative Spectroscopic Analyses for PSI Monomer Purified by Protocol II a) UV-Vis spectrum for monomeric(red) and trimeric(black) PSI before (dashed line) and after (full line) detergent removal, b) Fluorescence emissions for monomeric and trimeric PSI c) UV-Vis Difference spectrum of monomeric and trimeric PSI (orange is the carotenoid absorption region, red is the chlorophyll absorption region).

The biochemical and biophysical characterization shows that monomers and trimers have a similar level of activity, even though the monomers are produced by the break up of the trimeric protein. The full lined UV-Vis spectra are produced by the final sample, in which, the excessive detergent was removed by GraDeR methodology[109]. The differences for both monomeric and trimeric spectra before and after detergent removal imply that, there were phycobilisomes in the sample (550-650 nm region) which were removed by the GraDeR method. The difference spectra shows that trimeric sample has more carotenoids and chlorophylls per monomer. However, its noteworthy that detergent removal does not effect the absorption difference in the red region of the spectra.

To conclude, monomers were purified succesfully as well as trimers. Both oligomeric species were observed to be intact, pure and photosynthetically active but exhibited differences in UV-Vis spectra. Fluorescence spectra confirms this finding by the obsered red shift in trimeric spectra relative to monomeric spectra.

2.4 Discussion

According to characterization by biochemical methods and Maldi-TOF analysis, both protocols were succesfull in producing intact PSI monomers. Lower monomer yield of protocol I may be related to;

- Heat treatment: Considering the fact that monomers are less stable than trimers[102], treating the thylakoid membranes in the presence of ammonium sulfate may result in denaturation of some proteins.
- In-membrane Monomerization: Presence of the membrane surrounding the proteins may make them less accessible to ammonium sulfate and thus lower the yield of monomerization.
- Detergent Difference: LDAO may be more efficient in PSI extraction than β-DDM.

It was not possible to identify if there are any differences between upper band and lower band of SDG after the purification in Protocol II. Only information about this is the slightly higher size observable in the BN Page. Resolution of SDS-PAGE was not enough to comment on small subunits and their amounts in the sample.

Biophysical experiments run with the proteins purified by Protocol II show some spectral differences between monomer and trimer. Obvious decrease in the UV-Vis absorption and the shift in the fluorescence emission showing the decrease in absobtion capasity of the protein may be related to;

- Loss of some pigments upon monomerization
- Formation of uncoupled chlorophylls upon monomerization
- Change in the environment of chlorophylls upon monomerization
- Deformation of specific clusters of chlorophylls (red chlorophyll clusters) upon monomerization.

These spectra will be used in the structural analysis chapter as supporting information and the related literature will be surveyed in depth.

CHAPTER III.

X-RAY EXPERIMENTS

3 X-RAY CRYSTALLOGRAPHY OF PHOTOSYSTEM I

3.1 Introduction

The first protein structure determined by X ray crystallography was published in 1958[81]. The fact that it took over 20 years for the first membrane protein structure to come up[82] clearly shows that membrane protein purification is an ambigious process. The vast amount of knowledge deposited in the literature shows that these difficulties basically originate from three issues[83];

- Low yields of protein purification
- Instability of the protein out of the membrane
- Homogeneity of the protein

Cell membranes are composed of lipid bilayers sheltering the transmembrane proteins, parts of which span the hydrophobic regions of the bilayer as α-helically coiled or sometimes β-barrel shaped polypeptides[84]. "These bilayers are not linear polymers; rather, they are composed of a wide diversity of many single amphiphilic lipid molecules forming a volume enclosing 3D structure and their architecture is not encoded in genetic information."[85] Lipid molecules intermingle in a way to leave the hydrophilic head groups outside while forming a bilayer. Universally, the thickness of a bilayer is ~30 Å in the hydrophobic interior and is ~50 Å with the headgroups included. The density, dielectric constant and and composition is erratic, providing the ability of movement to the embedded proteins[85]. A cartoon of the widely accepted Singer-Nicolson model of the biological membrane is shown in Figure 3-1[177]. Diversity of modus operandi provided by the necessity of adaptation to change of environmental factors maintains the membranes with the ability of regulating the chemical locality of the proteins. The consequent excellency in stabilization and protection of proteins can hardly be maintained out of the membrane.

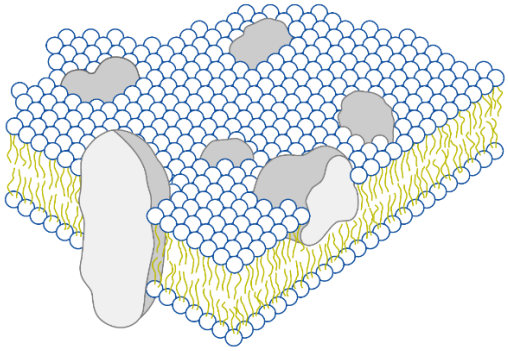

Figure 3-1 A model visualising the fluid-mosaic model of the biomembranes as a passive matrix wherein transmembrane proteins can move freely[85]

Keeping the proteins in their native environment provides them with the highest stability as well as attenuating the chances of unpredictible structural alterations. Accordingly, devising a chemical climate ideally same as the bilayer membrane to the proteins out of their native environment is the first step for a succesfull crystallization. Mimicking the membrane is attainable owing to the comprehension about the behaviour of lipid like amphiphilic molecules in solution. [170,171]. Detergent molecules, owing to their structure consisting of a polar group at the end of a lipophylic hydrocarbon tail, may form clusters in order to hide the hydrophobic part from available water, resulting in micelle formation[86]. Micelle sizes vary depending on the concentration of detergent. This behavior allows detergents to form an environment physically resembling the membrane. Combined with the ability to replace the lipid molecules surrounding a protein embedded in a membrane, resulting in its extraction[86], choise of proper detergent becomes paramount in membrane protein purification, affecting the yield of the purification and also stabilization the protein. On the other hand, depending on the chemistry of the detergent, overutilization or underutilization could result in aggregation, denaturation or decomposition of the protein too[87].

Even though detergent use is very critical in mediating a native like environment to protein in which it can maintain its activity, solution parameters such as ionic strengt, pH and temprature are also very important[88]. The preservation provided by the optimization of these conditions is the basis of crystallization which necessiates manipulation of the interactions between the proteins [89].

A protein crystal is a form wherein individual protein units are arranged in a periodical manner. This periodicity results in layer formations and upon interaction with photons, depending on the arrangement, it is possible to observe the diffraction[89]. An ideal crystal would react the same way to incoming photons at every repeating unit and provide a recurring signal. For this to happen, all the units of the crystal should be precisely in the same orientation and they should fulfill interconnections in a patterned fashion. Just as its cardinal effect in preservation of the protein in solution state, owing to being a part of the protein by surrounding its hydrophobic regions as a belt, the detergent has an indicative role in governing the orientation movement of the protein in solution, dictating its interactions with its environs. Difficulties in obtaining a crystal are not simply limited to sample condition and protein environment. A crystallization drop is a very complex system with many thermodynamic parameters and with different kinds of interactions happening instantly under many forces. From a physical point of view, crystallization may be defined as a complex form of state transition, from a less ordered solid state or liquid state to the crystalline state. This transformation is driven by the variation of the energy in the crystallization drop. Growth rates and morphologies of crystals vary with respect to these barely controllable dynamics that determine the energy of the system. In order for crystals to occur, proteins in the solution are required to form a nuclei, possibly a small cluster. The next requirement is the interaction of the proteins that are still not in the crystalline state with this nuclei, minimizing the energy of the system gradaually. The nuclei can be formed by the solution itself providing that it is in a state of supersaturation, or can be situated by an external addititive[172,173]. To manipulate the dynamics of crystallization drop system, thermodynamic properties of the solution are used as instuments. The dissolving capacity of the solution is usually used for transforming the solutes to the solid crystalline state. Solvent, entities competing with protein molecules for acces to solvent molecules, the electrostatic properties of the solutes and their manipulation by pH and temprature may be listed as the main instrumentation. In order to obtain the nucleation and control the growt, many methods has emerged such as vapor diffusion, microbatch, microdialysis etc., all depending on manipulating the solubility over time. If crystals are obtained succesfully, another step before the structural analysis is cryo-preservation. In order for the crystal to be preserved

during the freezing until the measurements, a cryoprotection should be provided[100,101].

Cyanobacterial PSI was succesfully crystallized in 2001[28], forming crystals diffracting to 2.5 Å . The high solvent content (>80%) and the insufficient utilization of surface area in the formation of crystal contacts (<5%) has been reported as the resolution limiting factors during the optimization of the crystals[174]. Since its crystallization, despite many attempts, none of the PSI crystals reached a better resolution than 2.5 Å . (See Table 3-1 for a list of the highest resolution PDB entries.) The rationale behind this hindrance despite the amelioration of the technique may be related to asymmetry of the protein, yet unmanageable flexibility issues or anavoidable stability problems.

Table 3-1 Published Highest Resolution PSI Structures from Protein Data Bank

YEAR	PDB ID	CITATION	RES. (Å)	SPECIES
2001	1JB0	Jordan *et al.*[28]	2.5	*Thermosynechoccoccus elongatus*
2018	5OY0	Malavath *et al.*[41]	2.5	*Synechocystis sp.*
2019	6PFY	Gisriel *et al.*[90]	2.9	*Thermosynechoccoccus elongatus*
2003	1QZV	Ben Shem *et al.*[91]	4.4	*Pisum sativum*
2014	4KT0	Mazor *et al.*[92]	2.8	*Synechocystis sp.*
2019	6PGK	Gisriel *et al.*[90]	2.9	*Thermosynechoccoccus elongatus*
2014	4L6V	Mazor *et al.*[92]	3.8	*Synechocystis sp.*
2012	4FE1	Brunger *et al.*[93]	4.9	*Thermosynechoccoccus elongatus*
2011	3PCQ	Chapman *et al.*[94]	8.9	*Thermosynechoccoccus elongatus*
2015	4RKU	Mazor *et al.*[193]	3.0	*Pisum savitum*
2019	6FOS	Antoshvili *et al.*[95]	4.0	*Cyanidioschyzon merolae*
2018	6HQB	Netzer-El *et al.*[39]	4.0	*Synechocystis sp.*

2018	5ZF0	Kubota-Kawai *et. al*.[40]	4.2	*Thermosynechoccoccus elongatus*
2015	4Y28	Mazor *et al*.[96]	2.8	*Pisum savitum*
2007	2O01	Amunts *et al*.[97]	3.4	*Arabidopsis thaliana*
2017	5L8R	Mazor *et al*.[98]	2.6	*Pisum sativum*
2015	4XK8	Suga *et al*.[99]	2.8	*Pisum sativum*
2020	6UZV	Toporik et al.[186]	3.1	*Synechocystis sp.*
2020	6TRA	Kölsch *et al*.[181]	2.9	*Thermosynechoccoccus elongatus*

Specifically for PSI, it has been reported that monomer crystallization is much more challenging than trimer cristallization[102]. In the same study, it has been explained that the crystallization strategy was based on the solubility of the protein. According to the detailed analysis on the behaviour of solubility of PSI, it is outlined that;

- The possibility that a change of an aminoacid charge on the surface of the protein may result in a drastic change in the solubility,
- The ratio of detergent to protein,
- Number of binding ligands,
- Ionic strength,

are important factors in the control of the solubility of PSI. In any monomerization process of PSI, it is very likely that the aminoacids in the surface at least change their conformations due to the changing environment. Moreover, the change in the surface area logically increases the detergent/protein ratio consequently increasing the solubility of the monomer when compared to trimer. Moreover, a predicted change in the number of binding ligands upon monomerization may result in the change of the solubility of monomeric PSI. The reported struggles in the crystallization of monomeric PSI are associated with these structural differences[102].

3.2 Materials and Methods

Due to the difficulties in controlling and manipulating such a complex system a systematic screening approach was employed. After trying crystallization in pre-prepared solutions with an robotic crystallization system (Mosquito LCP-136, TTP Labtech), the crystal forming conditions are identified as a starting point for search of optimal conditions. For the subsequent screening, variables are set as pH, temprature, salt conditions, precipitating agents. Vapor diffusion method was employed for gradually removing the solvent from the drop to induce the formation of crystal contacts. Figure 3-2 shows the scheme for crystallization experiments.

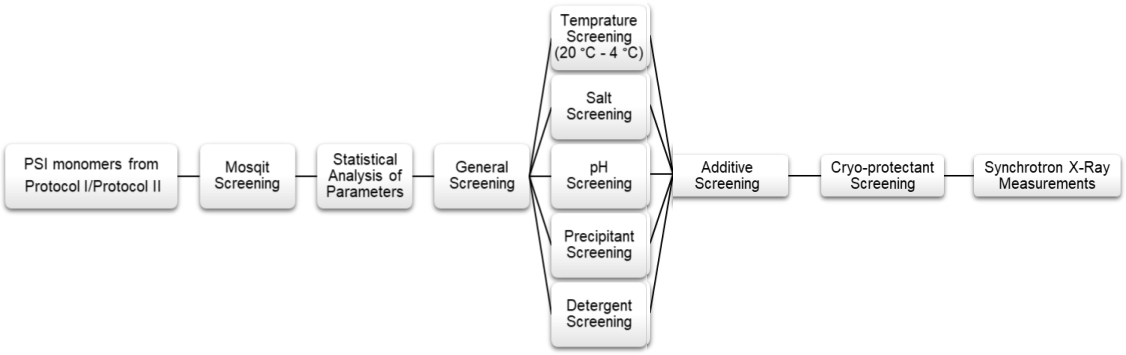

Figure 3-2 Workflow of Crystallization Experiments

PSI monomers extracted by Protocol I and Protocol II were both subjected to the same systemmatical screening. Initial screening was implemented using the commercially available prepacked screening kits MEMGOLD I, MEMGOLD II, MEMSTART, MEMSYST (Molecular Dimension), CRYSTAL SCREEN I, CRYSTAL SCREEN II, PEGION I, PEGION II (Hampton research) as the crystallization buffer and applied to VCP-1 96 well plates by the robotic crystallization system. Drops are observed for two weeks and the crystallization buffers imparting crystals were chosen for further optimization. These starting buffers were used to produce crystallization solutions that gradually change in pH (buffer type and concentration), salt (type and concentration), precipitant (type and concentration) in crystallization drops with a volume of 2 µl consisting of 1 µl protein solution and 1 µl of reservoir solution. The reservoir volume was 150 µl. In all experiments, the protein solution concentration was kept constant at 3 mg Chl/ml. The crystal drops were observed for two weeks on a daily basis. The

crystal drops are incubated seperately at room temprature and 4 ºC and it was observed that room temprature incubation resulted in degradation of the proteins resulting in red crystals. After this observation incubation was done on 4 ºC. After finding the best conditions, Hampton Research Additive Screen was used for improving the crystal quality further. The conditions screened are shown in table 3-2.

Table 3-2 Crystallization Screening Conditions

Precipitant	Precipitant Percentage (%)	Buffer	Ph Range	Salt	Salt Molarity	Additive	Detergent
PEG 200	18-41	MES	5.0-7.0				
PEG 400	18-41			NaCl	0.1 – 0.3		β-DDM
PEG 500	18-41	HEPES	7.0-8.0				
PEG 1000	4-20						UDM
PEG 1500	4-20	Glycine	9.0-9.5	$MgCl_2$	0.1 – 0.3	Glutathione (red-ox)	
PEG 2000	4-20						DM
PEG 3000	4-20	TRIS	7.0-9.0	$LiSO_4$	0.1 – 0.3		
PEG 3350	4-20						OG
PEG 4000	4-20	Sodium Acetate	3.5-5.5	KCl	0.1 – 0.3		
PEG 5000	4-20						
PEG 6000	4-20	TES	7.5	LiCl	0.1 – 0.3	Betaine HCl	
MME 500	4-20						CYMAL-7
Jeffamine	4-20	BIS-TRIS	7.5	None	0.1 – 0.3		

Drops were investigated by an Olympus SZX7 stereo microscope. Observed crystals are collected by Hampton Research Mounted CryoLoops with 0.05-0.1 mm size. Prior to freezeing, crystals are immersed in their respective reservoir solution including 0-30% ethylenglycol with 5% steps for cryo-protection. Crystals are kept in cryoprotectant solution for half an hour each step. The last step is repated three times.

PSI monomers purified by Protocol I were subjected to initial screening 3 times and general screening 8 times. PSI monomer purified by Protocol II were subjected to initial screening two times, general screening 37 times and additive screening one time. Total number of conditions screened for Protocol I proteins is 768, and for Protocol II proteins 3552. It was not possible to obtain crystals diffracting to better than 20 Å, however a best resolution of 14 Å was obtained from Protocol II proteins. Variation in the drop condition was used as a guide to manipulate the conditions after every batch.

The best PSI monomer crystals used for X ray analysis were obtained by hanging-drop vapor diffusion method at 277.15 K in the former studies in this lab, by Protocol I proteins. A hanging drop was prepared by mixing equal volumes of protein solution (3 mg Chl/ml) and reservoir solution containing 50 mM Tris, pH: 7.5, 50 mM NaCl and 20% (w/v) Polyethylene glycol (PEG) 400. For X-ray intensity data collection, the single crystals were transferred to a cryo-protectant solution containing the same buffer of crystallization buffer with 30% ethylen glycol and immediately frozen with liquid nitrogen.

3.2.1 X-ray Measurements

The X-ray diffraction of all the crystals were measured at the SPring-8 synchroton facilities in Koto, Hyogo. Native data was collected on beamline BL44XU at SPring-8 using CCD detector MX-300HE (Rayonix) at cryogenic temperature (100K). The native data set was processed and scaled using program XDS[103] and diffraction data at 6.5 Å resolution with 98.46% completeness was obtained from 180 frames. A crystal of PSI monomer belonged to space group $P3_221$ with cell dimensions of a=187.029 Å, b= 187.029 Å, c= 233.805 Å. The crystal contained one molecule in an asymmetric unit. Initial phase was determined by molecular replacement method with program PHASER[194] in CCP4[104]using the X-ray structure of PSI (PDBID: 1JB0) as a starting model. The initial electron density

map revealed most of the main chains of PSI. The structure model was manually revised using program COOT[105] in CCP4, and external restraints refinement was performed using REFMAC5[195] and ProSMART[106] in CCP4. All figures showing the atomic coordinates were made with ChimeraX[107].

3.3 Results

The best crystals from Protocol II purified PSI monomer was obtained after the additive screening. These crystals appeared at 4 ºC in a crystal buffer containing no salts, 8%-15% PEG and 0.1 mM HEPES buffer at pH:7-7.5 with %0.003 β-DDM detergent within a week after the beginning of incubation. Some of the best crystals obtained by Protocol II are shown in Figure 3-3.

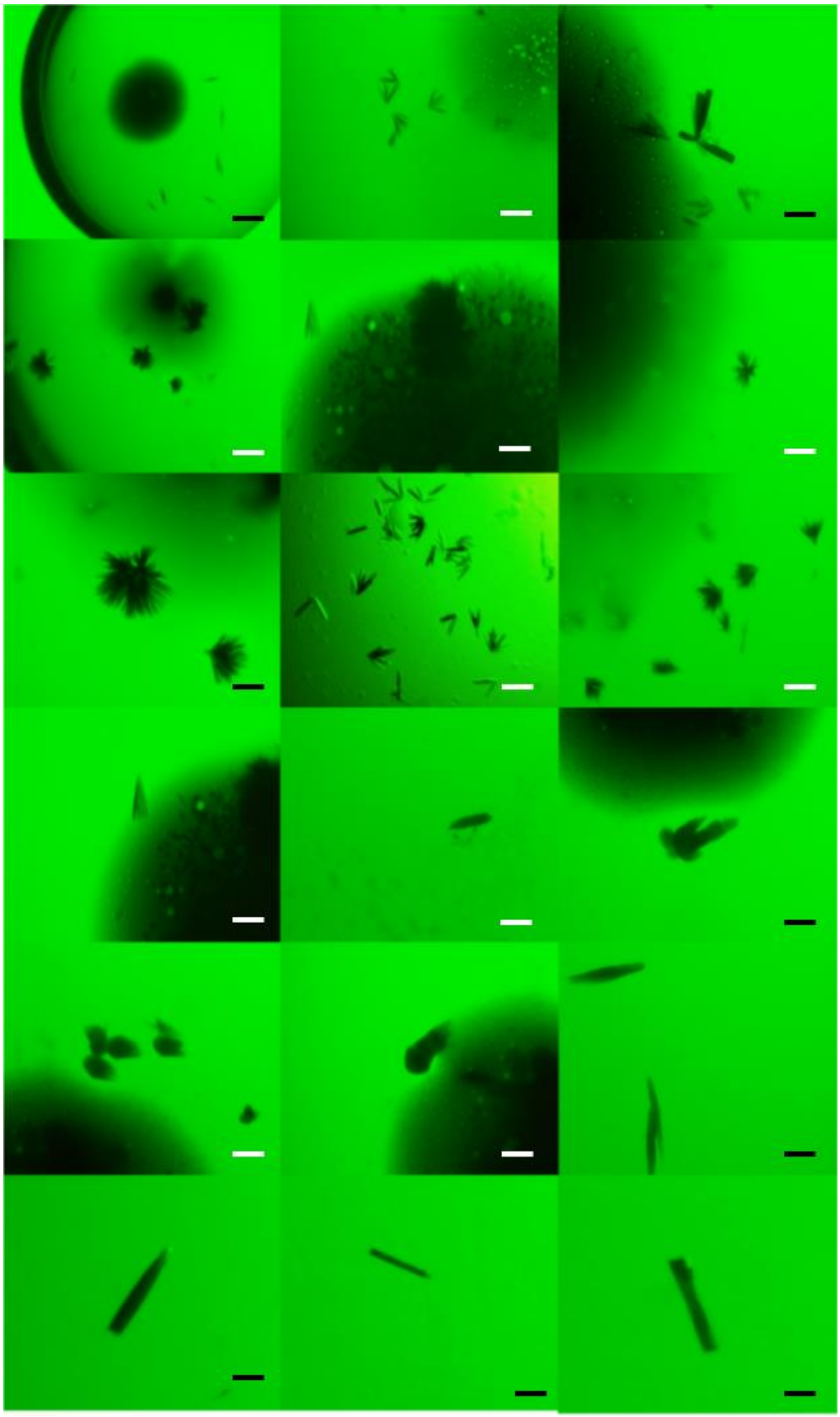

Figure 3-3 Various Crystals of PSI Monomers Purified by Protocol I. The crystal sizes are in the range of 0.05 (black scale bar) - 0.1 μm (white scale bar).

As clearly observable, it was not easy to obtain crystals in the appropriate size and shape. Moreover, only a small portion of crystals were observed to be single crystals, indicating that the optimization is necessary in nucleation.

The best monomeric PSI crystal that was used in the X-ray measurements is shown in Figure 3-4. This crystal is obtained from Protocol I proteins and diffracted to 4.0 Å resolution.

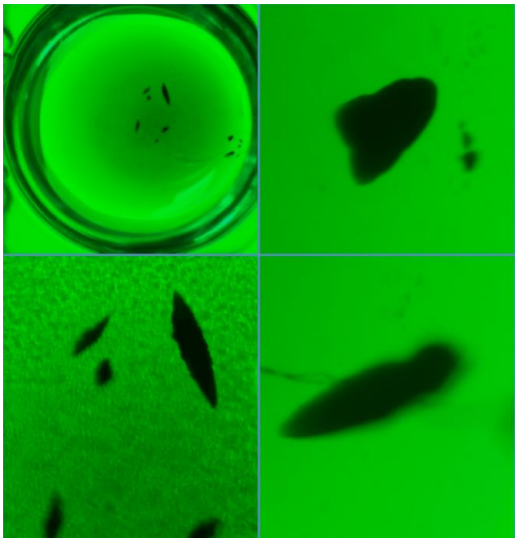

Figure 3-4 The Crystals That Provided The Data Used in Refinement.

Its crystallographic statistics can be seen in Table 3-3. Resulting 6.5 Å model was deposited to PDB with the accession code 7WB2. The solvent content within the crystal was calculated to be 63.55% using the Matthew's Coefficient program in CCP4 package[175].

Table 3-3 Crystallographic Table for PSI Monomer Crystal Structure

Native Data	
X-ray source	SPring-8 BL44XU
Detector	MX-300HE
Wavelength (Å)	0.90000
Space group	$P3_221$
Unit cell parameters	
a, b, c (Å)	187.029, 187.029, 233.805
β (°)	120
Resolution range (Å)	49.57 – 6.5 (6.732-6.5)
Total number of reflections	102,562 (10731)
Number of unique reflections	9,572 (949)

Multiplicity	10.7 (11.3)
Completeness (%)	98.46 (100)
Mean *I*/sigma (*I*)	29.58 (7.39)
R-merge (*I*) (%)	0.05486 (0.3354)
CC½ (%)	0.999 (0.978)
Refinement	
Resolution range (Å)	49.57 – 6.5
Reflection used	9556
R_{work} (%)	0.3940
R_{free} (%)	0.4616
Total number of atoms	23,837
Averaged B-factor (Å ^{2})	259.26
R.M.S.D. (Bonds (Å) /Angles (o))	0.033/2.11
Ramachandran Favored (%)	93.86
Ramachandran Allowed (%)	5.69
Ramachandran Outliers (%)	0.55

The numerals in parentheses are for the highest resolution shell.

Resulting overall view of the electron density map and model of PSI monomer crystal structure can be seen in Figure 3-5. At this resolution, the identification was possible in α helical level. The resolution was not good enough to model the ligands of the protein and the map did not allow a good resolving of the amino acid side chains.

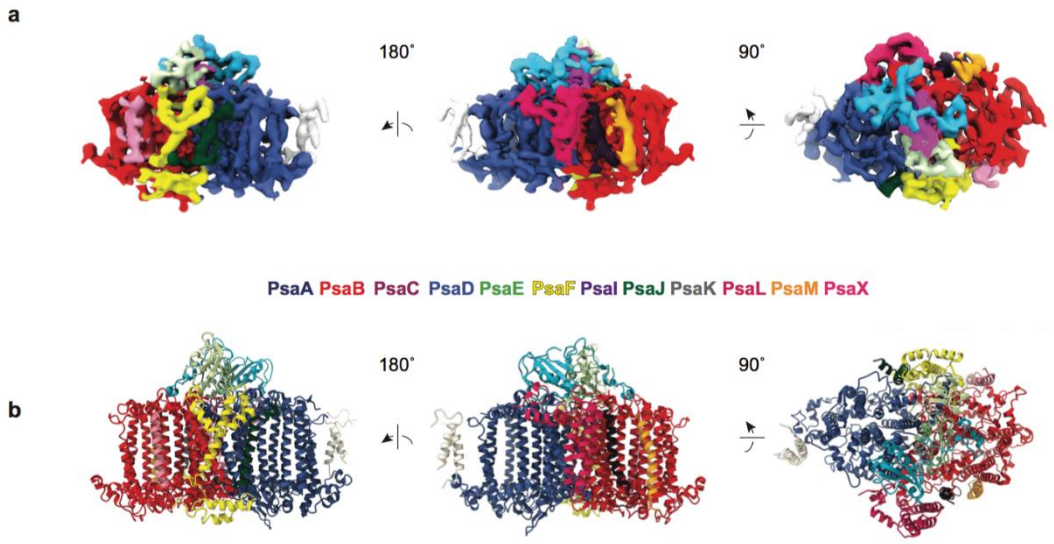

Figure 3-5 The X-ray Crystal Structure Model of The PSI Monomer (PDB ID 7WB2) Determined at 6.5 Å. View parallel to membrane from the membrane side (Left), trimerization side (middle) and view along the membrane normal from the stromal side. Coloring of subunits in this figure is according to Jordan *et al*., 2001 as indicated by the font color of the subunit names. a) Calculated X-ray electron density map and b) X-ray crystallographic model.

However, this structure allowed to confirm that the PSI monomer includes all of the subunits and the same level of transmembrane polypeptides as trimeric PSI. Only significant difference from the trimeric PSI structure was that C terminal small alfa helix of PsaL was not visible due to lack of electron density in that region, signifying that either secondary structure is disturbed or the helix became flexible upon monomerization.

3.4 Discussion

Despite systematic efforts for optimizing the crystallization conditions and the smaller size of the protein compared to trimer, no crystals reached the same resolution range as their trimeric counterparts. The reasons are not clear. Moreover, why the diffraction ranges of the monomers purified by Protocol I and Protocol II are not the same is not clear neither. The main difficulties specific to PSI crystallization are summarized as[102];

- Physiological status of the organism and based on adaptation to enviroment (heterogeneity and TM environment)
- Oligomeric form heterogeneity (disturbances on crystal structure caused by a small amount of smaller or larger oligomers)
- Solubility differences of the oligomers, monomer being more soluble and thus less crystallizable under low ion strength)!!
- Possible loss of small subunits and the heterogeneity caused by this.
- Possible presence of contaminant by-products of purification which can interact with protein.
- Drastic increase in the protein solubility due to the difference of detergent/protein ratio, monomer being three times higher than trimer.

The growth conditions of the culture was kept same in all of the experiments to avoid the differences based on the status and condition of the organism. Even cell harvesting time was kept constant in order to keep the cells in the same condition considering the circadian clock of the cyanobacteria. Growth rates of the cultures were observed to track the cell conditions.

In Protocol II, the optimization of the experimental conditions led to clear seperation of the monomeric and trimeric forms, as monitored from SDS-PAGE

and BN-PAGE results. Monomeric fragments did not involve trimeric forms. This is also attested in negatively stained EM analysis. (Data will be shown in the next chapter.) Chromatograms and gel electrophoresis results also show that there are no contaminants observable by these methods. However, negative staining results (will be shown in the following chapter) show that the sample includes very small particles, most likely broken ATPase particles. Effect of the presence of these particles on crystallization of PSI monomers purified by Protocol II is questionable.

Crystallization strategy employed was not to create an ionic strength gradient, but a method depending on the solvent vaporization. Even though a screening on different salt concentrations were employed, these were at 10 mM level and in the batch of the best crystals from optimized purification, no salts were present (Protocol II proteins). The effect of the salts on solubility of the PSI monomer can thus be ruled out. Moreover, in addition to these issues, cryoprotection of the crystals was also considered an issue about resolution and a proper screening was also done to adress this issue. Additionally, considering the reported possibility of the presence of different PSI pools (as discussed in Chapter II) with varying subunit content in the membrane[108], SDG bands are not mixed and treated as different preperations to exclude the heterogeneity introduced by the subunit occupancy differences. Depending on the resulting crystals from the upper band proteins and lower band proteins, its not possible to say this created a difference either size and morphology or resolution of the crystals.

Reasons for the low quality of crystals of the PSI monomer purification using Protocol II are possibly:

- Lack of control in the solubilized protein: Detergent molecules may be blocking the protein from making crystal contacts. In order to adress this issue, a detergent screening was employed, but non of the detergents tried (see Table 3-2) yielded in better crystals than the current best. It is possible that PSI monomer needs a specifically designed detergent. Moreover, the excess detergent in the protein buffer and the undetectable contaminants captured in the micelles may be removed by GraDeR approach[109] prior to crystallization.

- Presence of some undetectable impurity proteins/partial proteins in the sample that interact/shield the monomers from forming crystal contacts: As it will be shown later, some partial proteins (possibly an ATPase subunit) was found in the purified sample. These proteins were not detectable by gel electrophotesis or were not observable in the chromatograms. Eliminating these contaminants may improve the crystal quality.
- Natural or induced flexibility in peripheral subunits: The literature shows that there is a possibility of the presence of PSI monomers in the membrane which lack small peripheral subunits like PsaK, PsaI etc. In addition to resulting in occupancy problems, these subunits may have a role in forming the crystal contacts. Due to their small size, it is very difficult to prove their presence with electrophoresis or negative staining. However, the fact that crystals were possible to obtain in both native monomers and monomers obtained by the monomerization of the trimers indicates this was not an important issue in this case.
- Crystallization temprature: It was clearly observed that, crystallization drops in 20 ºC provided red colored crystals, showing that 20 ºC results in either denaturation of the proteins or at least release of carotenoid molecules from the proteins. Considering its effect on nucleation dynamics, a temperature screening with smaller variation in the intervals may be beneficial for crystallization.

Nevertheless, the crystal analysis provided valuable information that the monomeric PSI monomer isolated included all the subunits and maintained the general structure of trimer at the α helical level. Even though the resolution of crystal structure did not allow to observe the positions of the ligands in the structure, it was good enough to place the main frame of the protein and see that terminal helice of PsaL subunit was flexible. These information will support the higher resolution analysis in the following chapters.

CHAPTER IV.

CRYO-ELECTRON MICROSCOPY OF PHOTOSYSTEM I

4 CRYO-ELECTRON MICROSCOPY OF PHOTOSYSTEM I

4.1 Introduction

Amidst the creative, cooperative efforts by numerous scientists from different disciplines including physics, computational sciences and structural biology, cryo-electron microscopy (cryo-EM) advanced into a new era of high resolution structural analyses. Even its development stage from 1970's to mid 2010's provided benefits which has many applications in different areas of research. But it emerged as an expertise that is increasing the swiftness of structural biology research with the development of fast readout detection and motion corrections[188]. With a new strategy of removing the excessive detergents from sample buffer finally resulted in the identification of near atomic resolution structure of membrane proteins[189]. After this point, cryo-EM started to be considered as a method both competing and complementing X ray diffraction and following advencements in the field not only improved what cryo electron microscopy has to offer, but also what structural biology has to offer (Figure 4-1). This leap forward also incited an upsurge in the number of analyzable macromolecular complexes. Eventually, in 2017, Jacques Dubochet, Joachim Frank and Richard Henderson were awarded the Nobel Prize for heralding and accelerating the maturation of this technique[110].

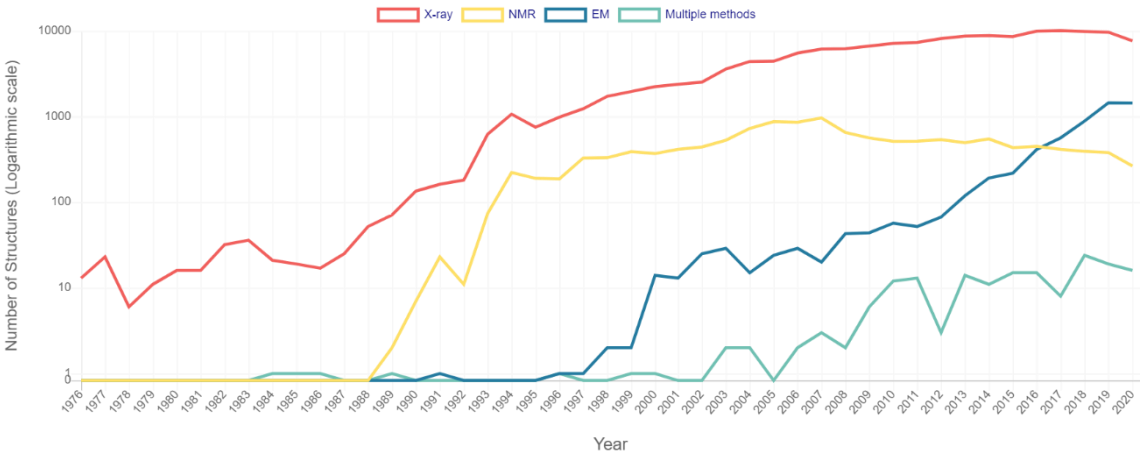

Figure 4-1 Change in The Number of Released Biological macromolecules' Structures in Time by Methodology[112]

The current methodology for a typical cryo-EM measurement is using a transmission electron microscope to image macromolecules or their complexes frozen in a thin layer of vitreous ice followed by processing the images,

eventuating in the reconstruction of the 3D volumes of Coulombic density of the macromolecules or their complexes. The principles of 3D volume reconstruction using the EM images stands on the central section theorem of Fourier transformations[113,196] and was proposed by Aaron Klug and his colleagues at MRC-LMB in the 1960's. According to this theorem[114], “The Fourier transform of a projection function of a 3D function is equal to a central section of the Fourier transform of the 3D function.” The fact that the inverse Fourier transform of a Fourier transform reconstitutes the original function is also fundemental in this context. Considering the geometry of an electon microscope, the images observed are projections of a 3D object. Klug *et al*. proposed that the 3D structure reconstruction can be fabricated following the steps of;

- Collection of images of macromolecules in many different orientations,
- Fourier transformation the images,
- Combining all the central sections of the Fourier transform,
- Inverse Fourier transforming the combination to restore the macromolecule structure[115].

This scheme became the basis of 3D structure reconstruction from EM images and subsequently new structure determination approaches were developed based on the scheme. For this contribution, Klug was awarded the Nobel Prize in chemistry in 1982[111]. With the gradual improvements in hardware and software, image processing and 3D reconstruction also improved a lot, leveraging the limit of resolution to challenge X-ray single crystal diffraction methodology. Today, it is possible to obtain atomic resolution from the particles dispersed in a solution, making it possible to analyse proteins that are very difficult to crystallize.

Currently, provided that hardware is in an advanced setting and the sample is appropriate, it is possible to design a workflow of image processing starting with the motion corrections on micrograph level, Contrast Transfer Function (CTF) estimations, autopicking, 2D classifications (projections) and 3D classifications (volumes), motion corrections on particle level, refinement of a 3D model of the protein from differently oriented particles and sharpening with respect to signal-to-noise ratio. A general workflow is shown in Figure 4-2.

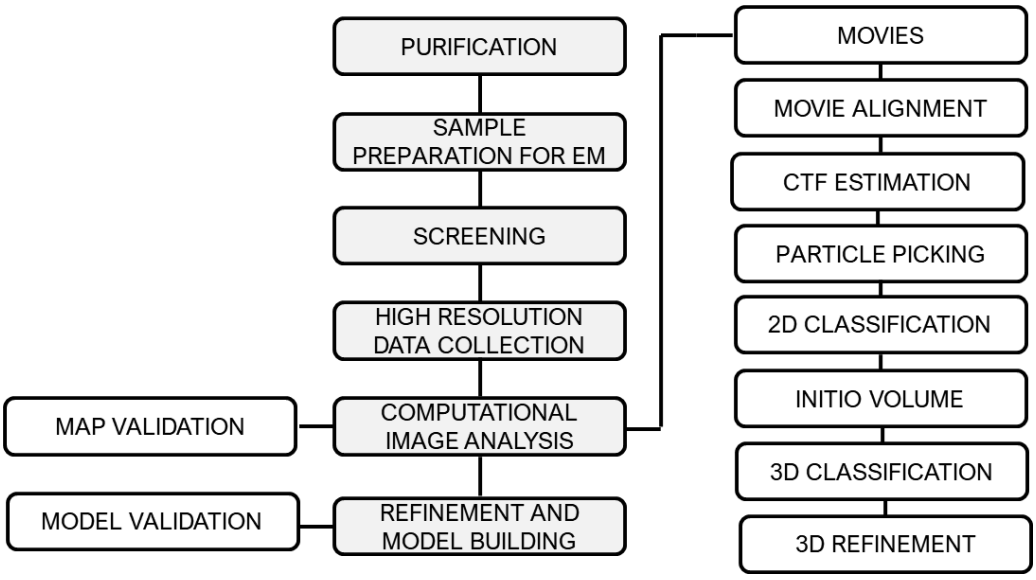

Figure 4-2 Image Processing in a Typical Cryo-EM Experiment Typical Cryo EM analysis workflow[116]and Typical Image Processing Workflow[117]

The advancements in freezing techniques, hardware and software resulted in an accumulation of the structures revealed by cryo-electron microscopy. With the increase of the availability of the method, the advantages and disadvantages of using cryo-EM in structural analysis became more clear. In a recent review, these advantages are listed as[118];

- Liberation of the analysis from usually cumbersome crystallization process
- Suitability for relatively large protein complexes,
- Reduction in radiation damage,
- Maintanance of information about the native states of the proteins,
- Ability to capture different conformations in single experiment,

Same article refers to the disadvantages of the method as;

- A limitation in the minimum size (lately is reached 52 kDa from 150 kDa)
- Difficulty in obtaining results from flexible parts of the proteins
- Better than 2 Å resolution is very hard to reach

These shortcomings are associated with the resolution limiting factors of an electron microscope. As a protein solution is dispersed onto a grid and frozen on the grid, the limiting factors are introduced in the very first step. Design of a grid is shown in Figure 4-3.

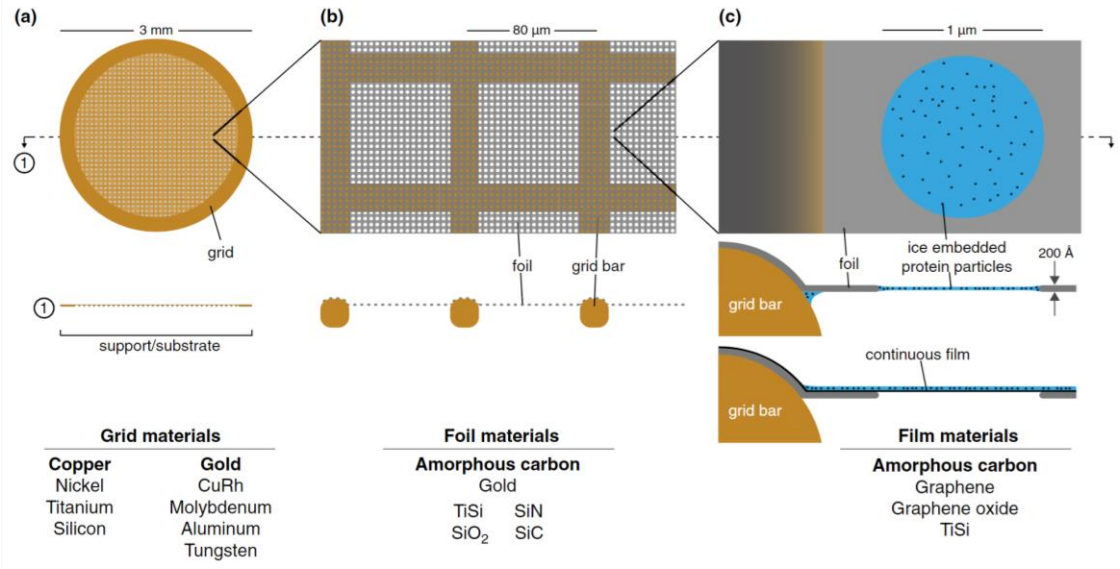

Figure 4-3 Design of Cryo-EM Grid. Top view and section diagrams of typical specimen support geometries. Three different magnifications are shown (a)–(c). Also materials used for each component of the support is given, the most common are in bold[119].

One of the basic outcomes of the central section theorem is the necessity to obtain the projections from as many orientations of the object as possible. The flash freezing of the sample is an abrupt phase transition with a consequent unpredictibility in the behaviour of the protein during the process. Depending on the buffer condition, self-dynamics of the protein and duration of the freezing process, this phase transition may result in a preferred orientation of a protein, or sometimes even in aggregation. These usually happen in the time between formation of a thin liquid film by blotting and shock freezing. Besides, it is possible for proteins to localize in regions of the grid which are not suitable for visualization. There are also less sample related issues such as isolated ice formation on the grid. The orientation and localization problems are visualized in Figure 4-4. The localization is also affected by the sample concentration, making it another subject of an obligatory optimization. Too high concentration may induce an aggravation in image processing due to features from too close laying particles and too low concentration may induce a shrinkage in the signal/noise ratio or lack of particles to overcome noise, consequently detoriating the resolution. Flexibility of a protein or its parts is naturally an important factor regarding the occupancy in the monitored particles. Since the method is based

on averaging a number of noisy images, even insignificant configurational changes within the premises of the protein result in a salient lessening of high resolution information making it harder to identify the features.

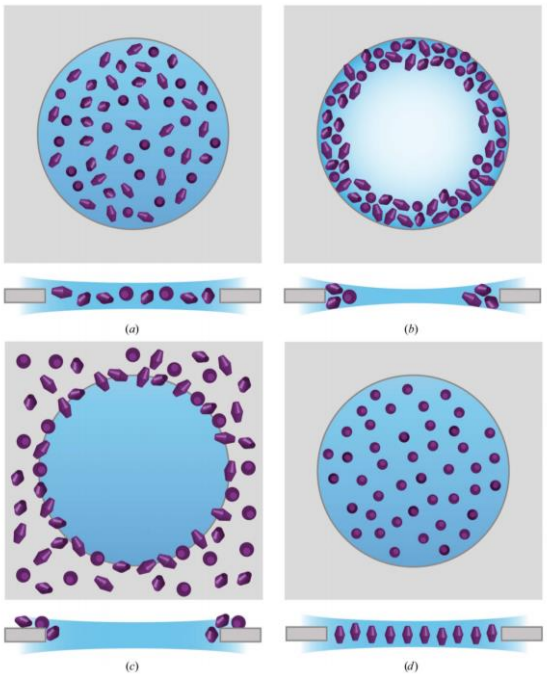

Figure 4-4 Possible Protein Orientation and Localizations During The Freezing Process. (a) Ideal vitrified sample exhibiting well dispersed particles adopting random particle orientations. (b) Particle localization close to carbon edge due to thinning of the ice in the centre of the hole. (c) Proteins affinity for the support results in exclusion from the holes. (d) Particles adopt a preferential orientation[120].

These experimental difficulties are even more severe for the structural analyses of membrane proteins. Solution state measurements require the presence of detergents in the solution for the sake of stability of the protein. The preparation of cryospecimen with particles being evenly distributed within a thin layer of vitreous ice becomes more complicated with the presense of detergent molecules within the sample due to introduced changes in the surface properties of the protein, effecting the protein behaviour and intoducing even more severity in monodispersity and localization. Moreover, a bilayer formed in the air-liquid interface not only introduces severe noise, but also a significant drop in the

surface tension of the buffer affecting the uniformity of ice formation and particle distribution within the vitreous ice.[109] Furthermore, the dynamic nature of a detergent containing buffer and the constant migration of detergent molecules between the detergent belt and the free micelles are reported to introduce a considerable level of noise and image contrast reduction.[190,191] These negative effects complicate the already troublesome vitrification process, necessiating a careful examination of sample behaviour in the presence of different detergents and time consuming screenings. However, high affinity detergents that are has a much lower migration rate and critical micelle concentration have been designed[192], that are providing the stability of a membrane proteins with a significantly lower amount of detergent and making vitrification a smoother process.

All of the experimental limitations combined with the computational limitations may be modeled by a Gaussian amplitude decay of structure factors and formulated as "$e^{-(B_{overall}/4d^2)}$", denoting the resolution. This decrease in the amplitude of structure factors affects the high resolution contrast significantly, making the maps smoother and featureless. This is overcome by a procedure termed as "sharpening", by applying the negative of the B factor computationally to the data to recover the high resolution features[121]. The decrease in the B factor brings an improvement in the noise levels and thus enhances the data. B factor is also related to the number of individual particles, as indicated by Henderson *et al*.[122], by calculating the slope of the curve defined by the logarithm of the particle numbers and the reciprocal square of the resolution. In other words, presuming that there are no resolution limiting factors except image noise, B factor plots the number of required particles for a given resolution. In a recent article of Yip *et. al.*, it is stated that to reach 1 Å resolution with apoferritin, existing state of the art commercial EM hardware requires several hundred billion particle images of the protein depending on B factor calculations[123]. However, use of cold field emission gun and monochromators with the latest detector technology is very recently reported to foster the resolution ranges to atomic level. Nakane *et al*.[178] reached 1.22 Å resolution with 363,126 particles and Yip *et al*.[179] reached 1.25 Å resolution with 1,091,000 particles of apoferritin protein, respectively.

Currently, amongst the high resolution structures deposited in PDB and EMDB, a tendency favoring the use of 300 kV accelerating voltage is evident. It has been reported that using higher values of acceleration voltage has many benefits like the increased electron penetration lengths or diminishing of multiple scattering and thus blurring[124]. On the other hand, electron microscopes operating at a maximum voltage of 200 kV can have significantly lower cost. Their design makes it easier and cheaper to compensate laboratory design requirements compared to those designed to operate at 300 kV. One important discussion in the field is the use of lower cost 200 kV microscopes for comparable high resolution structural analysis[125].

4.2 Materials and Methods

4.2.1 Sample Preparation

To eliminate the possible noise introducing effects of β-DDM and the excessive detergent micelles, a detergent exchange step from β-DDM to GDN was performed using the GraDeR approach[109]. Briefly, PSI monomer fractions were administered to a sucrose/GDN step gradient (20 mM HEPES-NaOH, pH 7.0, 10 mM $MgCl_2$) of 0.1 M and 1.3 M sucrose and 0.02% and 0.003% GDN. After a centrifuge of 18 hours at 97,000 g and 4°C using a P40ST rotor and a CP70MX ultra-centrifuge (Hitachi Koki), sucrose was removed and sample was concentrated to 5 mg/ml using Amicon Ultra-100k concentrators. 10 µl aliquots of PSI monomer were flash-frozen in liquid N_2 and stored at -80°C. An aliquot of 2.6 µl PSI monomers at 5 mg/ml in a buffer of 10 mM $MgCl_2$, and 20 mM HEPES (pH 7.0) and 0.0005% GDN was applied to glow discharged (JEC-3000 FC, 30 s) Quantifoil holey carbon-supported copper grids (R 1.2/1.3, 300 mesh), blotted (Whatman #1) and plunge-frozen in liquid ethane using an FEI Vitrobot Mark IV at 4°C and 95% humidity.

4.2.2 Negative Staining

After purification by Protocol II, negative stain EM was used to assess sample quality of PSI monomer preparations and investigate the appropriate detergents for cryo-EM. An aliquot of 3.5 µl protein solution with ~100x dilution was casted on glow-discharged (10 s at 5 mA) continuous carbon film coated copper grids (Nisshin EM) and staining was done using a 2% uranyl acetate solution. After a

quick blotting (Whatman #1), the grid was dried in room temprature and inspected using an H-7650 HITACHI electron microscope at 80 kV, equipped with a 1 x 1 K Tietz FastScan-F114 CCD camera (TVIPS, Gauting, Germany).

4.2.3 Data Acquisition

Image acquisition was performed on a CryoARM200 (JEOL) with a field emission gun and operated at 200 kV using flood beam illumination in bright field imaging mode. No screening was done and one out of three prepare grids were used for the measurements. Movies were recorded using a K2 Summit detector (Gatan) in counting mode at a nominal magnification of 60,000× at the camera level, corresponding to a pixel size of 0.89 Å with 60 frames at a dose of 1.34 $e^{-}/Å^2$ per frame and an exposure time of 12 seconds per movie resulting in a total dose of 80.4 $e^{-}/Å^2$. A small dataset consisting of a total of 1,530 movies were collected in series within a defocus range of 0.5 µm to 3.5 µm using JADAS software (JEOL)[126].

4.2.4 Cryo-EM Image Processing.

All image processing was performed using RELION 3.0[127] , cryoSPARC[128] , and UCSF CHIMERA[129] on a GPU workstation (2 GPUs). Alignment and summing of the movie frames and the estimation of the contrast transfer function (CTF) were carried out as the initial steps of image processing by MotionCor2[130] CTFFIND4[131], respectively. Thon rings of the resulting micrographs were inspected to pinpoint the contaminations or bad particle localizations on grid. ~40% of the micrographs were discarded at this step. Remaining 1,107 micrographs were subjected to automatic particle picking by Laplacian of Gaussian rendering a total number of 1,217,859 particles with a box size of 256 pixels. A reference-free 2D classification was applied on the extracted particles. Best 2D classes showing representing the PSI monomer were used as templates to autopick 227,910 particles. A manual investigation of the remaining micrographs is administered to expel particles on the carbon film and minimize the the noise, narrowing the partice number to 182,018 for extraction. To eliminate all the bad particles remaining in the dataset that are similar enough to form 2D classes as well as the ones hidden in the good 2D classes, successive rounds of 2D classification was employed. This constricted the number of particles to 46,515, stripping the dataset from the noisy particles and the particles

exhibiting strong features from their neighbours. De novo initial model building in Relion software generated irrelevant 3D volumes, most probably due to the effects from neighbouring particles. However, cryoSPARC software produced a very well defined initial model that the α helices were clearly distinguishable. The initial model was imported into Relion and used as a reference for 3D classification which resulted in further elimination of 410 particles. The remaining 46,105 particles were refined against the initial model followed by CTF-refinement and Bayesian polishing. These three steps iteratively repeated using the postprocessing job for probing the B factor and resolution using the Gold Standard FSC criteria. The iteration continued until there was no more improvement in B factor and resolution. These iterative per particle corrections enhanced the B factor from -122 to -45. To investigate if lower resolution/ flexible parts of the protein involved different conformations of subunits, additional focused classifications were tried for all peripheral subunits. These trials on low-density regions did not yield any improvements. Local resolution was calculated by Resmap[132] in RELION on the full density map without masking. Resolvability and Q-scores were calculated using MapQ, a USCF Chimera plug-in[187].The workflow of image processing is schematized in Figure 4-5.

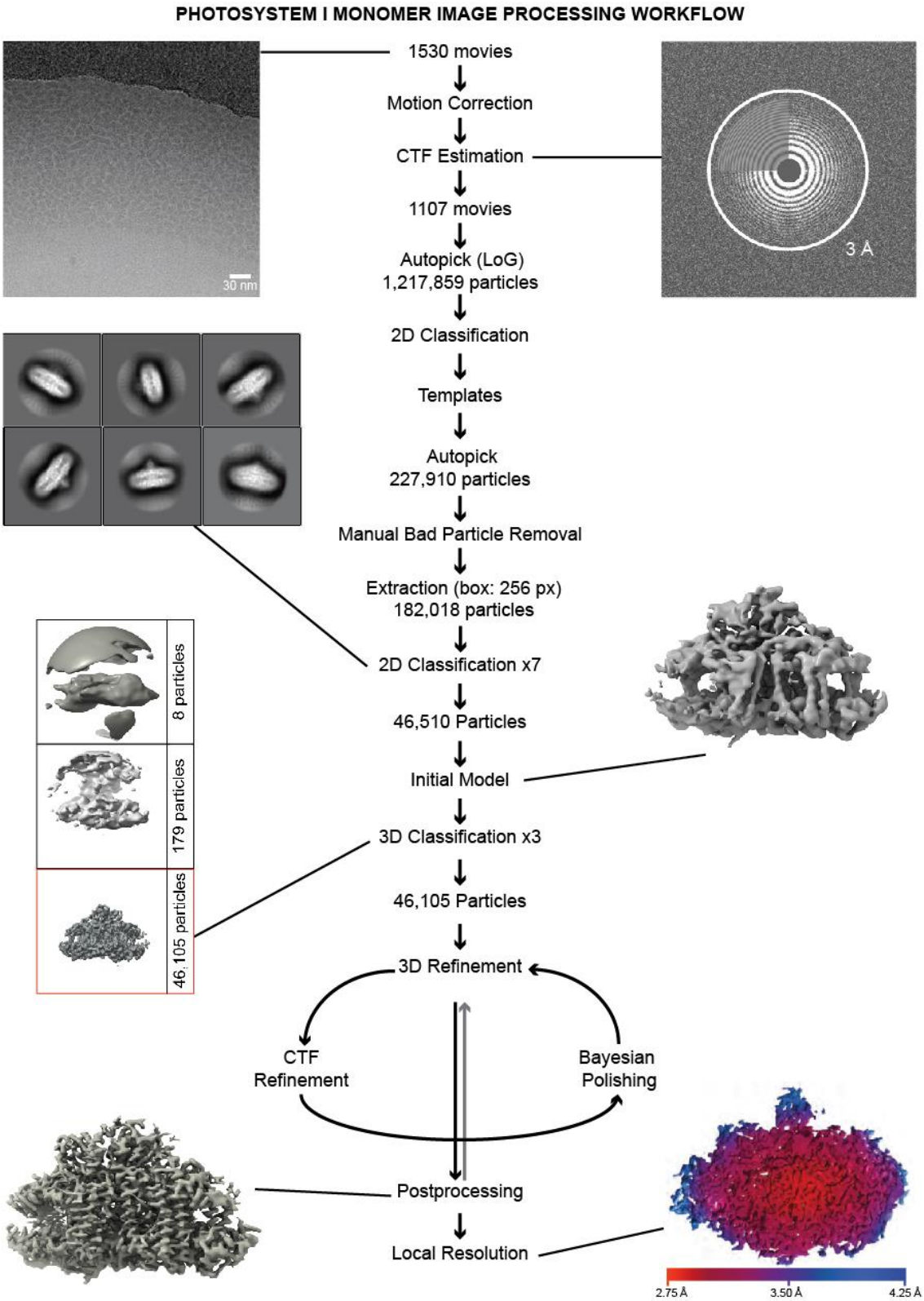

Figure 4-5 Workflow of Image Processing, with screen shots from motion correction, CTF estimation, 2D classification, initial modelling, 3D classification, postprocessing and local resolution jobs.

4.2.5 Atomic model building and refinement.

Coot 0.8.9.1[105] , Phenix 1.14-3260[133] , and UCSF Chimera/ChimeraX[129,107] were used for fitting, modeling, refinement and visualization. Since PSI monomer is cognate with PSI trimer (used as the starting model), the modelling strategy is tailored as an iterative approach fostering a step by step model manipulation process to make use of the presumable structural similarities. In each step, a transfiguration is followed by successive manual modifications in Coot and real space refinements in Phenix, until validation statistics do not improve anymore. As a first step, the *T. elongatus* PSI trimeric cyrstal based atomic model (PDB ID: 1JB0) was fitted to the final cryo-EM Coulomb map in Chimera. After modulations at α-helical level, amino acid residues corrected and ligands were only subjected to rigid body refinement. These corrections were followed by a real space refinement with CSD Mogul[197] substructure restraint files in Phenix. These two processes were repeated iteratively until the diminishing of betterment in validation statistics. For the second step, all constituents of the manipulated trimeric model corresponding to meager regions of the density map were erased. Another loop of manual corrections and postdating real space refinements was iteratively carried out until the consolidation of the validation statistics. In the final step, a final round of real space refinements and manual corrections was performed using more accurate ligand restraint files. For β-carotene and chlorophyll *a*, restraint files calculated by the Grade Server (http://grade.globalphasing.org)[134,198] and for the iron sulfur cluster, recently deposited restraint files created by Moriarty and Adams (sourceforge.net/projects/geostd/)[135] were employed. The modelling was terminated when the validation statistics ceased improving.

4.3 Results

4.3.1 Negative Staining

Negative staining was used for investigating the sample quality. Samples varying in detergent content were also screened to acquire a sense about the behaviour of the proteins. The samples with different detergent ingredient were prepared by the grader approach. Two different bands were observed in the GDN sample.These bands are investigated with BN-PAGE in addition to negative

staining. BN-PAGE and sucrose density gradient results are shown in Figure 4-6.

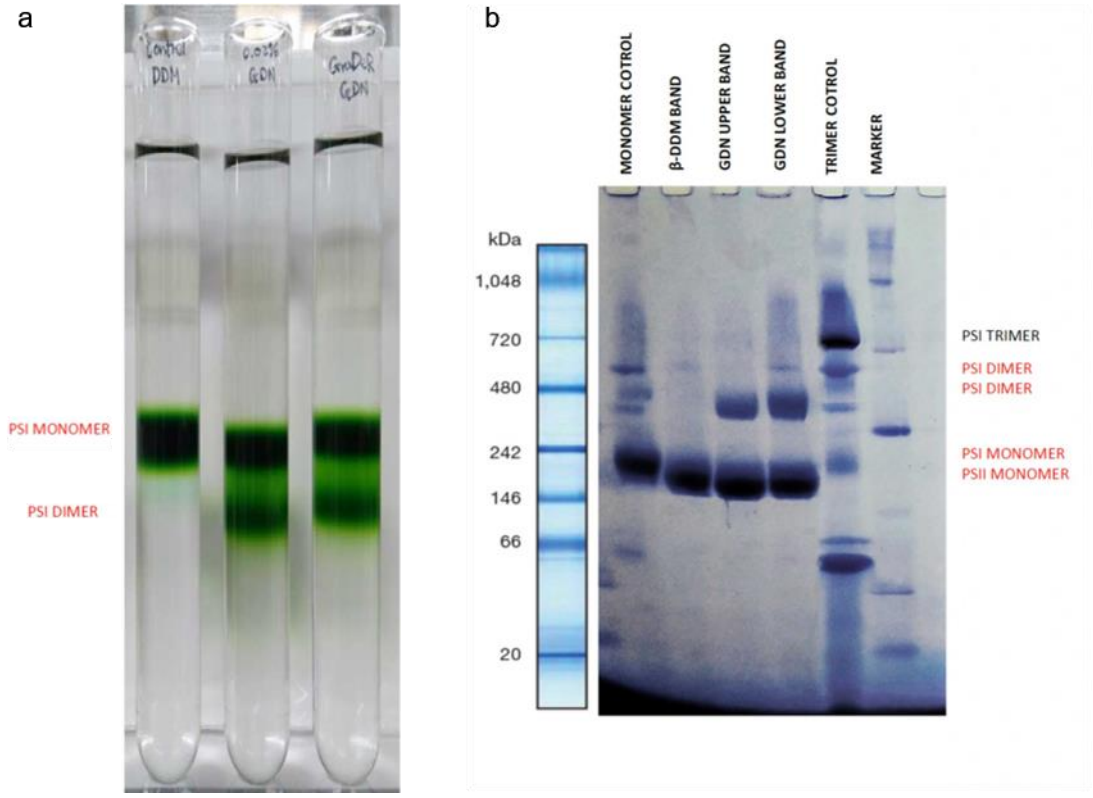

Figure 4-6 Biochemistry of Detergent Exchanged Particles a) The sucrose gradient after the detergent exchange. The first gradient is a control of B-ddm sample, the second and third tubes are with GDN. b) BN-PAGE of the bands from the SDG.

The micrographs obtained from negative staining of the PSI purified by Protocol II are shown in Figure 4-7. In addition to the samples investigated by BN-PAGE and sucrose density gradient, a mixture of GDN and LMNG detergents were also investigated by the negative staining, shown in Figure 4-7.(e,f). The behaviour of the proteins to attach together and the tendency to aggregate is clearly seen in these micrographs.

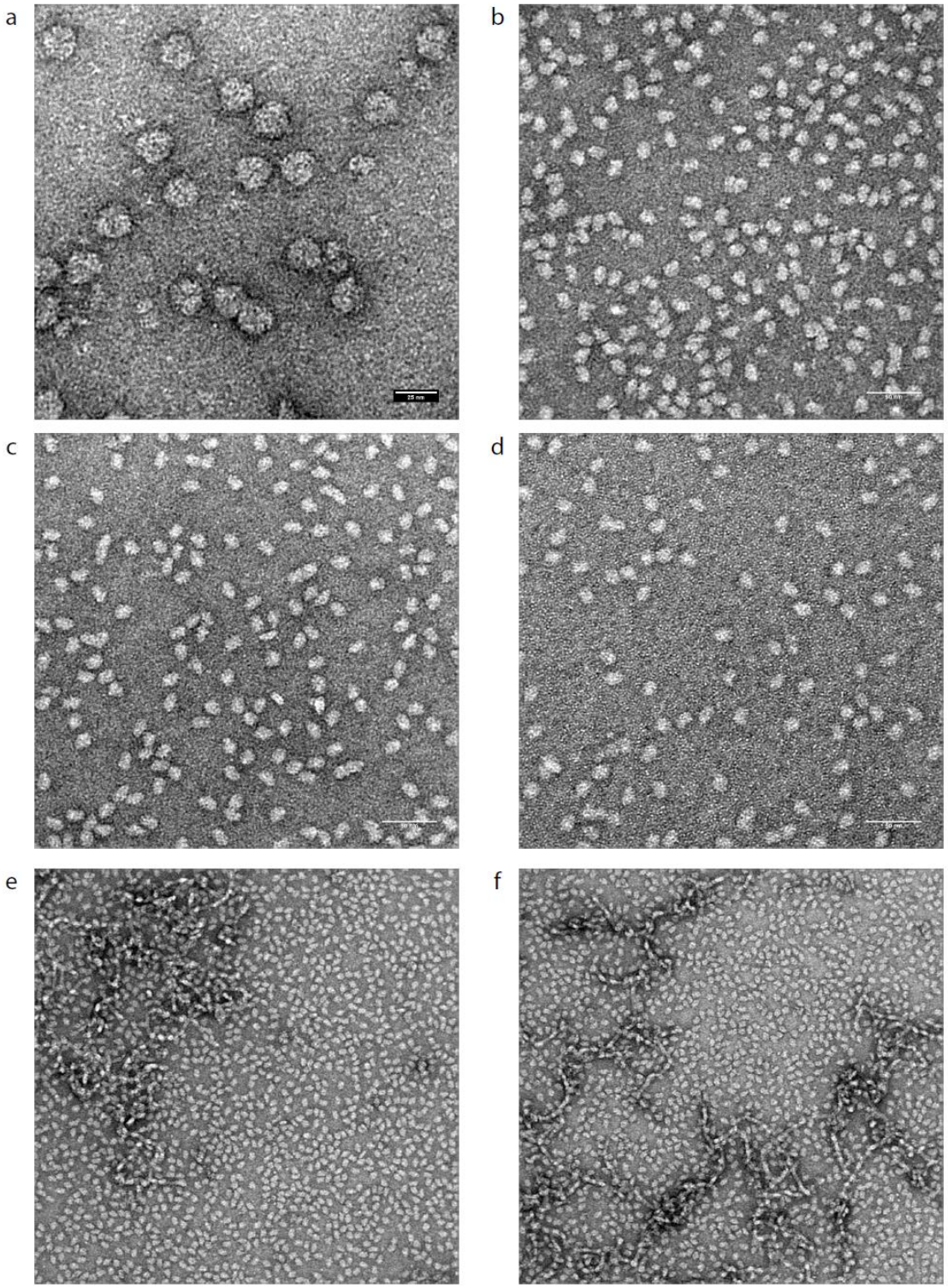

Figure 4-7 Negative Staining. a) Micrograph of PSI trimers with β-DDM, purified by Protocol II, scale bar is 25 nm, b) includes the sample with β-DDM,c,d Micrograph of PSI monomers purified by Protocol II after the detergent excange. Scale bars are 50 nm. , c) is the upper band of SDG, d) is the lower band of SDG after the detergent exchange., e,f) Sample with a mixture of GDN and LMNG detergents.

4.3.2 Cryo EM Data Acquisition and Image Processing

The same sample investigated by negative staining was used for Cryo-EM microscopy. However the sample quality was good, as a result of application of too dense sample on the grid and problems in the image acquisition software, the resulting images had severe problems. Sample micrographs are shown in Figure 4-8.

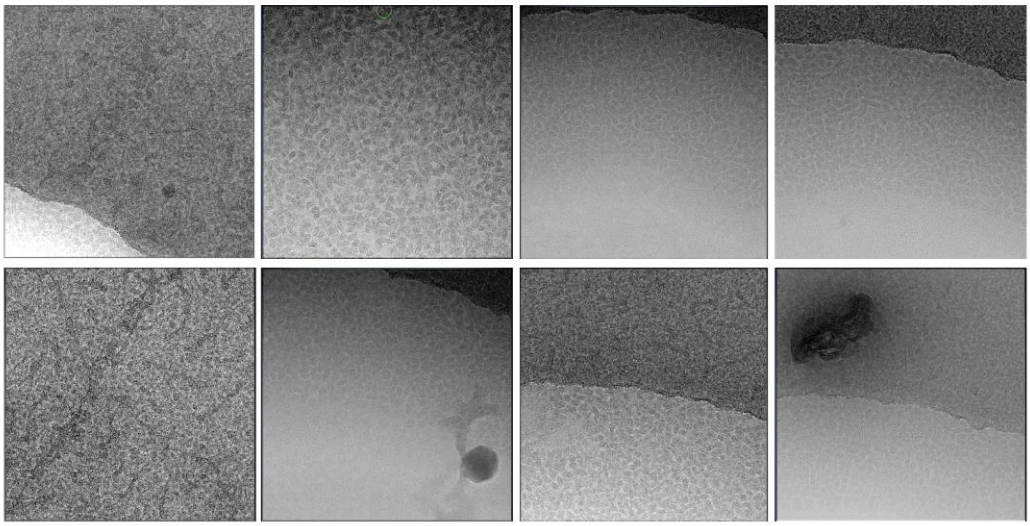

Figure 4-8 Sample Micrographs Representing The Problems in The Dataset

A sample of the estimated contrast transfer functions of randomly picked micrographs showing how the selection was done is shown in Figure 4-9.

A preliminary and straightforward image processing strategy venturing to make use of all the autopickable particles regardless of their location on the grid and noise level resulted in a failure in constructing an initial model. However, carefully eliminating all the particles suffering from higher noise levels and close neighbour features made it possible to make a high resolution analysis. 2D classes, initial model, 3D classes, final map and the local resolution of the final map are shown are shown in Figure 4-5.

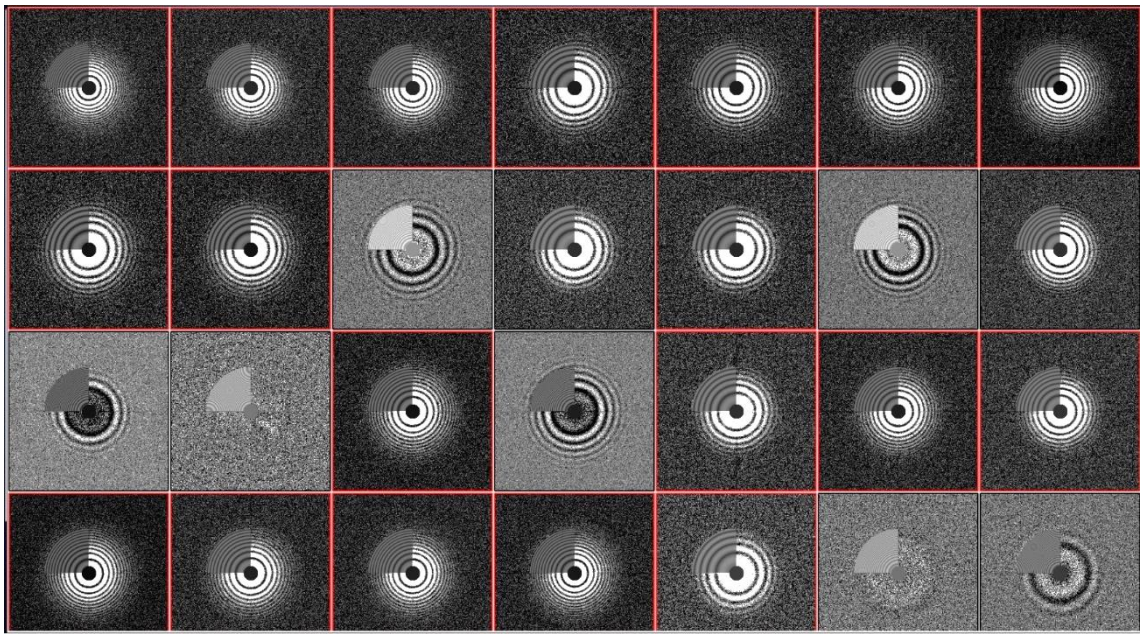

Figure 4-9 A Sample Screenshot From CTF Estimation Job. The squares with a red perimeter are selected as good micrographs, others are eliminated.

The change in the B factor with respect to the resolution throughout the workflow of image processing is shown I Figure 4-10.

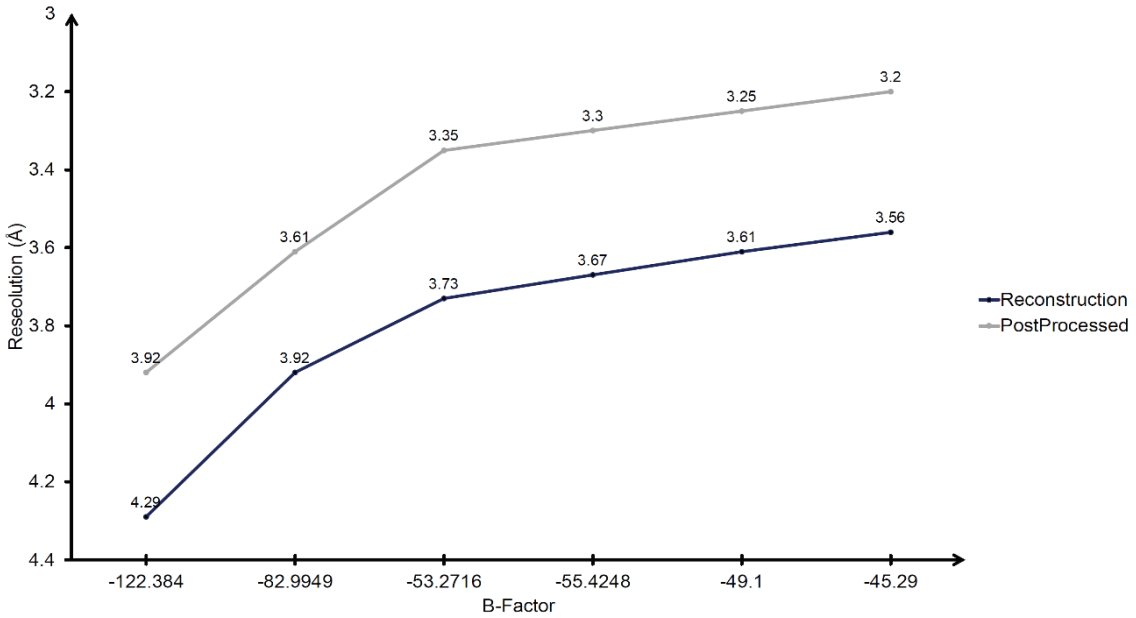

Figure 4-10 The Change in the B Factor with Respect to Resolution Throughout the Image Processing. All the resolution points shown in the graph correspond to a postprocessing job after CTF refinements and polishing jobs in relion 3.0.

The particles used in the last refinement were observed to have an orientation distribution far from ideal, yet the preference behavior in cryo conditions did not prohibit image analysis due to an even radial distribution of Euler angles. The final map had a resolution of 3.2 Å (Gold Standard FSC cut-off at 0.143) with a local resolution ranging from 2.75 Å at the core to 4.3 Å in the peripheral region. Euler Angle Distributions and the Fourier Shell Correlation curves are shown in Figure 4-11.

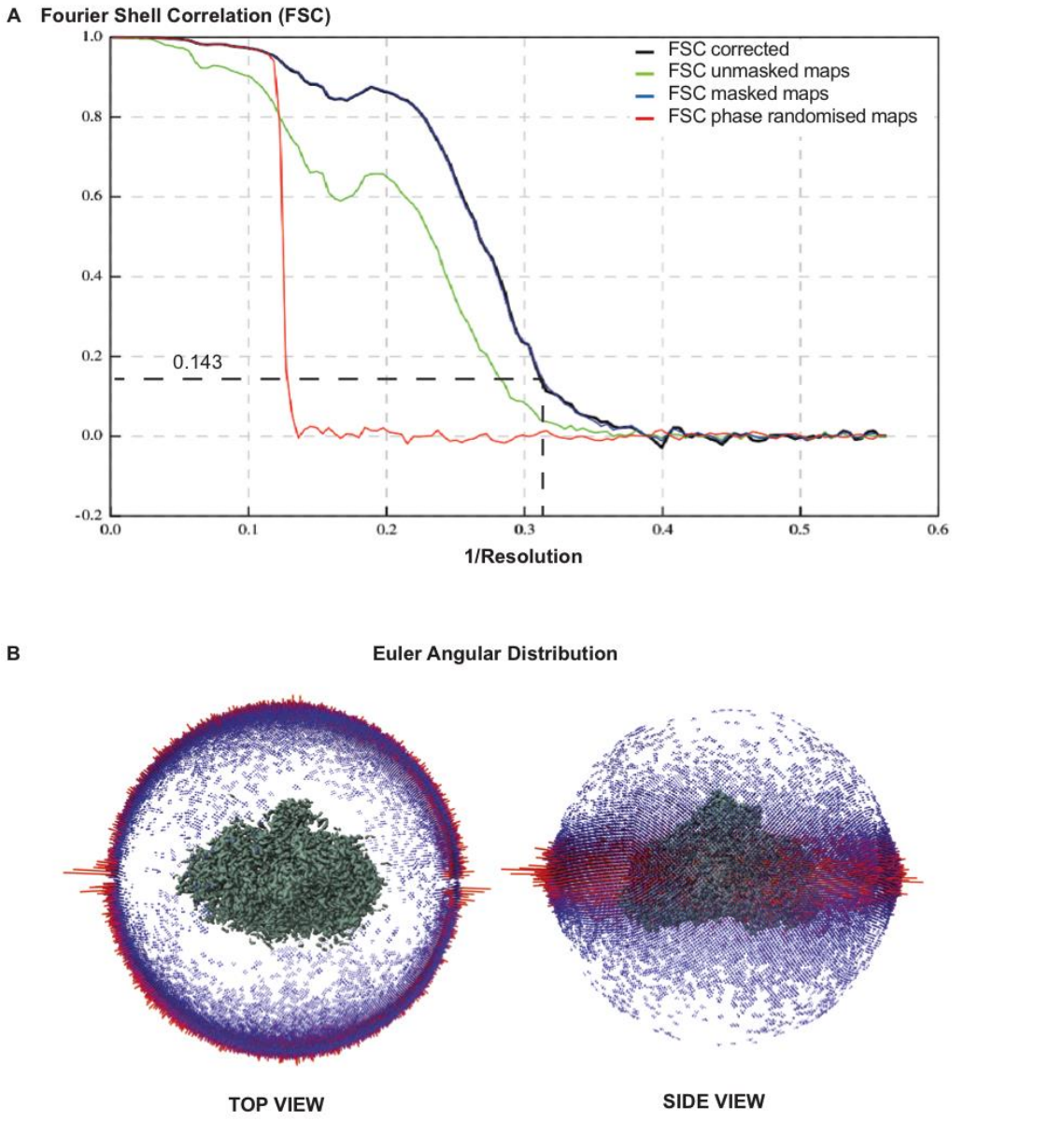

Figure 4-11Cryo-EM Map Quality a Fourier Shell Correlation curves of the final map showing the resolution b Euler Angle Distributions of the particles in the final dataset.

4.3.3 Model Building

After obtaining the map, A model from trimeric crystal structure (PDB ID: 1JB0) was fitted into the map using UCSF Chimera and a new model was produced by employing real space refinements. Validation statistics of the final model are shown in Table 4-1. with a comparison to related models in the same resolution levels from Protein Data Bank.

Table 4-1 Comparison of Final Model with related models at similar resolution by means of validation statistics

	6LU1	1JB0[29]	6HQB	6K61
Resolution (Å)	3.2	2.5	4.0	2.37
Sidechain outliers	%0.1	%4.4	%3.9	%0.1
Main Chain Bond Length Outliers	0	0	0	5
Main Chain Bond Angle Outliers	2	15	0	16
Main Chain Bond Chirality Outliers	9	0	0	0
Main Chain Bond Planarity Outliers	0	1	0	8
All Atom Clash Score	3	16	14	7
Close Contacts	125	743	666	585
Ramachandran Outliers	0	37	21	6
Non-rotameric Sidechains	0	78	70	36
Ligand Bond Length Outliers	239	642	532	1178
Ligand Bond Angle Outliers	563	1340	1073	2403
Ligand Bond Chirality Outliers	248	249	279	563
Ligand Bond Torsion Outliers	476	831	8	2594
Monomers in Short Contacts	73/91	114/339	116/375	119/391

Resulting 3.2 Å model was deposited to PDB with the accession code 6LU1 and to EMDB with the accession code 0977. The raw data is deposited to EMPIAR database with the accessio code 10352.The cryo-EM information of the resulting model can be seen in Table 4-2.

Table 4-2 Data collection, map reconstruction and model building information of 6LU1

DATA COLLECTION	
Microscope	JEOL cryoARM200
Voltage (kV)	200
Camera	Gatan K2 Summit
Defocus Range (μm)	0.5-3.5
Exposure Time (s)	12
Number of frames per image	60
Electron Exposure (frame/total) ($e^-/Å^2$)	1.34/80.4
Pixel Size (Å)	0.89
RECONSTRUCTION	
Micrographs (Initial/Final)	1530/1107
Particles (Initial/Final)	227910/46105
Box Size (px)	256
Symmetry Imposed	C1
Map Sharpening B-factor ($Å^2$)	-45.29
FCS Treshold/Map Resolution (Å)	0.143/3.2
EMPIAR Accession Code	10352
MODEL REFINEMENT	
Initial Model	1JB0
Non-hydrogen Atoms	21203
Protein Residues	1986
Ligands	121
R.M.S.D. (Bonds (Å) /Angles (o))	0.011/1.181
Ramachandran Favored (%)	95
Ramachandran Allowed (%)	5
Ramachandran Outliers (%)	0
Poor Rotamers	0.06
Molprobity Score	1.49
Clashscore	4
EMRinger Score	3.87
PDB Accession Code	6LU1
EMDB Accession Code	0977

The final model, final map and the local resolution distribution of the final map are shown in Figure 4-12.

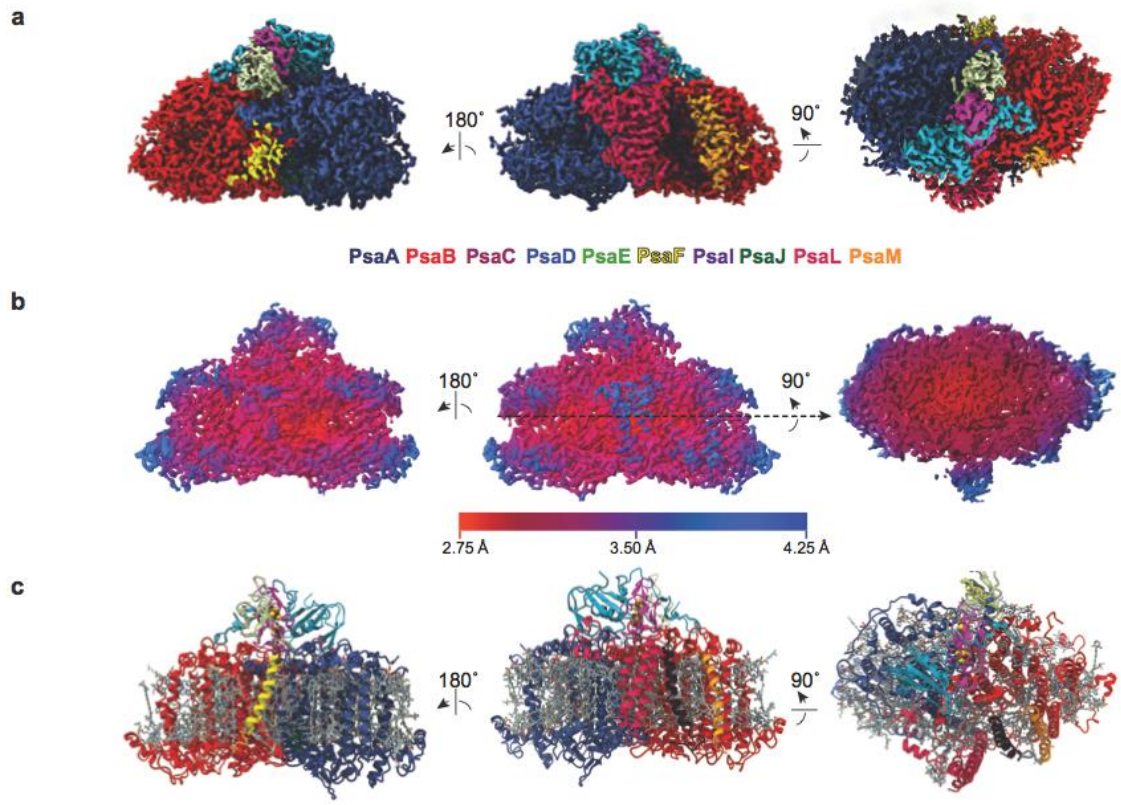

Figure 4-12 Overall Structure of The PSI Monomer From *T. elongatus*. a) The 3D cryo-EM coulomb density map of the PSI monomer viewed parallel to membrane from the membrane side (Left), trimerization side (middle), and viewed along the membrane normal from the stromal side. Map regions are colored according to the fitted model following the color scheme indicated by the subunit name font color. b) Local resolution map of the PSI monomer viewed parallel to membrane from the membrane side (left), trimerization side (middle), and viewed along the membrane normal from the stromal side. Coloring by local resolution as indicated. c) The structural model of the PSI monomer viewed parallel to membrane from the membrane side (Left), trimerization side (middle), and viewed along the membrane normal from the stromal side. Coloring of subunits as in a.

A meticulous model comprising information about amino acid residue conformations, ligands binding and flexiblility of PSI in solution state was constituted using the Coulomb density map. The appearance of monomeric PSI matches that of a curling stone with the stromal subunits PsaC, PsaD and PsaE outlining the knob (Figure 4-12 a). The overall structure of monomeric PSI is predominantly the same as trimeric PSI. However, significant differences were observed at the α-helical level and in ligand content, particularly at the peripheral regions. These disparities comprise of a conformational change in the

trimerization interface bred by the C-terminal region of PsaL, a disordered loop-helix-loop motif in PsaB (B291-B316), a partial flexibility of PsaF and PsaJ subunits, impartial flexibility of PsaK and PsaX subunits in addition to occupational changes of peripheral chlorophylls and carotenoids. PSI monomer model contains ten protein subunits featuring seven transmembrane subunits PsaA, PsaB, PsaF, PsaI, PsaJ, PsaL, PsaM and the three extrinsic stromal subunits PsaC, PsaD, PsaE. It accommodates a total of 112 cofactors (Figure 4-12 c). Subunits and cofactors were found to be positioned akin to their trimeric counterparts retaining the same side chain coordinations to the metals. Coordination of the cofactors by the protein is preserved between the monomeric cryo-EM structure and the trimeric crystal structure. Novel additions to the trimeric structure-based model (PDB ID 1JB0) are residues A11-A12, A262-A265 along with 8 new carotenoids. The flexibility of the subunits was measured with the percentage of the modelled aminoacid residues. The flexibility comparison of the trimeric structure and the monomeric structure is shown in Table 4-3. An additional calculation was done do define the resolvability of the subunits and the pigments, quantifying the flexibility of the modelled entities. Q scores are listed are also shown in Table 4-3.

Table 4-3 Percentage of modelled residues, Q scores and estimated resolutions for 6LU1 and 1JB0 subunits and pigments

SUBUNIT	6LU1 RESIDUES MODELLED (%)	1JB0 RESIDUES MODELLED (%)	Q SCORE / ESTIMATED RESOLUTION (Å)
PsaA	95	95	0.71 / 2.30
PsaB	95	100	0.70 /2.37
PsaC	98	100	0.69/2.41
PsaD	99	100	0.68 / 2.50
PsaE	91	92	0.64 / 2.69
PsaF	18	86	0.48 / 3.54
PsaI	100	100	0.65 / 2.62
PsaJ	20	100	0.52 / 3.40
PsaK	0	55	-/-
PsaL	87	95	0.64 / 2.68
PsaM	100	100	0.66 / 2.59
PsaX	0	83	-/-
Chlorophyll A	-	-	0.71 / -
Carotenoids (All)	-	-	0.61 / -
Carotenoids (New)	-	-	0.53 / -

An assortment of snapshots from different regions of the model with the surrounding map is shown in Figure 4-13. The map quality was sufficient to resolve amino acid residues, ligands and their interactions. As an additional comparison, whole electron transfer chains of the resulting monomeric model and the trimeric model with the distances between the components of the chain are shown too.

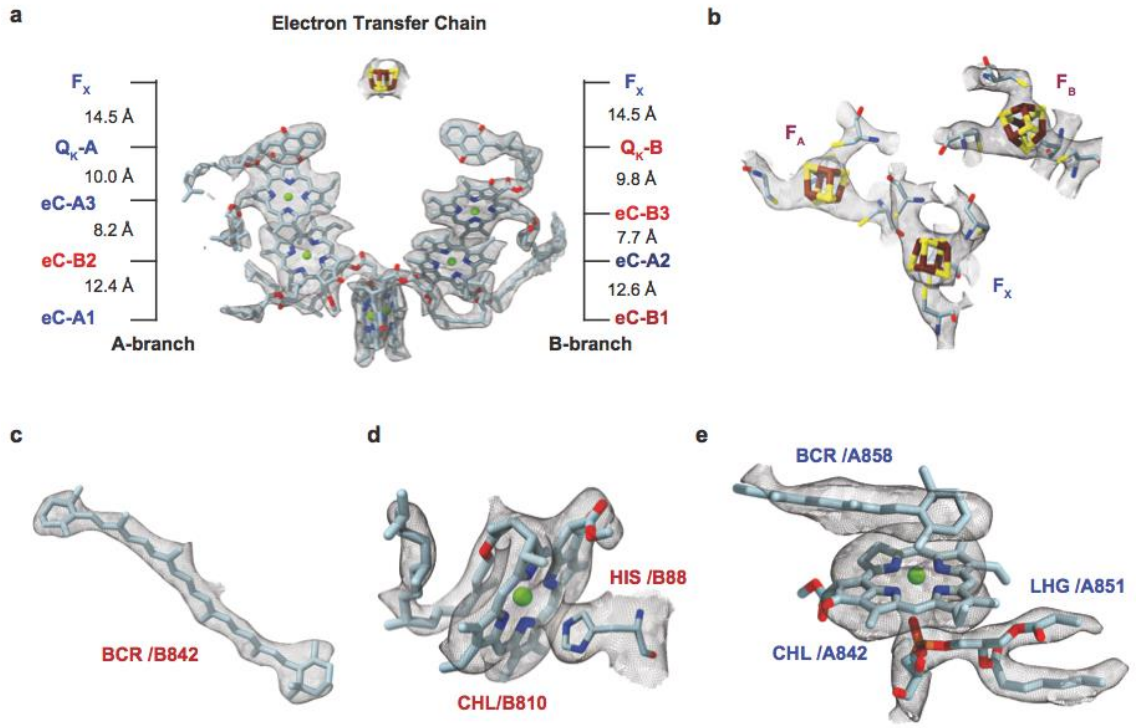

Figure 4-13 Selected Cofactors and Their Corresponding 3D Cryo-EM Coulomb Density Map. a) The electron transfer chain (ETC) of monomeric PSI viewed parallel along the membrane plane. Distances between the A-branch and B-branch measured between magnesium atoms of neighboring chlorophylls, magnesium, and center of the carbonyl ring of neighboring chlorophyll and phylloquinone and center of the Fx iron-sulfur cluster and center of the carbonyl ring of the neighboring phylloquinones are indicated. b) The three iron-sulfur clusters Fx, FA and FB of the PSI monomer. c) A fully modeled carotene with visible polyene chain methyl bumps in the density map. d) A chlorophyll coordinated by a histidine residue and its own phytol chain. e) A chlorophyll coordinated by a lipid and a newly found carotenoid.

4.4 Discussion

The two bands observed in the SDG upon detergent exchange indicates a possible change, or an aggregation behaviour upon detergent exchange.

However, investigation by BN-PAGE shows that the sample consists of solely monomeric particles (Figure 4-6). The reason of this band seperation in SDG is not known. Inclusion of LMNG to the buffer shows the aggregation behaviour of the proteins on the grid (Figure 4-7 e,f). This negative stain based screening was decisive for the detergent to use in cryo-EM measurements. As visible from the micrographs, detergent exchange with GDN not only improved to contrast (possible due to lower noise) but also resulted in removal of small contaminants. This effect is thouht to be very effective in reaching high resolution with such a small dataset and only one measurement.

Cryo-EM measurements with the cryoARM200 provided an atomic model with all the components of the protein at residual level, however it was not possible to model the majority of the water molecules or the Ca^{+2} ion in the structure. This model is one of the 50 highest resolution structures generated by a 200 kV EM, and the fifth highest resolution structure amongst the membrane proteins obtained with the same acceleration voltage despite the imperfect sample condition. Considering the discussions about the necessity of 300 kV machines and the limits of 200 kV machines, these results support the argument that much more accessible 200 kV microscopes provide sufficient quality for near atomic resolution analysis of membrane proteins.

Considering the sample condition shown in the results section, it was necessary to define a unique strategy. The preliminary image processing evinced the particles introducing higher noise levels to the dataset are detrimental and cripple the whole image processing. Therefore, despite the fact that the number of particles has a linear relationship with the resolution, the strategy is devised to eliminate bad particles as much as possible to obtain higher resolution. However, eliminating the particles in the carbon regions of the grid was not sufficient to obtain good 2D classes. The closeness of the remaining particles resulted in strong effects observable in the 2D classification step. Most of the classes included some neighbouring density from the neighbours. An optimization of box size was administered to eliminate neighbouring effects and an iterative classiffication was utilized to uncover and discard the covert bad particles that were included within the good classes. Owing to this strategy it was possible to acquire good 2D classes.

As a second part of the image processing, extensive per particle corrections were employed using Bayesian Polishing and CTF Refinement jobs of RELION iteratively. The elimination of neighbour effects was important to obtain better results from per particle corrections too.

After every refinement, CTF refinement and Bayesian polishing were employed. Following these jobs, another 3D refinement succeeding a postprocessing job was employed to observe the change in the B factor. The improvement of B factor throughout these per particle corrections shows that, even with a very small dataset, it is possible to minimize the resolution limiting factors given that dataset consists of only properly imaged particles.

Validation statistics of the monomeric model is superior to that of the similar PSI structures in the resolution range of 2.3 Å – 4 Å . This may be explained by the quality of the map provided by the unique image processing strategy. Total number of the loops of manual corrections and real space refinements from the anchoring of the trimeric crysta structure (PDB ID: 1JB0) to the Coulomb density map to the termination of modelling is 248. A gradual improvement of the validation statistics following the pattern of step by step modelling summed up to significant improvements for nearly all of the validation parameters, even when they are compared to deposited higher resolution structures. Considering the fraction of clashes including the ligands, specifically chlorophyll molecules, the improved restraint files were exclusively effective in improving statistics. In order to check the effect of the restraint files and to test whether the variance in co-factor distance between two structures of trimeric X-ray (1JB0) and monomeric Cryo-EM (6LU1) (Figure 4-3 a) stems from differences in the structure or is the result of different refinement strategies, the final model was re-refined using CSD Mogul restraints instead of Grade server restraints[136]. A comparison between the distances of these structures and similar structures in the same resolution range are shown in Table 4-4. For this comparison, ETC is chosen since it is in the best resolved region in the current model. The RMSZ values for bond lengths and bond angles define how the geometry of a modeled molecule satisfies the restraints[134]. For the ETC chlorophylls in the model, these values lie between 0.84 and 0.95 for bond lengths and between 0.94 and 1.17 for bond angles as an indicator of the sturdiness in this region. Moreover, its archaic yet substancially

unaltered structural organization for transferring electrons at very high efficiency from a lumenal donor (plastocyanin or cytochrome c_6) to stromal side electron acceptors (ferredoxin or flavodoxin) accentuates ETC. This mechanism involves the transfer of excitation energy to the primary electron donor P700 upon light absorption and transfer of electrons are through the A-branch or the B-branch along A_0 (two pairs of Chl *a*), A_1 (a pair of phylloquinones), iron-sulfur cluster F_x and eventually to the two iron-sulfur clusters of PsaC for the subsequent delivery to the stromal side electron acceptor ferredoxin (or flavodoxin) [25].

Table 4-4 Effect of the restraints on distances between ETC components

	Coruh et al. (2020)	Coruh et al. (2020)	Jordan et al. (2001)	Suga et al. (2019)	Zheng et al. (2019)	Netzer-El et.al. (2019)
PDB-ID	6LU1	-*	1JB0	6JO5	6K61	6HQ1
METHOD	Cryo-EM	Cryo-EM	X Ray	Cryo-EM	Cryo-EM	X Ray
RES.	3.2 Å (2.7 Å**)	3.2 Å (2.7 Å**)	2.5 Å	2.9 Å (2.5 Å**)	2.4 Å (2.2 Å*)	4 Å
			Distance (Å)			
A1-B2	12.4	12.0	11.7	11.9	12.1	12.3
B1-A2	12.6	12.0	12.0	11.9	11.8	12.2
B2-A3	8.2	8.7	8.8	7.9	8.3	8.3
A2-B3	7.7	8.4	8.2	7.6	7.9	7.8
A3-Q_KA	10.0	10.3	8.6	9.0	9.3	9.5
B3-Q_KB	9.8	10.1	14.2	8.6	8.9	9.0
Q_KA-F_X	14.5	14.6	14.1	14.4	14.1	13.9
Q_KB-F_X	14.5	14.9	14.9	14.5	13.9	14.2
F_X-F_A	15.8	15.7	14.9	14.9	15.1	14.7
F_X-F_B	12.6	12.6	12.3	12.3	12.3	12.0

**A refinement of final model with CSD Restraints*

***Highest local resolution observable in the deposited map.*

Distances between the cofactors of both ETC branches as measured according to Jordan *et al*. between magnesium atoms of chlorine rings, the center of the carbonyl ring of the phylloquinones and centers of the iron sulfur clusters were in variance from that of the trimeric crystal structure. Changing the restraint files clearly impacted the distances between ETC cofactors. This outcome and also a comparison with ETC cofactor distances in more recently published, high-

resolution cryo-EM structures of other PSI suggests that at the current resolution level, the influence of the refinement strategies is not insignificant. A fact that underlines the need for structures of PSI, resolved at true atomic resolution for the determination of accurate cofactor geometry in the ETC.

Since the sample was througly investigated by biochemical and biophysical means as explained in Chapter 2, it is presumed that the relatively lower resolution in the periphery is related to the flexibility in this region. Comparing with the crystal structure at lower resolution (Chapter 3), it may strongly be stated that the flexibility stems from the protein being in the solution state rather than a crystalline state and thus lacking stabilizing neighbours.

CHAPTER V.

STRUCTURAL ANALYSIS OF MONOMERIC PHOTOSYSTEM I

5 STRUCTURAL ANALYSIS OF MONOMERİC PHOTOSYSTEM I

5.1 Introduction

As a result of the explained experiments in Chapter II, Chapter III and Chapter IV, it was possible to solve the structure of monomeric PSI from *Thermosynechoccoccus elongatus* at 6.5 Å resolution with X-ray diffraction and 3.2 Å resolution with single particle cryo electron microscopy. These are the second and third monomeric photosystem I structures published until today, according to Protein Data Bank. Depending on the methodological differences between X-ray crystallography and cryo-electron microscopy (cryo-EM), these models complement each other to provide a better structural information. Due to the stabilization of peripheral subunits by formation of crystal contacts, the periphery is less flexible in X-ray structure, confirming the flexibility of the non-modelled subunits in cryo-EM structure. On the other hand, due to the resolution difference, cryo-EM structure provides valuable information about the conformations of ligands and amino acid residues.

It has been reported that the trimeric state of PSI is especially essential in low light conditions[102]. Being an assemble of 12 different protein subunits, each of the monomers are defined as functional units of the oligomers. However, despite its revealed structure, one of these subunits, PsaX, is still not fully sequenced and its function is still not explicitly desribed[174].

One of the unclear issues is the oligomerization mechanism of photosystem I. Although the role of PsaL in monomerization of PSI has been proven by a study of ΔPsaL mutants, the exact mechanism has not been reported yet, possibly due to lack of monomer structures of PSI at the time[139]. Recent report on the only monomeric PSI structure from *Synechococcus sp.* has revealed that the terminal helix loses its secondary structure due to the addition of a terminal histidine to that region. As this addition terminated the trimeric formation in the cell, the authors interpreted this observation to hypothesize that stability of this helix is a prerequisite for monomers to form contact with other monomers[39].

A half a century old discussion stemming from the functional differences of monomeric and trimeric PSI is about the light absorption properties[140]. Only a few decades ago, it was observed that the long wavelength absorption of PSI differs between monomers and trimers[38,50,52]. Upon the publication of the trimeric PSI

structure[28], many experiments and calculations have been conducted to identify the long wavelength absorbing “Red Chlorophylls” of PSI. Owing to spectroscopic work, these 'Red' chlorophylls are defined as pigments allowing an uphill excitation energy transfer to P700 for its oxidation by the low energy light (wavelengths beyond 700 nm) and the thermal energy supplied by the vibrations of the surrounding phonon bath, effectively expanding the light spectrum available for electron pumping[53,54,55]. Even though different kinds of chlorophylls take the role of long wavelength absorptions in different organisms[59,141], *T. elongatus* PSI has chlorophyll *a* only and it still absorbs in the red region. This indicates that absorption spectrum of the chlorophylls of PSI is tuned by the interactions of some PSI cholorophylls with their surroundings. These interactions may involve the ligation of chlorophylls with water, chlorophyll-chlorophyll molecular orbital interactions, chlorophyll-carotenoid interactions, chlorophyll amino acid interactions, chlorophyll-phonon (vibrational energy of the whole protein) interactions. Thus far, three concrete absorption bands at 708 nm (C718), 715 nm (C715) and 719 nm (C719) have been identified in the red edge of the spectrum by room temperature spectroscopy[56,57,58]. The release of the atomic model of trimeric crystal structure (PDB ID: 1JB0) shaped up the ground for more detailed theoretical and experimental work, leading to more attentive studies regarding the identification of red chlorophylls. As a result, ~9 'red' chlorophylls per PSI monomer has been estimated on the basis of spectroscopical measurements, ~4 of them are proposed to absorb at 708 nm and 4-5 of them devoted to absorbing at 719 nm[142]. Additionally, a loss of about four C719 chlorophylls upon monomerization of trimeric PSI was estimated in the same regard[143]. In another spectroscopic study of *T. elongatus* PSI, the ~50% quantum yield of P700 oxidation at low temperature demonstrated that red chlorophylls localize as a cluster in the periphery of PSI[51]. Even though the number of lost chlorophylls has always been an estimation, interestingly, it has been reported that irrespective of the method used, monomerized PSI always exhibited the loss of 'red' chlorophylls[38,143]. The rationale behind the monomerization induced susceptibility of the membrane-exposed surface region of *T. elongatus* PSI to loose 'red' chlorophylls is still obscure. Related literature exhibits a vast amount of proposals regarding the molecular identity of 'red' chlorophylls. These proposals are established by experimental work as well as

theoretical work and all were predicated on chlorophyll-chlorophyll relative distances, alignment of Q_Y (referring to the longer wavelength absorption band of chlorophylls and the molecular orbital states causing this absorption) to the membrane plane, the possible excitonic coupling of their chlorine rings, and site energies[28,56,58,144,145,146,147,148,149,150,151,152,153]. The straightforward relation of monomers lacking PsaL subunit (ΔPsaL mutants) and diminish of the C719 in these monomers focused the search in trimerization domain and upon calculations, B1237/B1238 and A1132/B1207 dimers were found to be suitable candidates[144,145,146,148,151,152]. Along a similar line of arguments, it was proposed that since the disruption of the trimer causes their loss, 'red' chlorophylls should be located at the monomer-monomer interface[28]. Based on the idea that funneling of excitation energy to the reaction center is aided by close localization of 'red' chlorophylls and that quenching of $P700^+$ necessitates a limited distance, vicinity of 'red' chlorophylls to P700 had been suggested[154,155]. Despite the efforts to identify the number and location of red chlorophylls, the findings are still not conclusive.

As a result of their lower energy absorption, red chlorophylls change the excited energy transfer dynamics amongst the light harvesting antenna. It is suggested that they act as energy traps, slowing – or maybe controlling- the speed of excited energy transfer to P700[156]. The electron transfer system is defined as a system of two quasi-symmetrical branches by Nelson and Yocum[157], and in the same paper it was stated that this two branched design had been invoking questions about the reasoning behind. The measurements of the branch activities using point mutations provided information about different branch activities in different species. It is shown that cyanobacterial PSI shows differences in the branch activities. Hereafter, the branches will be referred as Branch A and Branch B following their predominant coordinations by subunits PsaA and PsaB. Branch A has been shown to be more active in Cyanobacteria[158,159,160]. These studies conclude that there is a difference in the active use of branches which changes as the evolutionary level of the organism changes. While in cyanobacteria, PsaA side of the branch was reported to be more active, this relative activity changes into a equivalent activity in more comlex organisms[180].

5.2 Materials and Methods

In order to identify the structural differences between the monomeric PSI and other oligomers to associate the differences to functional data, monomeric structure is superposed with the trimeric crystal structure of PDB ID: 1JB0 at the secondary structure level, using the Superpose software in CCP4[138] software package.

The structures used in this part of the work are;

- PDB id :1JB0[28],
- PDB id: 6HQ1[39],
- PDB id: 5OY0[41],
- PDB id: 6LU1,
- PDB id: 7WB2.

In the superposition process, trimeric model of 1JB0 was kept fixed and monomeric model 6LU1 was anchored on the fixed model using the common sequence both structures at the core polypeptides PsaA and PsaB. For a second level of comparison on the same grounds, the same procedure was followed for 6HQ1 (monomeric) and 5OY0 (trimeric) model of *Synechocystis* PSI. The visualization was done using ChimeraX[107].

5.3 Results

5.3.1 Oligomerization and the Inner Peripheral Region

The two models built by cryo-EM (6LU1) and X-ray diffraction complement each other. The peripheral subunits that are interpreted as flexible in the solution state are well defined and clearly visible in the crystal structure, allowing the interpretation that the protein is intact. Results of the biochemical and biophysical experiments strengthen this observation. However, the C-terminal helix of PsaL could not be modeled in either of the structures, as visualised in Figure 5-1 (a, b).

Figure 5-1.(b) shows a similar comparison that was available by the release of the trimeric[41] and monomeric[39] PSI structures from *Synechocystis sp*. It is very significant that in all 3 monomeric structures released until today, PsaL subunit is very well defined and not flexible at the α-helical level except the C-terminal. Despite the prominent role of PsaL in oligomerization, only ramifications of three

distinct monomerization modi operandi are localized to the C-terminal region. There is also evidence that in tetrameric structures[46,47] and even in IsaA supercoplexes[162,163] the C-terminal region of PsaL exhibits divergences just as the cofactor content does. One other common denominator for the two cases is the absence PsaL bound caretonoid BC-L22, which has already been suggested to have a structural role in oligomerization. Other variations are not explicitly common for the two monomerization cases, since all three PsaL-bound chlorophylls could be modeled in the monomer model of *T. elongatus*, whereas they are missing in the monomer model of *Synechocystis* sp. These findings strongly suggest that monomerization does neither result in the overall flexibility of PsaL nor the loss of PsaL-bound chlorophylls.

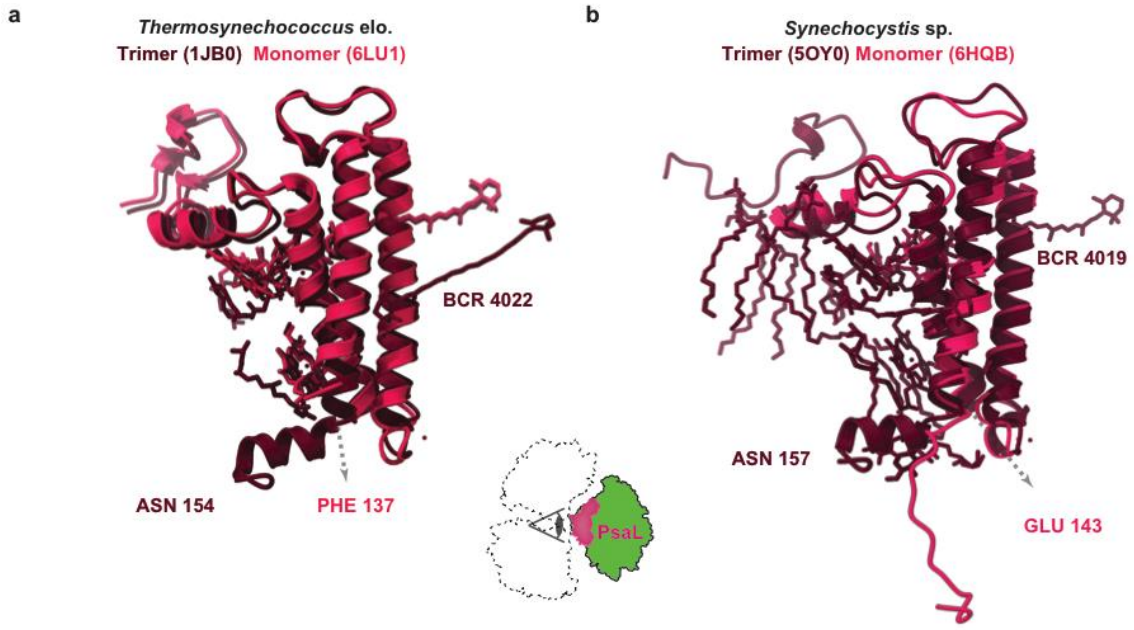

Figure 5-1 PsaL Subunit as Viewed From The Center of The PSI trimer. a) *T. elongatus* trimer and monomer superposed for illustration of the absence of the C-terminal α-helix and the PsaL bound carotenoid BCR-4022. The C-terminal phenylalanine in our monomer model of PsaL is indicated with a dashed arrow. b) *Synechocystis* sp. trimer and monomer superposed with the C-terminal glutamate of the monomer model of PsaL indicated by a dashed arrow.

5.3.2 Carotenoid Network

Carotenoids form the second most crowded group amongst cofactors in *T. elongatus* PSI. 22 caretonoids comprising six groups were identified in trimeric structure for each monomer whereas 26 carotenoids are modelled in my Cryo-EM structure with PDB ID 6LU1. In order to understand the differences in the

carotenoid content, carotenoid networks of two structures are superposed in Figure 5-2.

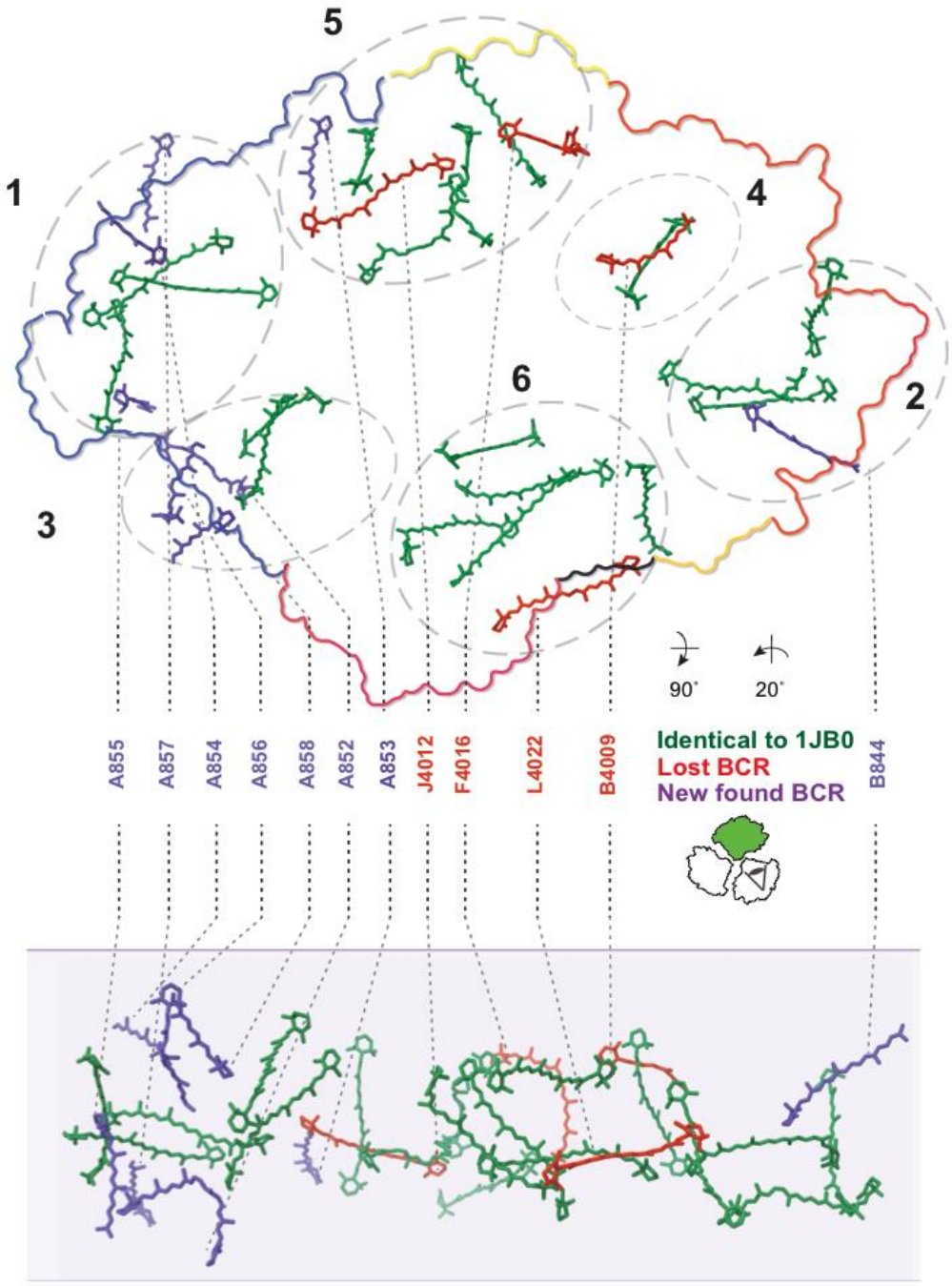

Figure 5-2 Carotenoid Network. View along the membrane normal from the stromal side (upper panel) with monomer outlined according to subunit color. Lower panel: side view along the membrane plane with the membrane indicated in shade. Carotenoids found in both monomer and trimer structures are colored in green, carotenoids not found in the monomer structure are colored in red and newly found ones are colored in blue. Carotenoids are clustered according to ref[28] and indicated by dashed circles and their respective number.

Amongst the 26 carotenoids in the structure of 6LU1, 8 were unprecedented, however four caretonoids modelled in the structure of 1JB0 could not be modelled. There is a controversy between the spectroscopic analysis of PSI monomer which indicates a decrease in carotenoids absorption upon monomerization and the structural data showing a higher total number of carotenoids. The superposition revealed that 18 of the modelled caretonoids in the monomeric structure are observed to localize accordingly with their counterpart in the trimer structure. Lost carotenoids were BC-F4016 (a 13'-cis isomer) and BC-J4012 from the periphery of the trimer, BC-B4009 in the vicinity of the periphery and BC-L4022 from the trimerization interface. The majority of the novel carotenoids (BC-A853, BC-A854, BC-A855, BC-A856, BC-A857, and BC-A858) were found in the perimeter of PsaA, and only one new carotenoid (BC-B844) was found in PsaB (Figure 5-2). Of the eight novel carotenes, half can be assigned to the lumenal side and half to the stromal side. All newly found carotenoids are located close to chlorophyll chlorine rings within a distance range of 3.5 - 5.1 Å. BC-A852 was fully modeled as a 13'-cis isomer and BC-A856 was modeled as a 9'-cis isomer. Interestingly, out of these two carotenoids, the head group of BC-A852 is located in the same region occupied by the lost chlorophyll aC-K1401 of the trimer crystal structure and BC-A856 is in proximity to same lost chlorophyll. Jordan *et al*. grouped the carotenoids into six distinct clusters. The most noticeable change in the monomeric model regarding these clusters is that the disturbance in the population balance between the clusters 3/4 and the clusters 1/2.

5.3.3 Chlorophyll Network

Chlorophylls form the most crowded group of *T. elongatus* PSI cofactors. 96 chlorophylls were identified in the trimeric structure for each monomer and 82 are modelled in my 6LU1 structure. In order to understand the differences in chlorophyll content, chlorophyll networks of two structures are superposed in Figure 5-3.

82 chlorophylls reticulating within the PSI monomer are observed to overlap with their counterpart in the trimer crystal structure, leaving 14 chlorophylls of the peripheral antenna absent in the monomer structure. Among these aC-A1402, aC-K1401, aC-J1302, aC-J1303, aC-F1301, aC-X1701, and aC-B1233 are

located on the lumenal side of the peripheral antenna network and the remaining chlorophylls are all located on the stromal side of the peripheral network.

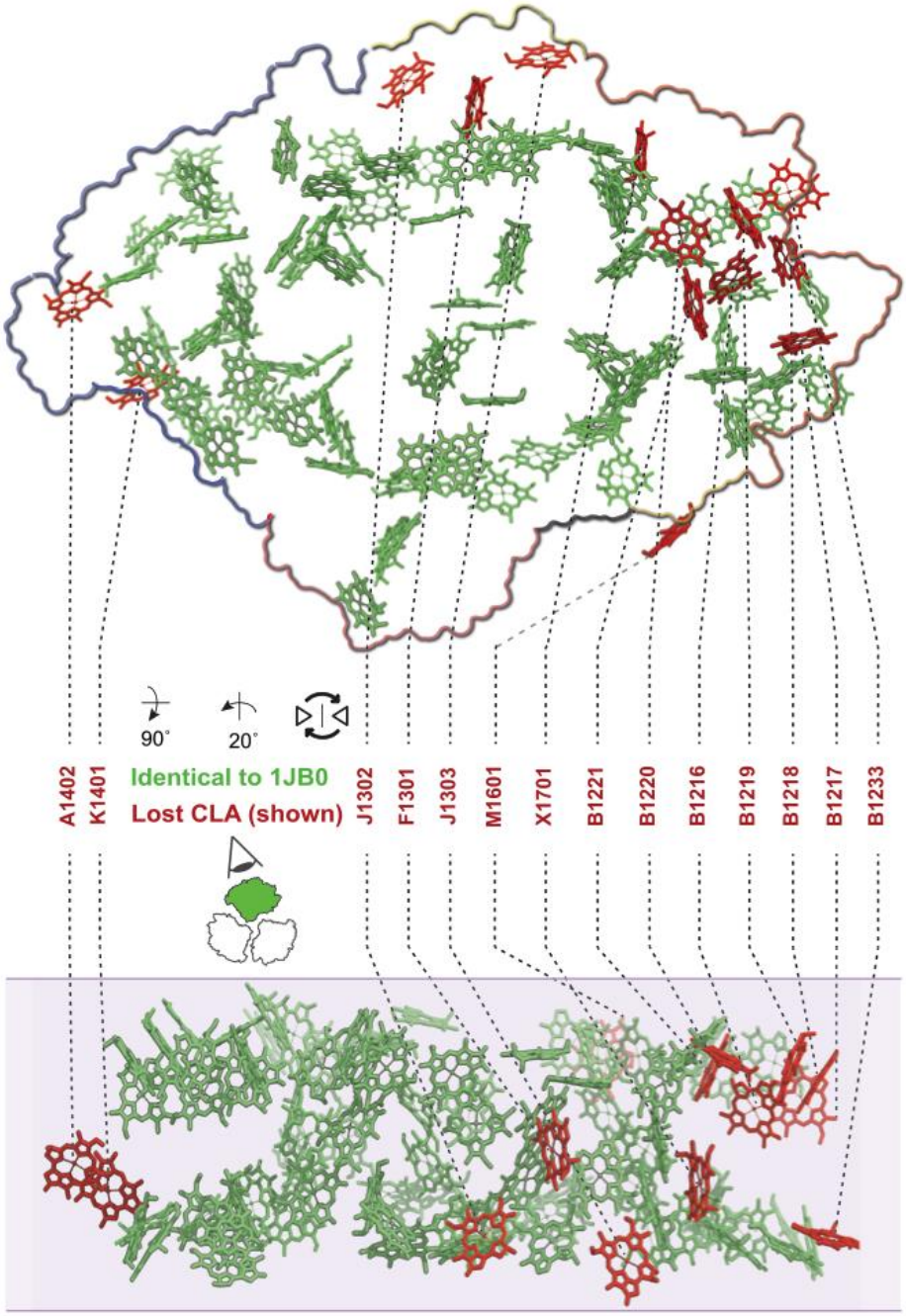

Figure 5-3 Chlorophyll Network. View along the membrane normal from the stromal side (upper panel) with monomer outlined according to subunit color (upper panel). Lower panel: side view along the membrane plane with the membrane indicated in shade. Chlorophylls found in both monomer and trimer structures are colored in green, chlorophylls not found in the monomer structure are colored in red.

Seven of the lost chlorophylls are localized in PsaB, and the remaining seven are distributed to PsaA, PsaF, PsaK, PsaM and PsaX, one per subunit. The only loss of chlorophylls from the trimerization interface are from PsaM (aC-M1601) and PsaK (aC-K1401). PsaL, the subunit with the most prominent role in trimerization is observed to maintain all its chlorophyll molecules in the same positions. All other 12 lost chlorophylls are at the exterior membrane-facing side of the PSI trimer and thus accessible by the surrounding thylakoid lipid bilayer. Among the 14 lost chlorophylls, only a group of six chlorophylls on the stromal side of PsaB, aC-B1216-B1221, are in contact with each other and form a tight cluster. The location of this chlorophyll cluster coincides with the only flexible part of the monomeric PsaA/PsaB core that could not be modeled, the stromal side loop-helix-loop motif at PsaB 291-316. This region is shown in Figure 5-4 with a closer look. The disordered region around the hexametic cluster exhibits unique structural relations in the trimeric model. Two phenylalanine residues (B309 and B310) of the short horizontal α-helix protrude from atop as a loose clamp bracing the chlorine ring coordinating phytol chain of the membrane-facing chlorophyll B1219 (Figure 5-4 inset 1). This hexameric cluster of chlorophylls is located above the characteristic chlorophyll trimer of PsaB that resembles a staircase. The outer 'step' of the staircase chlorophylls, aC-B1233, is also absent from the model (Figure 5-4 inset 3). Three of the chlorine rings in the hexameric cluster and two of the 'staircase trimer' are conspicuously coordinated by water. Lipid IV, (the only lost lipid in the monomer), is in bridging the hexameric cluster to the X8-Try residue of the PsaX.

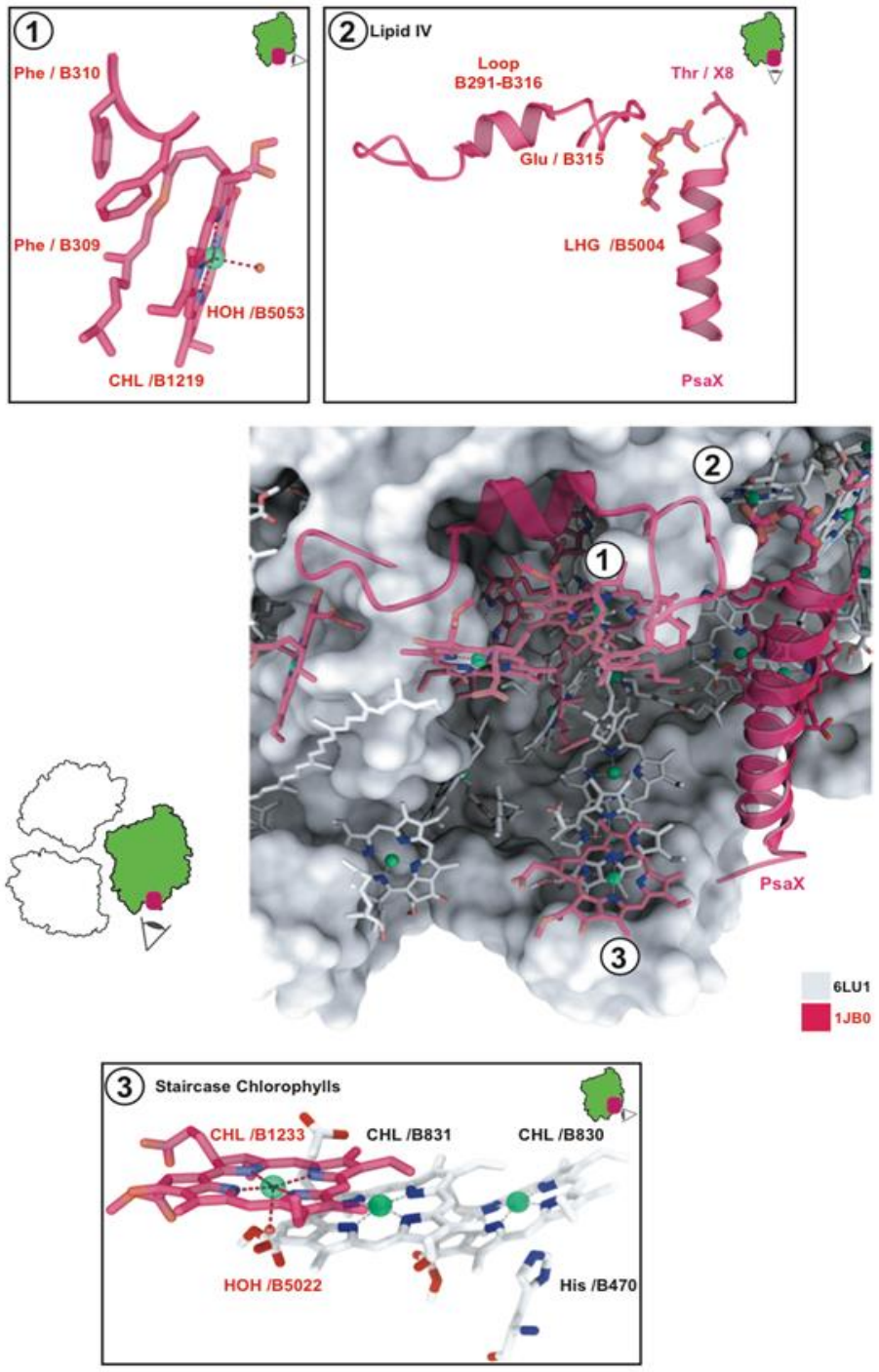

Figure 5-4 The Main Region of Disorder in Monomerized PSI and The Putative Site of Lost 'Red' Chlorophylls. The monomer model 6LU1 is depicted in grey as surface for protein and as ball and stick for ligands. Ligands and protein regions of the trimer structure model 1JB0 that could not be modeled in our monomer structure in red ribbon or ball and stick. ① Weak coordination of the lost chlorophyll B1219 of the trimer structure. ② Interaction of the lost lipid IV of the trimer structure with the in the monomer structure disordered loop-helix-loop motif of PsaB 291-316 and the lost PsaX subunit. ③ Weak coordination of the lost chlorophyll B1233 of the lumenal side trimer staircase chlorophylls.

Barring the flexibility in the PsaL C-terminus and the disorder in the hexameric cluster region, the most striking structural change revealed by the superposition is localized to the PsaK region of trimer. The new carotenoid BC-A855 is located in the middle of two lost chlorophylls, aC-A1402 and aC-K1401 (Figure 5-5).

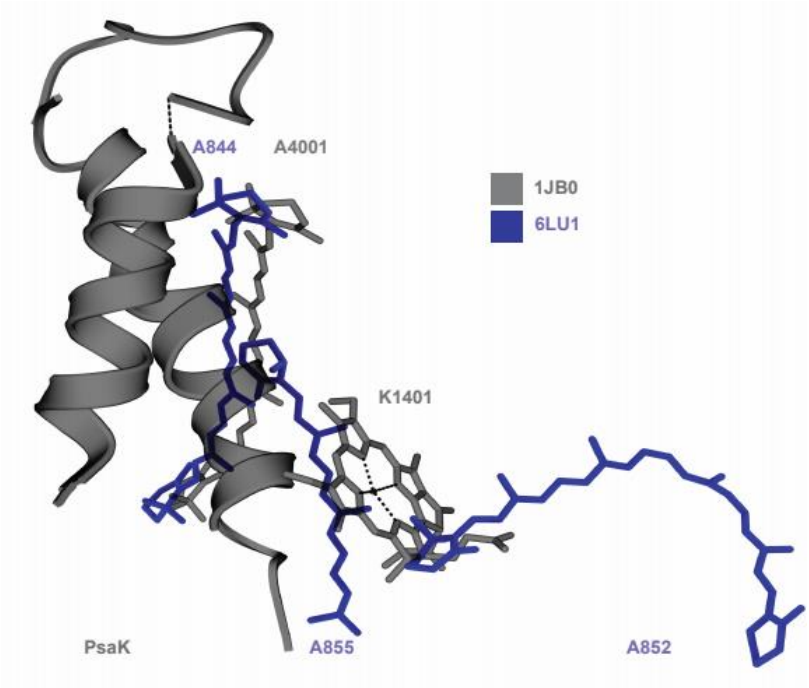

Figure 5-5 Mobility of Carotenoids Upon Monomerization. In the PSI monomer structure (PDB ID 6LU1) newly found carotenoids A855 and A852 are clashing with the position of PsaK and its chlorophyll in the trimer structure. Likewise, PsaK bound carotenoid A4001, named A844 in the monomer structure, of the trimer structure shifts its position to a degree that its clashes with the space occupied by PsaK in the trimer structure.

It is also notable that among the lost pigments,

- BC-L4022/aC-M1601
- BC-F4016/aC-X01
- BC-B4009/aC-B1220

were found in close range, lost as chlorophyll-carotenoid couples.

5.4 Discussion

In this dissertation, the structure of PSI from the thermophilic cyanobacterium *Thermosynechococcus elongatus*, monomerized by LDAO and ammonium sulfate treatment was determined and analysed. High yield PSI monomer extraction was achieved. The purification prodecure is explained in Chapter II together with the characterization by biochemical and biophysical means. X-ray crystallography and cryo electron microscopy experiments are described in Chapter III and Chapter IV, respectively. Cumulative interpretation of the experiments demonstrates that the investigated proteins are active, monodisperse and intact, ensuring the genuinity of monomeric PSI. The spectral analysis of the monomeric proteins in comparison with their trimeric counterpart exhibited a decrease absorption at 720 nm and a blue shift in the fluorescence spectrum of monomeric PSI relative to that of trimeric PSI. Given that a number of light absorbing entities were not possible to model, these findings establish a framework for the assessment of red chlorophylls identity, behaviour and effect on energy/charge transfer

A careful examination of 3.2 Å single particle cryo-EM monomer structure in comparison to the 2.5 Å X-ray structure of trimeric PSI revealed that;

- PsaK and PsaX had a flexibility in the solution state that prevented the modelling of their residues
- PsaF and PsaJ had a flexibility in the solution state that curbed the modelling and constrained the reconstruction of their aminoacid residues to about a fifth of their counterparts in the trimeric crystal structure
- PsaL subunit had a flexibility localized only to the terminal helix of the subunit

Considering the solubilization and monomerization process, this flexibility may be explained with the fact that these peripheral subunits are exposed to the chemical treatment for a relatively longer time period compared to other subunits. Their biochemically/biophysically proven presence and observability in the crystal structure demonstrates a reversible instability in the solution state. However, the terminal helix of PsaL is observable neither in the cryo-EM structure nor in crystal structure. This contradiction clearly shows that, this helix is not ordered even in the crystalline state once the the trimer is seperated into monomers. As the

MALDI-ToF analyses demonstrate the entirety of PsaL to be present, in contrast to other flexible parts, the instability of in this region may be explained by an irreversible disorder in the secondary structure. This short α-helix, placed on the lumenal side and oriented roughly parallel to the membrane plane in oligomeric PSI has been reported to have a role of making contacts between the monomers in the oligomerization process[28,41,44,45,46]. The monomerization induced disorder in this helix may acknowledge its stabilization by the formation of contacts with its equivalents in different monomers and transformation to an α-helical secondary structure only upon oligomerization. It is possible to speculate a role to Ca^{2+} chelation considering the trimeric structures, but 3.2 Å resolution does not provide information about the Ca^{+2} ion or its state. The caretonoid L4022 may also have a role in the oligomerization, considering that it is not modelled in neither of the *Synechocysts sp.* and *T.elongatus* monomers (Figure 5-3). On the other hand, it is noteworthy to mention that all three chlorophyll molecules and one of the two caretonoid molecules were succesfully modelled to the structure with the current data.

Despite the lower resolution of my cryo-EM 6LU1 model, more caretonoids were observed in the structure compared to the published trimeric X-ray model of 1JB0, as observable in Figure 5-4. Taking the mobile nature of the carotenoids and their localization in the luminal or stromal sides in contrast to the localization of 1JB0 carotenoids vertical to the membrane plane into account, it is possible to presume a non-natural attachment to PSI after the solubilization. Moreover, considering the reliance of the HIC seperation on hydrophobicity, highly hydrophobic nature of carotenoids provides a possibility of distrubution of extracted idle proteins into fractions. The possible presence of free carotenoids in micelles within the bulk protein solution could be reflected in spectroscopic data, and additionally it could result in aberrant attachment of caretonoids to PSI. However, additional spectroscopic experiments revealed that the removal of free detergent micelles did not result in any changes in the difference of chlorophyll absorption or carotenoid absorption. A more detailed look into the positions of caretonoid molecules in Figure 5-4 reveals that;

- Caretonoid L-4022 of 1JB0 is lost

- The newly found carotenoid A855 is anchored in a location that is occupied by PsaK in the trimer crystal structure
- The newly found carotenoid A852 is partially in the same location as the PsaK bound chlorophyll of the trimer crystal structure.
- Caretenoid A844 (conserved and retained carotenoid in monomeric structure) shifted towards PsaK

Considering the reported minuteness of excitation transfer between monomers of the PSI trimer[176] and loss of the same caretonoid from both monomeric structures[39], BCR-L4022 may possess a rather structural role in oligomerization than an energetic role. Spatial differences observed between the PSI-bound carotenoids of monomeric and trimeric structures demonstrates that, compared to other cofactors in the structure, carotenoids appear to experience a relatively larger degree of portability. The asymmetrical distribution of caretonoids in the trimeric crystal structure of *Synechocystis sp.* might also support this observation[15]. Regarding the carotenoid content, it is also noteworthy that BC-A853, had also been modelled in the very recently reported single particle cryo-EM structure of the *T. elongatus* PSI trimer[181]. Its presence in both recent PSI structures but not in 1JB0 could be related to differences in sample preperation. However, the calculated Q scores of caretonoid molecules modelled in the monomeric structure remarks that, resolvability of newly modelled caretonoids are lower than the preserved ones. The spectral data showing more caretonoid absorption in trimer compared to monomer remarks the possibility that, there may be more caretonoids yet to be modelled in the trimeric structure, owing to their flexibility and maybe mobility.

The most peculiar difference between the trimeric and monomeric structures is the chlorophyll content. Of the 96 chlorophylls present in the trimer crystal structure, 14 were not found in the monomer structure and thus, were either physically lost or too disordered to permit a well-defined density map to model them. In the light of the spectral differences between the monomeric and trimeric PSI (also observed for the current protein samples as shown in Figure 2-9), it is possible to associate the difference in the chlorophyll content to red chlorophylls. It has already been shown that, of the long wavelength absorption bands of trimeric PSI, C719 diminishes upon monomerization. It is estimated that this

difference stems from the loss of five chlorophylls lost per monomer[51]. The proposals for the identities of the red chlorophylls until today are all based on this difference between the spectra of monomeric and trimeric PSI and include many different approaches of spectroscopy and theoretical work. However due to lack of structural data of a monomeric structure, the common framework of all is the chlorophyll locations defined in the trimeric structure. This framework provided details about the relative distance between the chlorophylls, alignment of chlorophyll polarities to the membrane plane, the possible excitonic coupling of their chlorine rings, and site energies[28,56,58,144,145,146,147,148,149,150,151,152,153]. But as demonstrated in Table 5-1, there is no consensus even about the number of chlorophyll molecules causing an absorption band in the UV-Vis spectra of PSI. Moreover, despite all the efforts spent, it was not possible to define a pattern such as the ligation properties that gave rise to such an interaction. The only solid clue about the positioning of red chlorophylls came from a polarization dependent single molecule spectroscopy experiment in 2015[56], proposing that chlorophylls causing the 708 nm absorption band and 719 nm absortion bands should exhibit a perpendicular orientation to the membrane plane. Other approaches center the search of red chlorophylls on;

- Loss of chlorophylls from PsaL with regard to its expected destabilization due to its role on trimerization. This aproach resulted in suggestions such as B1237/B1238 and A1132/B1207[144,145,146,148,150,151]
- Loss of chlorophyll from trimerization region in relation to expected regional destabilization[28,164]
- Localization of red chlorophylls close to ETS for the functions of funneling excitation energy and possible necessity of short distance for funnelling[154,155]

Table 5.1 summarizes part of the related literature.

Table 5-1 A summary of suggested red chlorophyll identities in relevant literature

Year	Group	Suggested Identities
2001	Jordan *et al.*	B31-B32-B33 A38-A39 A32-B07 B37-B38
2001	Schlodder *et al*.	A16-A17-A25 A38-A39 B18-B19 B37-B38
2002	Damjanovic *et al.*	A31-A32-B07-B6 B24-B25 A26-A27
2002	Sener *et al*.	A32-B07 A33-A34 A24-A35 B22-B34
2002	Byrdin *et al*.	A31-A32-B07-B6 A38-A39 B37-B38
2003	Gobets *et al*.	B31-B32-B33 B31-B32-B33 A32-B07 A38-A39 B37-B38 A12-A14 A10-A18 B09-B17
2007	Schlodder *et al*.	A31-A32-B07 A16-A17-A25 B14-B15-B23 B31-B32-B33 B18-B19 B24-B25 B37-B38
2010	Shibata *et al*.	A38-A39 A32-B07 A33-A34 B24-B25 B26-B27
2015	Skandary *et al*.	B18-B19 B31-B32 B32-B33

For the first time, the monomeric structure of 6LU1 provides structural information about the lost chlorophylls, precisely defining their number, positions and identities. In contrast to the expectations of chlorophyll loss from PsaL and the

trimerization interface, most of the lost chlorophylls are unambiguously located in the distal region of the monomer that faces the membrane with the exception of M1601 and K1401. As portrayed in Figure 5-3, no chlorophylls are lost from the region in vicinity of ETC either. Moreover, the distances between lost chlorophylls of 6LU1 are larger than distances that allow the interactions that may induce a long wavelength absorption, except the hexameric cluster of chlorophyll molecules in PsaB. Aspects of this region may be described as;

- Being stationed at the stromal side of PsaB, about the border of the protein and secluded from ETC
- Being surrounded by a cavelike architecture in the rearward and being the uttermost prone region of PSI to membrane lipids (Even though there is a similar cavelike structure nearly symmetrical to this region shown in Figure 5-6., in the trimer it is not exposed to membrane as much since it is located in the monomer-monomer interface and PsaK blocks the region that is slightly outward.)
- Being situated as a hub between the only lost chlorophyll of the unique staircase chlorophylls[28], the only disordered PsaB secondary structure (loop-helix-loop motif, Psab291-316) and Psax
- Being bridged to PsaX by the only lost lipid of the structure

At the edge of the cluster, the lost chlorophyll B1219 is coordinated by only a water molecule on the protein side and its own phytol chain on the membrane side. Two phenylalanine side chains (PsaB309/310) of the disordered stromal side loop-helix-loop motif of PsaB (PsaB291-316) appear to seize B1219, maintaining its connection to protein. A dimer of B1219 with the neighbouring B1218 dimer has been represented as canditates in a few studies[56,151]. The seventh lost chlorophyll of PsaB, B1233, is the outermost, membrane-facing 'stair' of the 'staircase' chlorophyll trimer, neighbouring PsaX on the lumenal side. The trimer of chlorophylls formed by B1231, B1232 and B1233 has been suggested as candidate red chlorophylls for several times owing to their parallel arrengement, site energy and excitonic coupling[28,56,146,148,151]. As featured in Figure 5-3 and 5-4, B1216 together with B1219 and B1233 institute the junction of lipid bilayer and the protein. Astoundingly, coordination of the chlorine rings by either their own phythol chains or water molecules in the trimeric structure is

common for these three chlorophylls. It is also notable that in the model of trimeric PSI from the mesophilic cyanobacterium *Synechocystis* sp*.* which lacks a C719 absorption band, no chlorophyll corresponding to B1233 was found[39,41].

In regard to this difference, the region of lost chlorophylls adjacent to PsaX from *T. elongatus* with the same region of the PSI complex of *Synechocystis* sp*.* in both trimer and monomer structures was superposed and compared in Figure 5-6, 7. Important differences are the absence of PsaX, the absence of B1233 with its supporting loop region of B490-496 of *Syncechocystis* PSI[41]. Interestingly, these differences had been noticed even before the release of the first *Synechocystis* crystal structure[184]. Moreover, the loop formed by the residues B306-316 of the loop-helix-loop region B291-316, that with its two coordinating phenylalanine side chains stabilizes the very weakly bound B1219 in *T. elongatus* PSI trimer structure which is disordered in our monomer structure, is also missing in *Synechocystis* sp*.* PSI. Instead *Synechocystis* sp*.* PSI has an additional third chlorophyll which, if present in PSI of *T. elongatus*, would clash with PsaX.

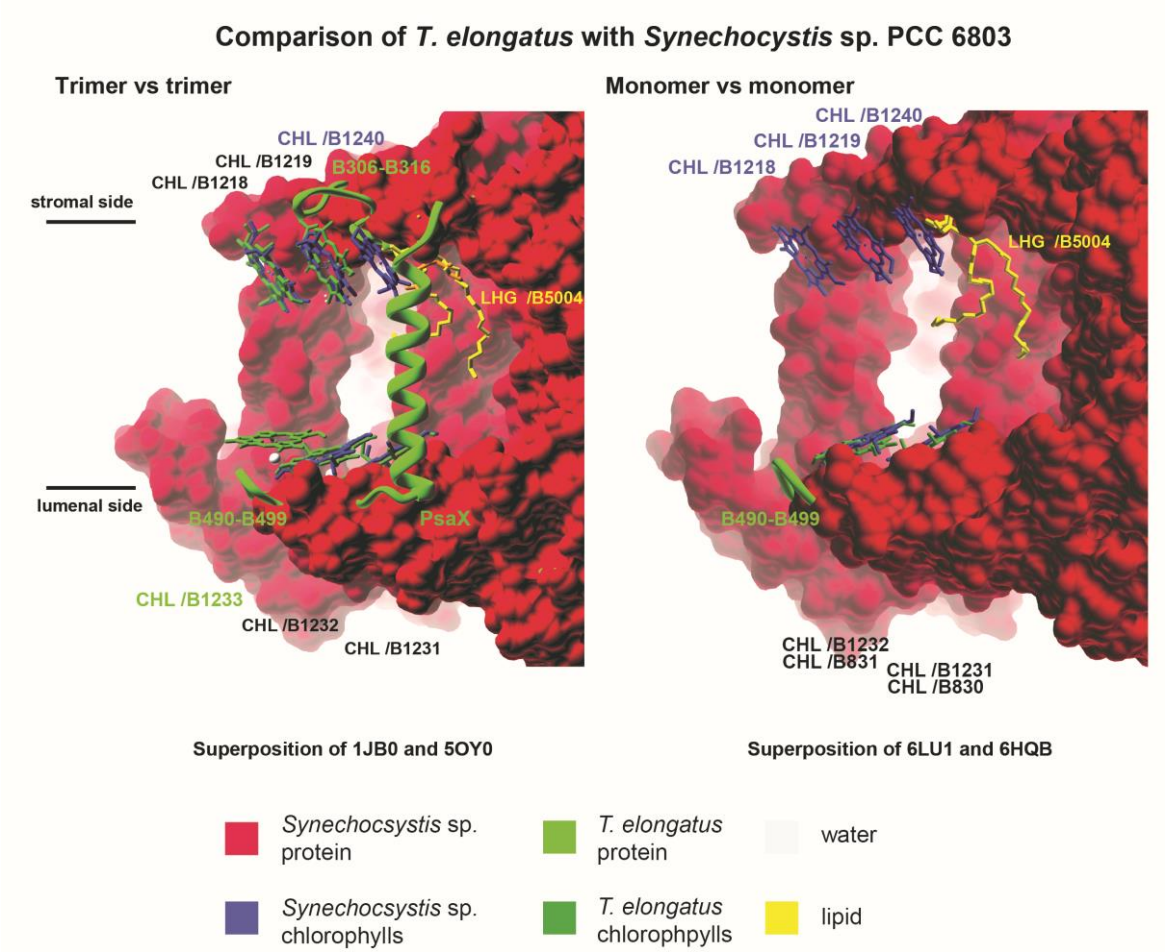

Structural differences between PSI from *T. elongatus* and *Synechocystis* sp. at the 'red' chlorophyll cluster region	
Between trimer structures	*Between monomer structures*
Stromal loop (B306-B316) above B1219 in *T. elongatus*	Disorder of B1218 and 1219 amongst other chlorophylls in *T. elongatus*
Chlorophyll B1233 to form a trimer with B1232 and B1231 in *T. elongatus*	Absence of B1240 in *T. elongatus*
Lumenal loop (B490-B499) below B1233 in *T. elongatus*	Presence of lipid B5004 in *Synechocystis* sp.
Chlorophyll B1240 forming a trimer with B1218 and B1219 in *Synechocystis* sp.	Absence of a loop (B490-B499) in *Synechocystis* sp.

Figure 5-6 Superposition of Chlorophyll Hexamer Region of PSI Monomer and Trimer of *T.elongatus* and *Synechocystis* sp. Following is a list of the differences between trimeric and monomeric PSI from corresponding species.

Significant structural differences of *T. elongatus* PSI with *Synechocystis sp.* PSI are concentrated in the main region of disorder in monomerized *T. elongatus* PSI.

And the most significant spectroscopic difference between the two species is the absence of C719 chlorophylls in *Synechocystis* PSI. This provides strong support for the assignment of B1233 and B1219 as C719 'red' chlorophylls. For strong red shifts in chlorophylls excitonic coupling alone is thought to be insufficient and the importance of magnesium coordination by water has been suggested as a factor allowing stronger red shifts[184,185]. We find that the absence of the water coordinated 'outer staircase' chlorophyll B1233 and the replacement of water coordination by histidine coordination in B1219 of *Synechocystis* PSI is in support of this notion. These differences are also used in a recent study to produce a red shift in the *Synechocystis* sp. by the addition of the same loop to PSI trimer[186]. It was observed upon this addition, a new chlorophyll was attached to the same place and proteins red absorption showed a significant difference, in support of hereby explained hypothesis. These finding also show the importance of B490-496 loop for accomodation of the chlorophyll, providing clues about the evolution of PSI amongst different species.

The conjoint unique ligation, loose coordinations and juxtaposition to lipid membrane brings B1216, B1219 and B1233 to forefront as possible candidates for red chlorophylls. Their proximity with a group of lost clorophylls within a cluster is also in line with this nomination.

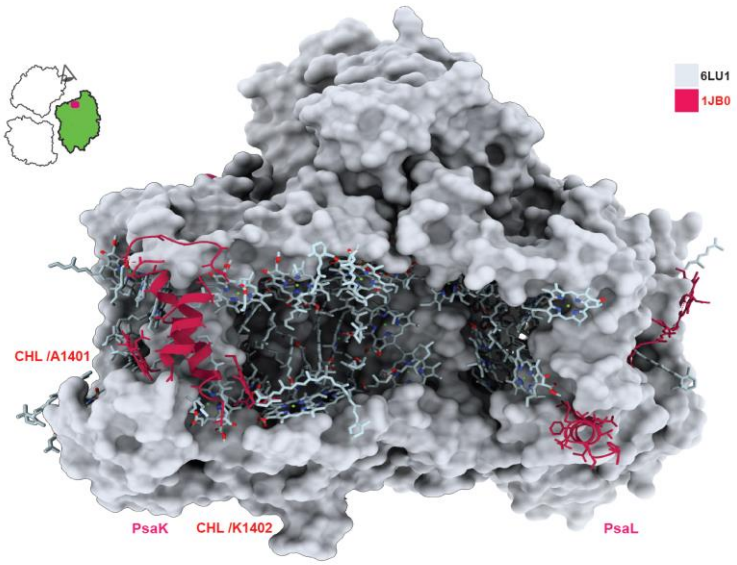

Figure 5-7 The Cavelike Region Symmetric to The Region of Hexameric Chlorophyll Cluster. The monomer model 6LU1 is depicted in grey as surface for protein and as ball and stick for ligands. Ligands and protein regions of the

trimer structure model 1JB0 that could not be modeled in our monomer structure in red ribbon or ball and stick.

Au-fait with favoured notion of clustered localization of red chlorophylls[51], mergering the supporting theoretical and spectroscopic studies with the currently represented structural data narrates a localization of the red chlorophylls in the lost chlorophyll cluster, are the disordered region of PsaB which is surrounded by Lipid IV, PsaX and loop-helix-loop motif between the residues B291-B316. This hypothesis contours an interaction of vibrational energy transfer from the lipids of thylakoid membrane to the chlorophylls accomodated in region as a possible tuning mechanism for long wavelength absorption. This effect has never been involved in the related calculations on the red chlorophylls as far as inferred from the literature survey in this dissertation.

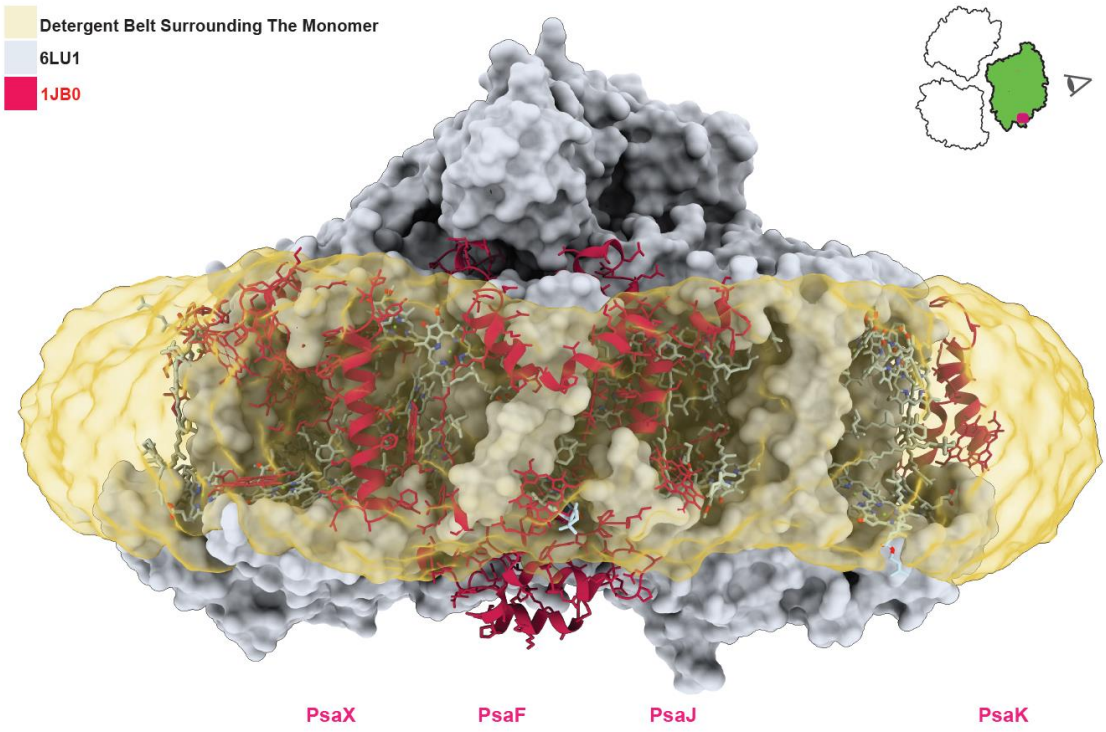

Figure 5-8 The Detergent Belt Surrounding The PSI Monomer After Solubilization. The monomer model 6LU1 is depicted in grey as surface for protein and as ball and stick for ligands. The detergent belt is colored in pale yellow. The point of view is chosen to visualize all the disordered regions in the membrane facing region of a monomer.Ligands and protein regions of the trimer structure model 1JB0 that could not be modeled in our monomer structure in red ribbon or ball and stick.

It is possible to postulate a scenerio of the disassembling/disordering mechanism in regard to the spatial relations of the unmodelled components in this region. In the context of the solubilization mechanism wherein the detergents replace the lipids of the membrane, the removal of Lipid IV through interaction with a detergent molecule is plausible. Absence of Lipid IV may induce a disorder in PsaX, destabilizing the close neighbouring PsaF subunit partially on one side (as shown in Figure 5-8.) and loop-helix-loop motif of PsaB on the other side, eventually facilitating the derangement of the cluster altogether. This framework pleads for a function of PsaX in the stabilization and preservation of red chlorophylls boxed in the protein, whose function was not clear until today, may be speculated as an outcome of this scenario. On the other hand, monomerization-oligomerization has been reported as a reversible process in the presence of lipids[92,93]. Given the chance that proposed red chlorophyll region is rather disordered, but not detached from the structure, this information pinpoints an oligomerization induced conformational disorder, functioning as a molecular switch for turning on and off red chlorophyll activity and thus being incorparated in cyanobacterial state transitions. With red chlorophylls being absent from the core, oligomerization of PSI in algae and plants as a molecular mechanism for controlling their activity becomes redundant.

Even though the red chloropylls control the traffic during the excitation energy transfer, since their localization is unknown, they were hardly associated with electron transfer. However, the branch activites in cyanobacterial PSI correlate with the current findings. The sparse usage of the B branch of the ETC induces an asymmetric utilization of branch activities and this branch is enrooted in the same side of PSI as the supposed red chlorophylls. The trapped energy by the red chlorophylls might be predominantly channeled to the B branch resulting in a less frequent use compared to the A branch. This gambit also explains the inclination towards the bidirectional use of the branches in higher photosynthesis organisms that evolved to remove the red chlorophylls from the core to the light harvesting complexes surrounding the core.

CHAPTER VI.

CONCLUDING REMARKS

6 SUMMARY AND CONCLUSIONS

The outcomes of this research may be concluded as;

- Purification of PSI monomers with Protocol I using heat treatment in high salt conditions and β-DDM solubilization to yield in monomeric PSI crystals
- Purification of PSI monomers with Protocol II using LDAO solubilization and room temprature high salt treatment yielding monomeric PSI crystals
- Characterization of the proteins by biochemical and biophysical methodologies exhibiting the purity, heterogeneity and intactness of PSI monomers in the resulting samples, additionally providing spectroscopic data to support the structural analysis
- Structural analysis of crystals of PSI monomer purified by Protocol I by X-ray diffraction, yielding in a 6.5 Å resolution model deposited to the PDB with the accession code 7WB2
- Structural analysis of PSI monomer purified by Protocol II in solution state by cryo electron microscopy, yielding in a 3.2 Å resolution model deposited to PDB with the accession code 6LU1 and EMDB with accession code EMD-0977. Raw cryo-EM images of the T. elongatus PSI monomer after motion correction were deposited in the Electron Microscopy Public Image Archive (EMPIAR), under the accession number EMPIAR-10352 as the first cryoARM200 membrane protein entry.

The structural information produced by the interpretation of models may be listed as;

- The solution state flexibility of the subunits of PSI induced by monomerization of a trimer was revealed and reported;
  - PsaX and PsaK subunits were found to be fully disordered,
  - PsaF, PsaJ and PsaL subunits were found to be partially disordered,
  - A loop-helix-loop motif between the residues 291-316 of PsaB was found to be disordered.
- The disorder/losses in pigment content induced by monomerization was revealed and reported;
  - 14 of the chlorophyll molecules were found to be lost or disordered,
  - 4 of the carotenoid molecules were found to be lost or disordered,

- 8 new carotenoid molecules were found to be integrated to PSI monomer,

- The situation of 1 Ca^{+2} ion and 205 of the water molecules was not possible to discuss due to resolution restriction.

The findings were related to literature to produce hypothesis and discuss some of the concurrently unanswered questions. These may be listed as:

- Oligomerization mechanism is related to the findings about the flexible region of PsaL in comparison to other structures. A possible mechanism has been suggested.
- The changes in carotenoid content has been shown in comparison with the trimeric PSI structure and the possible mobility of these molecules within PSI is suggested.
- The changes in chlorophyll content has been shown in comparison with the trimeric PSI structure. These differences are related to literature about the light absorption behaviour of PSI monomers and trimers, and supported by the spectral measurements in this study to reveal the identities of red chlorophylls. A hexamer of lost chlorophylls is suggested as the red chlorophyll pool.
- Based on the localization of suggested red chlorophylls, possible function of the adjecent subunit PsaX, Lipid IV and loop-helix-loop motif of PsaB in maintaining the red chlorophyll molecules within the PSI has been discussed and suggested.
- The possibility of the unmodelled parts of PSI being disordered instead of being detached from the structure was related to reported “monomerization-trimerization” experiments, and monomerization was hypothesized as physological mechanism organizing the red chlorophyll usage in different light conditions.
- A relation between the red chlorophylls and branch activities of ETC has been hypothesized in regard to localization of red chlorophylls. The effect of evolution is discussed with respect to literature regarding ETC and red chlorophylls.

- As a result of superposition with most recent *Synechocsytis sp.* structures, the role of loop B490-496 has been suggested as accomodating an additional chlorophyll that contributes to the red absorptions of PSI.

On the foundation of the listed articles, the function of PsaX and lipid IV together with PsaB291-316 is proposed as stabilizing the spatial arrangement of the 'red' chlorophylls while allowing the mechanical vibration necessary for efficient reception of thermal energy. This proposition is regarded credible with respect to bioenergetics literature, as the water molecules, defined as the most common energizer of Brownian machines[165], are not available for the hydrophobic chlorophylls, and lipids are an established source of thermal energy for membrane bound molecular machines[166]. A possible scenario for the observed loss of the 'red' chlorophylls upon monomerization is enunciated as an unraveling starting from the lipid IV upon interaction with detergents during solubilization, succeeded by the destabilization of PsaX and the stromal side loop-helix-loop motif of PsaB291-316 culminating in the disorder or even release of the seven chlorophylls into the bulk solution. The region with a cavelike surrounding architecture in the rear and a direct contact to membrane in the front, is identified as the main location of 'red' pool chlorophylls. With an emphasis on their unique geometries, B1233 on the lumenal side, B1216 in the center and B1219 on the stromal side, all protruding straight into the bulk lipid and bridging the cluster with the membrane lipids, these chlorophyll are contemplated as regulatory units of three modes of interaction with the membrane. Perhaps these three pigments in their common exposure to the rapid movement of lipid acyl chains but with divergent micro-architecture are ideally situated to receive and deliver the different modes of vibrational thermal energy provided by the lipid bath of the surrounding membrane.

In the light of these findings, observations about the methodologies regarding structural biology has been shared. These observations may be listed as;

- The necessity of employing individual strategies for individual data sets in cryo-em image processing and modelling
- The effect of the restraint files in the modelling and the accuracy, (with the supporting illustration of the level of the differences caused by restraint files by an experiment and comparison to the current PDB structures.)

- Complementary nature of X-ray Diffraction and cryo electon microscopy

In summary, comparison of the trimer crystal structure (PDB ID 1JB0) with monomer crystal structure (PDB ID 7WB2) and single particle cryo-EM monomer structure (6LU1) enabled an examination of the candidates for 'red' chlorophylls and to conclusively assign them in the structure. Based on this assignment and the position-specific derangement of the oligomeric integral membrane protein complex, a novel functional and structural role for PsaX in the stabilization of 'red' chlorophylls is proposed.

REFERENCES

[1] Shih PM. Photosynthesis and early Earth. Current Biology. **2015** Oct 5;25(19):R855-9

[2] Olson JM, Pierson BK. Photosynthesis 3.5 thousand million years ago. Photosynthesis Research. **1986** Jan 1;9(1-2):251-9.

[3] Farquhar J, Zerkle AL, Bekker A. Geological constraints on the origin of oxygenic photosynthesis. Photosynthesis research. **2011** Jan 1;107(1):11-36.

[4] Boardman NT. Comparative photosynthesis of sun and shade plants. Annual review of plant physiology. **1977** Jun;28(1):355-77.

[5] Sage RF. The evolution of C4 photosynthesis. New phytologist. **2004** Feb;161(2):341-70.

[6] Barber J. A mechanism for water splitting and oxygen production in photosynthesis. Nature Plants. **2017** Apr 3;3(4):1-5.

[7] Li Y, Chen M. Novel chlorophylls and new directions in photosynthesis research. Functional Plant Biology. **2015** Jun 2;42(6):493-501.

[8] Fleming GR, Scholes GD. Quantum mechanics for plants. Nature. **2004** Sep;431(7006):256-7

[9] Lloyd S. Quantum coherence in biological systems. InJournal of Physics-Conference Series **2011** Jul 20 (Vol. 302, No. 1, p. 012037).

[10] Barber J, Tran PD. From natural to artificial photosynthesis. Journal of The Royal Society Interface. **2013** Apr 6;10(81):20120984..

[11] Kim D, Sakimoto KK, Hong D, Yang P. Artificial photosynthesis for sustainable fuel and chemical production. Angewandte Chemie International Edition. **2015** Mar 9;54(11):3259-66..

[12] Kiang NY, Segura A, Tinetti G, Blankenship RE, Cohen M, Siefert J, Crisp D, Meadows VS. Spectral signatures of photosynthesis. II. Coevolution with other stars and the atmosphere on extrasolar worlds. Astrobiology. **2007** Feb 1;7(1):252-74.

[13] Vera JP, Möhlmann D, Butina F, Lorek A, Wernecke R, Ott S. Survival potential and photosynthetic activity of lichens under Mars-like conditions: a laboratory study. Astrobiology. **2010** Mar 1;10(2):215-27.

[14] Hohmann-Marriott, Martin F.; Blankenship, Robert E. Evolution of photosynthesis. Annual review of plant biology, **2011**, 62: 515-548.

[15] Raymond J, Segre D. **2006**. The effect of oxygen on biochemical networks and the evolution of complex life. Science 311:1764–67

[16] Walker, J. C. (1980). Atmospheric constraints on the evolution of metabolism. In Limits of Life (pp. 121-132). Springer, Dordrecht.

[17] Musazade, E., Voloshin, R., Brady, N., Mondal, J., Atashova, S., Zharmukhamedov, S. K., ... & Bruce, B. D. **2018**. Biohybrid solar cells: Fundamentals, progress, and challenges. Journal of Photochemistry and Photobiology C: Photochemistry Reviews, 35, 134-156.

[18] CARDONA, Tanai. Reconstructing the origin of oxygenic photosynthesis: do assembly and photoactivation recapitulate evolution?. Frontiers in plant science, 2016, 7: 257.

[19] Raven, J. A., & Allen, J. F. **2003**. Genomics and chloroplast evolution: what did cyanobacteria do for plants?. Genome biology, 4(3), 209.

[20] Schmitt, Franz-Josef & Maksimov, Eugene & Junghans, Cornelia & Weißenborn, Jörn & Hätti, Patrick & Paschenko, Vladimir & Allakhverdiev, Suleyman & Friedrich, Thomas. (**2013**). Structural Organization and Dynamic Processes in Protein Complexes Determined by Multiparameter Imaging.

[21] Nelson, N. & Junge, W. Structure and energy transfer in photosystems of oxygenic photosynthesis. Annual Review of Biochemistry 84:659-83 **(2015)**. doi:10.1146/annurev-biochem-092914-041942

[22] Andreasson, L. E. & Vanngard, T. Electron Transport in Photosystems I and II. Annu. Rev. Plant Physiol. Plant Mol. Biol. 39, 379-411 **(1988)**. doi:10.1146/annurev.pp.39.060188.002115.

[23] Blankenship, R. E. Early Evolution of Photosynthesis. Plant Physiol. 154, 434–438 **(2010)**

[24] Amunts, A. & Nelson, N. Plant photosystem I design in the light of evolution. Structure 17, 637–650 **(2009)**.

[25] Golbeck, J. H. Structure and Function of Photosystem I. Annu. Rev. Plant Physiol. Plant Mol. Biol. 43, 293–324 **(1992)**.

[26] Boekema, E. J. et al. Refined analysis of the trimeric structure of the isolated Photosystem I complex from the thermophilic cyanobacterium Synechococcus sp. BBA - Bioenerg. 974, 81–87 (1989)

[27] S. Jeon and P. V Braun, “Hydrothermal Synthesis of Er-Doped Luminescent TiO_2 Nanoparticles”, *Chem. Mater.*, no. 15, pp. 1256-1263, **2003**.

[28] Jordan, P. et al. Three-dimensional structure of cyanobaoterial photosystem I at 2.5 Å resolution. Nature 411, 909-917 **(2001)**. doi:10.1038/35082000

[29] Zhao, L. S. et al. Structural variability, coordination and adaptation of a native photosynthetic machinery. Nat. Plants 6:869-82 **(2020)**. doi:10.1038/s41477-020-0694-3.

[30] Şener, M. K. et al. Comparison of the light-harvesting networks of plant and cyanobacterial photosystem I. Biophys. J. 89, 1630–1642 **(2005)**.

[31] Xiong, J. & Bauer, C. E. Complex evolution of photosynthesis. Annual Review of Plant Biology 53, 503-521 **(2002)**. doi:10.1146/annurev.arplant.53.100301.135212.

[32] Nelson, N. & Ben-Shem, A. The structure of photosystem I and evolution of photosynthesis. BioEssays 27, 914–922 **(2005)**

[33] Brettel, K. **(1997)**. Electron transfer and arrangement of the redox cofactors in photosystem I. Biochimica et Biophysica Acta (BBA)-Bioenergetics, 1318(3), 322-373.

[34] Şener, M., Strümpfer, J., Hsin, J., Chandler, D., Scheuring, S., Hunter, C. N., & Schulten, K. **(2011)**. Förster energy transfer theory as reflected in the structures of photosynthetic light‐harvesting systems. ChemPhysChem, 12(3), 518-531.

[35] Fromme, P., Melkozernov, A., Jordan, P., & Krauss, N. **(2003)**. Structure and function of photosystem I: interaction with its soluble electron carriers and external antenna systems. FEBS letters, 555(1), 40-44.

[36] Croce, R., & van Amerongen, H. **(2013)**. Light-harvesting in photosystem I. Photosynthesis Research, 116(2-3), 153-166..

[37] Kennis, J. T., Gobets, B., van Stokkum, I. H., Dekker, J. P., van Grondelle, R., & Fleming, G. R. (2001). Light harvesting by chlorophylls and carotenoids in the photosystem I core complex of Synechococcus elongatus: a fluorescence upconversion study. The Journal of Physical Chemistry B, 105(19), 4485-4494.

[38] Pålsson, L. O., Flemming, C., Gobets, B., van Grondelle, R., Dekker, J. P., & Schlodder, E. **(1998)**. Energy transfer and charge separation in photosystem I: P700 oxidation upon selective excitation of the long-wavelength antenna chlorophylls of Synechococcus elongatus. Biophysical journal, 74(5), 2611-2622.

[39] Netzer-El, S. Y., Caspy, I. & Nelson, N. Crystal structure of photosystem i monomer from synechocystis PCC 6803. Front. Plant Sci. 9, **(2019)**

[40] Kubota-Kawai, H. et al. X-ray structure of an asymmetrical trimeric ferredoxin-photosystem i complex. Nat. Plants 4, 218–224 **(2018)**.

[41] Malavath, T., Caspy, I., Netzer-El, S. Y., Klaiman, D. & Nelson, N. Structure and function of wild-type and subunit-depleted photosystem I in Synechocystis. Biochim. Biophys. Acta - Bioenerg. 1859, 645–654 **(2018)**.

[42] Gisriel, C. et al. The structure of Photosystem I acclimated to far-red light illuminates an ecologically important acclimation process in photosynthesis. Sci. Adv. 6, eaay6415 **(2020)**

[43] Kato, K. et al. Structural basis for the adaptation and function of chlorophyll f in photosystem I. Nat. Commun. 10, 1-9 **(2020).** doi:10.1038/s41467-019-13898-5

[44] Zheng, L. et al. Structural and functional insights into the tetrameric photosystem I from heterocyst-forming cyanobacteria. Nat. Plants 14, 331-332 **(2019)**. doi:10.1038/s41477-019-0525-6.

[45] Chen, M. et al. Distinct structural modulation of photosystem I and lipid environment stabilizes its tetrameric assembly. Nat. Plants 6, 314–320 **(2020).**

[46] Kato, K. et al. Structure of a cyanobacterial photosystem I tetramer revealed by cryo-electron microscopy. Nat. Commun. 10, 1-9 **(2019)**. doi:10.1038/s41467-019-12942-8.

[47] Li, M., Semchonok, D. A., Boekema, E. J. & Brucea, B. D. Characterization and evolution of tetrameric Photosystem I from the thermophilic cyanobacterium Chroococcidiopsis sp TS-821. Plant Cell 26, 1230-1245 **(2014)**. doi:10.1105/tpc.113.120782

[48] Kühlbrandt, W. The resolution revolution. Science 343, 1443–1444 **(2014)**

[49] Herzik, M. A., Wu, M. & Lander, G. C. Achieving better-than-3-Å resolution by single-particle cryo-EM at 200 keV. Nat. Methods 14, 1075–1078 **(2017)**.

[50] Pålsson, L. O., Dekker, J. P., Schlodder, E., Monshouwer, R. & Van Grondelle, R. Polarized site-selective fluorescence spectroscopy of the long- wavelength emitting chlorophylls in isolated Photosystem I particles of Synechococcus elongatus. Photosynth. Res. 48, 239–246 **(1996)**.

[51] Pålsson, L. O. et al. Energy transfer and charge separation in photosystem I: P700 oxidation upon selective excitation of the long-wavelength antenna chlorophylls of Synechococcus elongatus. Biophys. J. 74, 2611–2622 **(1998)**.

[52] Karapetyan, N. V., Holzwarth, A. R. & Rögner, M. The photosystem I trimer of cyanobacteria: Molecular organization, excitation dynamics and physiological significance. FEBS Letters vol. 460 395–400 **(1999)**

[53] Rätsep, M., Johnson, T. W., Chitnis, P. R. & Small, G. J. The Red-Absorbing Chlorophyll a Antenna States of Photosystem I: A Hole-Burning Study of Synechocystis sp. PCC 6803 and Its Mutants. J. Phys. Chem. B 104, 836–847 **(2000)**

[54] Cometta, A. et al. Thermal behavior of long wavelength absorption transitions in Spirulina platensis photosystem I trimers. Biophys. J. 79, 3235–3243 **(2000)**

[55] Brecht, M., Radics, V., Nieder, J. B., Studier, H. & Bitt, R. Red antenna states of photosystem I from Synechocystis PCC 6803. Biochemistry 47, 5536–5543 **(2008)**

[56] Skandary, S., Konrad, A., Hussels, M., Meixner, A. J. & Brecht, M. Orientations between Red Antenna States of Photosystem I Monomers from Thermosynechococcus elongatus Revealed by Single-Molecule Spectroscopy. J. Phys. Chem. B 119, 13888–13896 **(2015)**

[57] Riley, K. J., Reinot, T., Jankowiak, R., Fromme, P. & Zazubovich, V. Red antenna states of photosystem i from cyanobacteria Synechocystis PCC 6803 and Thermosynechococcus elongatus: Single-complex spectroscopy and spectral hole-burning study. J. Phys. Chem. B 111, 286–292 **(2007)**.

[58] Vaitekonis, S., Trinkunas, G. & Valkunas, L. Red chlorophylls in the exciton model of Photosystem I. Photosynthesis Research 86, 185-201 (2005). doi:10.1007/s11120-005-2747-x.

[59] Behrendt, L. et al. Chlorophyll f-driven photosynthesis in a cavernous cyanobacterium. ISME J. 9, 2108–2111 **(2015)**

[60] Gisriel, C. J., Wang, J., Brudvig, G. W., & Bryant, D. A.Opportunities and challenges for assigning cofactors in cryo-EM density maps of chlorophyll-containing proteins. Communications Biology, 3, 1-10 **(2020)**.

[61] Yamaoka, T., Satoh, K., and Katoh, S. **1978**, Photosynthetic activities of a thermophilic blue-green alga, Plant Cell Physiol., 19, 943–954.

[62] Honda, D., Yokota, A., and Sugiyama, J. **1999**, Detection of seven major evolutionary lineages in cyanobacteria based on the 16S rRNA gene sequence analysis with new sequences of five marine Synechococcus strains, J. Mol. Evol., 48, 723–739

[63] Zouni, A., Witt, H. T., Kern, J. et al. **2001**, Crystal structure of photosystem II from Synechococcus elongatus at 3.8 A resolution, Nature, 409, 739–743.

[64] Sonoike, K. and Katoh, S. **1989**, Simple estimation of the differential absorption coefficient of P-700 in detergent-treated preparations, Biochim. Biophys. Acta, 976, 210–213.

[65] Katoh, H., Itoh, S., Shen, J. R., and Ikeuchi, M. **2001**, Functional analysis of psbV and a novel c-type cytochrome gene psbV2 of the thermophilic cyanobacterium Thermosynechococcus elongatus strain BP-1, Plant Cell Physiol., 42, 599–607

[66] Nakamura, Y., Kaneko, T., Sato, S., Ikeuchi, M., Katoh, H., Sasamoto, S., ... & Kishida, Y. **(2002)**. Complete genome structure of the thermophilic cyanobacterium Thermosynechococcus elongatus BP-1. DNA research, 9(4), 123-130.

[67] Onai, K., Morishita, M., Itoh, S., Okamoto, K., & Ishiura, M. **(2004)**. Circadian rhythms in the thermophilic cyanobacterium Thermosynechococcus elongatus: compensation of period length over a wide temperature range. Journal of bacteriology, 186(15), 4972-4977.

[68] Los, D. A., & Murata, N. **(2002)**. Sensing and response to low temperature in cyanobacteria (Vol. 3, pp. 139-153). Elsevier Press: Amsterdam, Holland.

[69] Schuergers, N., Lenn, T., Kampmann, R., Meissner, M. V., Esteves, T., Temerinac-Ott, M., ... & Wilde, A. **(2016).** Cyanobacteria use micro-optics to sense light direction. Elife, 5, e12620.

[70] Masoumi, Ava & Heinemann, Ilka & Rohde, Manfred & Koch, Michael & Jahn, Martina & Jahn, Dieter. **(2009)**. Complex formation between protoporphyrinogen IX oxidase and ferrochelatase during haem biosynthesis in Thermosynechococcus elongatus. Microbiology (Reading, England). 154. 3707-14. 10.1099/mic.0.2008/018705-0.

[71] Collins, A. M., Liberton, M., Jones, H. D., Garcia, O. F., Pakrasi, H. B., & Timlin, J. A. **(2012)**. Photosynthetic pigment localization and thylakoid membrane morphology are altered in Synechocystis 6803 phycobilisome mutants. Plant physiology, 158(4), 1600-1609..

[72] Vothknecht, U. C., & Westhoff, P. **(2001)**. Biogenesis and origin of thylakoid membranes. Biochimica et Biophysica Acta (BBA)-Molecular Cell Research, 1541(1-2), 91-101.

[73] Zhao, L. S., Huokko, T., Wilson, S., Simpson, D. M., Wang, Q., Ruban, A. V., ... & Liu, L. N. **(2020)**. Structural variability, coordination and adaptation of a native photosynthetic machinery. Nature Plants, 6(7), 869-882.

[74] Wada, H., & Murata, N. **(1998)**. Membrane lipids in cyanobacteria. In Lipids in photosynthesis: structure, function and genetics (pp. 65-81). Springer, Dordrecht.

[75] Rögner, M., **1990**. Purification of membrane protein complexes isolated from a cyanobacterial thylakoid membrane by high-performance liquid chromatography. Journal of Chromatography A, 512, pp.219-226.

[76] Chitnis, V. P. & Chitnis, P. R. PsaL subunit is required for the formation of photosystem I trimers in the cyanobacterium Synechocystis sp. PCC 6803. FEBS Lett. 336, 330–334 **(1993)**.

[77] Jekow, P. et al. Crystallization of intact and subunit L-deficient monomers from synechocystis PCC 6803 photosystem I. Zeitschrift fur Naturforsch. - Sect. C J. Biosci. 51, 195-199 **(1996)**. doi:10.1515/znc-1996-3-410.

[78] Jekow, P., Fromme, P., Witt, H. T. & Saenger, W. Photosystem I from Synechococcus elongatus: preparation and crystallization of monomers with varying subunit compositions. BBA - Bioenerg. 1229, 115–120 **(1995)**.

[79] El-Mohsnawy, E. et al. Structure and function of intact photosystem 1 monomers from the cyanobacterium thermosynechococcus elongatus. Biochemistry 49, 4740–4751 **(2010)**

[80] Frank, A. **(2018)**. Efficient purification and comparative characterization of the cyanobacterial photosystem I monomer. [Master's thesis] Ruhr University Bochum

[81] Kendrew, J. C., Bodo, G., Dintzis, H. M., Parrish, R. G., Wyckoff, H., & Phillips, D. C. **(1958)**. A three-dimensional model of the myoglobin molecule obtained by X-ray analysis. Nature, 181(4610), 662-666.

[82] Deisenhofer, J., Epp, O., Miki, K., Huber, R., & Michel, H. **(1985)**. Structure of the protein subunits in the photosynthetic reaction centre of Rhodopseudomonas viridis at 3Å resolution. Nature, 318(6047), 618-624.

[83] Newby, Z. E., D O'Connell, J., Gruswitz, F., Hays, F. A., Harries, W. E., Harwood, I. M., ... & Stroud, R. M. **(2009)**. A general protocol for the crystallization of membrane proteins for X-ray structural investigation. Nature protocols, 4(5), 619-637.

[84] Marchesi, V. T. **(1985)**. Stabilizing infrastructure of cell membranes. Annual review of cell biology, 1(1), 531-561.

[85] Gerle, C. **(2019)**. Essay on Biomembrane Structure. The Journal of membrane biology, 252(2-3), 115-130.

[86] Jan, B. F. N. **(1993)**. Polymer–micelle interactions: physical organic aspects. Chemical Society Reviews, 22(2), 85-92.

[87] Womack, M. D., Kendall, D. A., & MacDonald, R. C. **(1983)**. Detergent effects on enzyme activity and solubilization of lipid bilayer membranes. Biochimica et Biophysica Acta (BBA)-Biomembranes, 733(2), 210-215.

[88] Chayen, N. E., & Saridakis, E. **(2008)**. Protein crystallization: from purified protein to diffraction-quality crystal. Nature methods, 5(2), 147-153.

[89] Boistelle, R., & Astier, J. P. **(1988)**. Crystallization mechanisms in solution. Journal of Crystal Growth, 90(1-3), 14-30.

[90] Gisriel, C., Coe, J., Letrun, R., Yefanov, O. M., Luna-Chavez, C., Stander, N. E., ... & Grant, T. D. **(2019)**. Membrane protein megahertz crystallography at the European XFEL. Nature communications, 10(1), 1-11.

[91] Ben-Shem, A., Frolow, F., & Nelson, N. **(2003)**. Crystal structure of plant photosystem I. Nature, 426(6967), 630-635.

[92] Mazor, Y., Nataf, D., Toporik, H., & Nelson, N. **(2014)**. Crystal structures of virus-like photosystem I complexes from the mesophilic cyanobacterium Synechocystis PCC 6803. Elife, 3, e01496.

[93] Brunger, A. T., Adams, P. D., Fromme, P., Fromme, R., Levitt, M., & Schröder, G. F. **(2012)**. Improving the accuracy of macromolecular structure refinement at 7 Å resolution. Structure, 20(6), 957-966.

[94] Chapman, H. N., Fromme, P., Barty, A., White, T. A., Kirian, R. A., Aquila, A., ... & Doak, R. B. **(2011)**. Femtosecond X-ray protein nanocrystallography. Nature, 470(7332), 73-77.

[95] Antoshvili, M., Caspy, I., Hippler, M., & Nelson, N. **(2019)**. Structure and function of photosystem I in Cyanidioschyzon merolae. Photosynthesis research, 139(1-3), 499-508.

[96] Mazor, Y., Borovikova, A., & Nelson, N. **(2015)**. The structure of plant photosystem I super-complex at 2.8 Å resolution. Elife, 4, e07433.

[97] Amunts, A., Drory, O., & Nelson, N. **(2007)**. The structure of a plant photosystem I supercomplex at 3.4 Å resolution. Nature, 447(7140), 58-63.

[98] Mazor, Y., Borovikova, A., Caspy, I., & Nelson, N. **(2017)**. Structure of the plant photosystem I supercomplex at 2.6 Å resolution. Nature plants, 3(3), 1-9.

[99] Qin, X., Suga, M., Kuang, T., & Shen, J. R. **(2015)**. Structural basis for energy transfer pathways in the plant PSI-LHCI supercomplex. Science, 348(6238), 989-995.

[100] Hope, H., Frolow, F., Von Böhlen, K., Makowski, I., Kratky, C., Halfon, Y., ... & Yonath, A. **(1989)**. Cryocrystallography of ribosomal particles. Acta Crystallographica Section B: Structural Science, 45(2), 190-199.

[101] Ochi, T., Bolanos-Garcia, V. M., Stojanoff, V., & Moreno, A. **(2009)**. Perspectives on protein crystallisation. Progress in Biophysics and Molecular Biology, 101(1-3), 56-63.

[102] Fromme, P. **(2003)**. Crystallization of photosystem I. Methods and results in crystallization of membrane proteins, 147-173.

[103] W. Kabsch, XDS. Acta Crystallogr. D 66, 125–132 **(2010)**

[104] Winn, M. D., Ballard, C. C., Cowtan, K. D., Dodson, E. J., Emsley, P., Evans, P. R., ... & Wilson, K. S. (2011). Overview of the CCP4 suite and current developments. Acta Crystallographica Section D: Biological Crystallography, 67(4), 235-242.

[105] Emsley, P., Lohkamp, B., Scott, W. G., & Cowtan, K. (2010). Features and development of Coot. Acta Crystallographica Section D: Biological Crystallography, 66(4), 486-501.

[106] R. A. Nicholls, F. Long and G. N. Murshudov, Low Resolution Refinement Tools in REFMAC5. Acta Cryst. D 68. 404-417 **(2012)**

[107] Goddard, T. D. et al. UCSF ChimeraX: Meeting modern challenges in visualization and analysis. Protein Sci. 27, 14–25 **(2018)**.

[108] Dühring, U., Ossenbühl, F., & Wilde, A. **(2007)**. Late assembly steps and dynamics of the cyanobacterial photosystem I. Journal of Biological Chemistry, 282(15), 10915-10921.

[109] Hauer, F. et al. GraDeR: Membrane Protein Complex Preparation for Single-Particle Cryo-EM. Structure 23,1769-1775 **(2015)**. doi:10.1016/j.str.2015.06.029.

[110] Shen, P. S. **(2018)**. The 2017 Nobel Prize in Chemistry: cryo-EM comes of age. Analytical and bioanalytical chemistry, 410(8), 2053-2057.

[111] Shampo, M. A., & Kyle, R. A. (1994, June). Sir Aaron Klug—Nobel Prize Winner for Chemistry. In Mayo Clinic Proceedings (Vol. 69, No. 6, p. 556). Elsevier.

[112] Berman, H. M., Westbrook, J., Feng, Z., Gilliland, G., Bhat, T. N., Weissig, H., ... & Bourne, P. E. (2000). The protein data bank. Nucleic acids research, 28(1), 235-242.

[113] Crowther, R. A., DeRosier, D. J., & Klug, A. **(1970)**. The reconstruction of a three-dimensional structure from projections and its application to electron microscopy. Proceedings of the Royal Society of London. A. Mathematical and Physical Sciences, 317(1530), 319-340.

[114] Yin, C. C. **(2018)**. Structural biology revolution led by technical breakthroughs in cryo-electron microscopy. Chinese Physics B, 27(5), 058703.

[115] De Rosier, D. J., & Klug, A. **(1968)**. Reconstruction of three dimensional structures from electron micrographs. Nature, 217(5124), 130-134.

[116] Lyumkis, D. **(2019)**. Challenges and opportunities in cryo-EM single-particle analysis. Journal of Biological Chemistry, 294(13), 5181-5197.

[117] De la Rosa-Trevín, J. M., Quintana, A., Del Cano, L., Zaldivar, A., Foche, I., Gutierrez, J., ... & Vargas, J. **(2016)**. Scipion: A software framework toward integration, reproducibility and validation in 3D electron microscopy. Journal of structural biology, 195(1), 93-99.

[118] Benjin, X., & Ling, L. **(2020)**. Developments, applications, and prospects of cryo‐electron microscopy. Protein Science, 29(4), 872-882..

[119] Russo, C. J., & Passmore, L. A. **(2016)**. Progress towards an optimal specimen support for electron cryomicroscopy. Current opinion in structural biology, 37, 81-89.

[120] Drulyte, I., Johnson, R. M., Hesketh, E. L., Hurdiss, D. L., Scarff, C. A., Porav, S. A., ... & Thompson, R. F. **(2018)**. Approaches to altering particle distributions in cryo-electron microscopy sample preparation. Acta Crystallographica Section D: Structural Biology, 74(6), 560-571.

[121] Fernandez, J. J., Luque, D., Caston, J. R., & Carrascosa, J. L. **(2008)**. Sharpening high resolution information in single particle electron cryomicroscopy. Journal of structural biology, 164(1), 170-175.

[122] Rosenthal, P. B., & Henderson, R. **(2003)**. Optimal determination of particle orientation, absolute hand, and contrast loss in single-particle electron cryomicroscopy. Journal of molecular biology, 333(4), 721-745.

[123] Yip, K. M., Fischer, N., Paknia, E., Chari, A., & Stark, H. **(2020)**. Breaking the next Cryo-EM resolution barrier-Atomic resolution determination of proteins!. BioRxiv.

[124] Frederik, P. M., Stuart, M. C. A., Bomans, P. H. H., Busing, W. M., Burger, K. N. J., & Verkleij, A. J. **(1991)**. Perspective and limitations of cryo‐electron microscopy: From model systems to biological specimens. Journal of microscopy, 161(2), 253-262.

[125] Merk, A., Fukumura, T., Zhu, X., Darling, J. E., Grisshammer, R., Ognjenovic, J., & Subramaniam, S. **(2020)**. 1.8 Å resolution structure of β-galactosidase with a 200 kV CRYO ARM electron microscope. IUCrJ, 7(4).

[126] Zhang, J. et al. JADAS: A customizable automated data acquisition system and its application to ice-embedded single particles. J. Struct. Biol. 165, 1–9 **(2009)**.

[127] Zivanov, J. et al. New tools for automated high-resolution cryo-EM structure determination in RELION-3. Elife 7, p.e42166 **(2018)**. doi:10.7554/eLife.42166.

[128] Punjani, A., Rubinstein, J. L., Fleet, D. J. & Brubaker, M. A. CryoSPARC: Algorithms for rapid unsupervised cryo-EM structure determination. Nat. Methods 14, 290-296 **(2017)**.

[129] Pettersen E.F. et al. UCSF Chimera--a visualization system for exploratory research and analysis. J. Comput. Chem. 25, 1605-1612 **(2004)**

[130] Zheng, S. Q. et al. MotionCor2: Anisotropic correction of beam-induced motion for improved cryo-electron microscopy. Nature Methods 14, 331-332 **(2017)**. doi:10.1038/nmeth.4193.

[131] Rohou, A. & Grigorieff, N. CTFFIND4: Fast and accurate defocus estimation from electron micrographs. J. Struct. Biol. 192, 216–221 **(2015)**.

[132] Kucukelbir, A., Sigworth, F. J. & Tagare, H. D. Quantifying the local resolution of cryo-EM density maps. Nat. Methods 11, 63–65 **(2014)**.

[133] Liebschner, D. et al. Macromolecular structure determination using X-rays, neutrons and electrons: Recent developments in Phenix. Acta Crystallogr. Sect. D Struct. Biol. **(2019)** doi:10.1107/S2059798319011471.

[134] Smart, O.S., Horský, V., Gore, S., Svobodová Vařeková, R., Bendová, V., Kleywegt, G.J. and Velankar, S. Validation of ligands in macromolecular structures determined by X-ray crystallography. Acta Crystallographica Section D: Structural Biology, 74 (3), 228-236 **(2018)**.

[135] Moriarty, N. W. & Adams, P. D. Iron–sulfur clusters have no right angles. Acta Crystallogr. Sect. D Struct. Biol. 75, 16–20 **(2019)**.

[136] O. S. Smart, T. O. Womack, A. Sharff, C. Flensburg, P. Keller, W. Paciorek, C. Vonrhein, and G. Bricogne.**(2011)** grade, version] /1.2.19/ Cambridge, United Kingdom, Global Phasing Ltd.,http://www.globalphasing.com

[137] Suga, M., Ozawa, S. I., Yoshida-Motomura, K., Akita, F., Miyazaki, N., & Takahashi, Y. **(2019)**. Structure of the green algal photosystem I supercomplex with a decameric light-harvesting complex I. Nature plants, 5(6), 626-636.

[138] E.Krissinel and K.Henrick **(2004)**, Acta Cryst. D60, 2256-2268 Secondary-structure matching (SSM), a new tool for fast protein structure alignment in three dimensions

[139] Schluchter, W. M., Shen, G., Zhao, J. & Bryant, D. A. Characterization of psaI and psaL Mutants of Synechococcus sp. Strain PCC 7002: A New Model for State Transitions in Cyanobacteria. Photochem. Photobiol. 64, 53–66 **(1996)**

[140] Franck, J. **(1958)**. Remarks on the long-wave-length limits of photosynthesis and chlorophyll fluorescence. Proceedings of the National Academy of Sciences of the United States of America, 44(9), 941.

[141] Croce, R., & van Amerongen, H. **(2020)**. Light harvesting in oxygenic photosynthesis: Structural biology meets spectroscopy. Science, 369(6506).

[142] Elli, A. F. et al. Red pool chlorophylls of photosystem I of the cyanobacterium Thermosynechococcus elongatus: A single-molecule study. Biochemistry 45, 1454–1458 **(2006)**.

[143] Gobets, B. et al. Time-resolved fluorescence emission measurements of photosystem I particles of various cyanobacteria: A unified compartmental model. Biophys. J. 81, 407–424 **(2001)**

[144] Damjanović, A., Vaswani, H. M., Fromme, P. & Fleming, G. R. Chlorophyll excitations in photosystem I of Synechococcus elongatus. J. Phys. Chem. B 106, 10251–10262 **(2002)**.

[145] Sener, M. K. et al. Robustness and optimality of light harvesting in cyanobacterial photosystem I. J. Phys. Chem. B 106, 7948–7960 **(2002)**.

[146] Byrdin, M. et al. Light harvesting in photosystem I: Modeling based on the 2.5-Å structure of photosystem I from Synechococcus elongatus. Biophys. J. 83, 433–457 **(2002)**.

[147] Yang, M., Damjanović, A., Vaswani, H. M. & Fleming, G. R. Energy transfer in photosystem I of cyanobacteria Synechococcus elongatus: Model study with structure-based semi-empirical Hamiltonian and experimental spectral density. Biophys. J. 85, 140-158 **(2003)**. doi:10.1016/S0006-3495(03)74461-0.

[148] Gobets, B., van Stokkum, I. H. M., van Mourik, F., Dekker, J. P. & van Grondelle, R. Excitation Wavelength Dependence of the Fluorescence Kinetics in Photosystem I Particles from Synechocystis PCC 6803 and Synechococcus elongatus. Biophys. J. 85, 3883–3898 **(2003)**.

[149] Brüggemann, B., Sznee, K., Novoderezhkin, V., Van Grondelle, R. & May, V. From structure to dynamics: Modeling exciton dynamics in the photosynthetic antenna PS1. J. Phys. Chem. B 108, 13536–13546 **(2004)**

[150] Balaban, T. S. Are syn-ligated (bacterio)chlorophyll dimers energetic traps in light-harvesting systems? FEBS Lett. 545, 97–102 **(2003)**

[151] Schlodder, E., Shubin, V. V., El-Mohsnawy, E., Roegner, M. & Karapetyan, N. V. Steady-state and transient polarized absorption spectroscopy of photosytem I complexes from the cyanobacteria Arthrospira platensis and Thermosynechococcus elongatus. Biochim. Biophys. Acta - Bioenerg. 1767, 732–741 **(2007)**.

[152] Shibata, Y., Yamagishi, A., Kawamoto, S., Noji, T. & Itoh, S. Kinetically distinct three red chlorophylls in photosystem i of thermosynechococcus elongatus revealed by femtosecond time-resolved fluorescence spectroscopy at 15 K. J. Phys. Chem. B 114, 2954–2963 **(2010)**.

[153] Pishchalnikov, R. Y., Shubin, V. V. & Razjivin, A. P. Spectral differences between monomers and trimers of photosystem I depend on the interaction between peripheral chlorophylls of neighboring monomers in trimer. Phys. Wave Phenom. 25, 185-195 **(2017)**. doi:10.3103/S1541308X17030050.

[154] Werst, M., Jia, Y., Mets, L. & Fleming, G. R. Energy transfer and trapping in the photosystem I core antenna. A temperature study. Biophys. J. 61, 868–878 **(1992)**. doi:10.1016/S0006-3495(92)81894-5.

[155] Laible, P. D., Zipfel, W. & Owens, T. G. Excited state dynamics in chlorophyll-based antennae: the role of transfer equilibrium. Biophys. J. 66, 844–860 **(1994)**.

[156] Klug, D. R., Giorgi, L. B., Crystall, B., Barber, J., & Porter, G. **(1989)**. Energy transfer to low energy chlorophyll species prior to trapping by P700 and subsequent electron transfer. Photosynthesis research, 22(3), 277-284.

[157] Nelson, N., & Yocum, C. F. **(2006)**. Structure and function of photosystems I and II. Annu. Rev. Plant Biol., 57, 521-565.

[158] Cohen, R. O., Shen, G., Golbeck, J. H., Xu, W., Chitnis, P. R., Valieva, A. I., ... & Stehlik, D. **(2004)**. Evidence for asymmetric electron transfer in cyanobacterial photosystem I: analysis of a methionine-to-leucine mutation of the ligand to the primary electron acceptor A0. Biochemistry, 43(16), 4741-4754.

[159] Xu, W., Chitnis, P. R., Valieva, A., Van der Est, A., Brettel, K., Guergova-Kuras, M., ... & Zybailov, B. **(2003)**. Electron transfer in cyanobacterial photosystem I II. Determination of forward electron transfer rates of site-directed mutants in a putative electron transfer pathway from A0 through A1 to FX. Journal of Biological Chemistry, 278(30), 27876-27887.

[160] Xu, W., Chitnis, P., Valieva, A., Van der Est, A., Pushkar, Y. N., Krzystyniak, M., ... & Zybailov, B. **(2003)**. Electron Transfer in Cyanobacterial Photosystem I I. PHYSIOLOGICAL AND SPECTROSCOPIC CHARACTERIZATION OF SITE-DIRECTED MUTANTS IN A PUTATIVE ELECTRON TRANSFER PATHWAY FROM A0 THROUGH A1 TO FX. Journal of Biological Chemistry, 278(30), 27864-27875.

[161] Poluektov, O. G., Paschenko, S. V., Utschig, L. M., Lakshmi, K. V., & Thurnauer, M. C. **(2005)**. Bidirectional electron transfer in photosystem I: direct evidence from high-frequency time-resolved EPR spectroscopy. Journal of the American Chemical Society, 127(34), 11910-11911.

[162] Kouřil, R., Yeremenko, N., D'Haene, S., Oostergetel, G. T., Matthijs, H. C., Dekker, J. P., & Boekema, E. J. **(2005)**. Supercomplexes of IsiA and photosystem I in a mutant lacking subunit PsaL. Biochimica et Biophysica Acta (BBA)-Bioenergetics, 1706(3), 262-266.

[163] Toporik, H., Li, J., Williams, D., Chiu, P. L., & Mazor, Y. **(2019)**. The structure of the stress-induced photosystem I–IsiA antenna supercomplex. Nature Structural & Molecular Biology, 26(6), 443-449.

[164] Pishchalnikov, R. Y., Shubin, V. V., & Razjivin, A. P. **(2020)**. The role of vibronic modes in formation of red antenna states of cyanobacterial PSI. Photosynthesis Research, 1-12.

[165] Frank, J. & Gonzalez, R. L. Structure and Dynamics of a Processive Brownian Motor: The Translating Ribosome. Annu. Rev. Biochem. 79, 381–412 **(2010)**.

[166] Junge, W., Lill, H. & Engelbrecht, S. ATP synthase: An electrochemical transducer with rotatory mechanics. Trends in Biochemical Sciences **(1997)** doi:10.1016/S0968-0004(97)01129-8.

[167] Wittig, I., Braun, H. P., & Schägger, H. **(2006)**. Blue native PAGE. Nature protocols, 1(1), 418.

[168] Schägger, H., & Von Jagow, G. **(1987)**. Tricine-sodium dodecyl sulfate-polyacrylamide gel electrophoresis for the separation of proteins in the range from 1 to 100 kDa. Analytical biochemistry, 166(2), 368-379.

[169] Karapetyan, N. V., Bolychevtseva, Y. V., Yurina, N. P., Terekhova, I. V., Shubin, V. V., & Brecht, M. **(2014)**. Long-wavelength chlorophylls in photosystem I of cyanobacteria: origin, localization, and functions. Biochemistry (Moscow), 79(3), 213-220.

[170] Seddon, A. M., Curnow, P., & Booth, P. J. **(2004)**. Membrane proteins, lipids and detergents: not just a soap opera. Biochimica et Biophysica Acta (BBA)-Biomembranes, 1666(1-2), 105-117.

[171] Timmins, P., Pebay-Peyroula, E., & Welte, W. **(1994)**. Detergent organisation in solutions and in crystals of membrane proteins. Biophysical chemistry, 53(1-2), 27-36.

[172] De Yoreo, J. J., & Vekilov, P. G. **(2003)**. Principles of crystal nucleation and growth. Reviews in mineralogy and geochemistry, 54(1), 57-93.

[173] Sun, C., & Xue, D. **(2017)**. Crystallization: A phase transition process driving by chemical potential decrease. Journal of Crystal Growth, 470, 27-32.

[174] Fujisawa, T., Narikawa, R., Maeda, S. I., Watanabe, S., Kanesaki, Y., Kobayashi, K., ... & Suzuki, E. **(2017)**. CyanoBase: a large-scale update on its 20th anniversary. Nucleic acids research, 45(D1), D551-D554.

[175] Kantardjieff, K. A., & Rupp, B. **(2003)**. Matthews coefficient probabilities: improved estimates for unit cell contents of proteins, DNA, and protein–nucleic acid complex crystals. Protein Science, 12(9), 1865-1871.

[176] Abramavicius, D. & Mukamel, S. Exciton delocalization and transport in photosystem I of cyanobacteria synechococcus elongates: Simulation study of coherent two-dimensional optical signals. J. Phys. Chem. B 113, 6097-108 **(2009)**. doi:10.1021/jp811339p.

[177] Singer, S. J., & Nicolson, G. L. **(1972)**. The fluid mosaic model of the structure of cell membranes. Science, 175(4023), 720-731.

[178] Nakane, T., Kotecha, A., Sente, A., McMullan, G., Masiulis, S., Brown, P. M., ... & Yu, L. (2020). Single-particle cryo-EM at atomic resolution. BioRxiv.

[179] Yip, K. M., Fischer, N., Paknia, E., Chari, A., & Stark, H. **(2020)**. Atomic-resolution protein structure determination by cryo-EM. Nature, 1-5.

[180] Santabarbara, S., Kuprov, I., Poluektov, O., Casal, A., Russell, C. A., Purton, S., & Evans, M. C. **(2010)**. Directionality of electron-transfer reactions in photosystem I of prokaryotes: universality of the bidirectional electron-transfer model. The Journal of Physical Chemistry B, 114(46), 15158-15171.

[181] Kölsch, A., C. Radon, M. Golub, A. Baumert, J. Bürger, T. Mielke, F. Lisdat et al. "Current limits of structural biology: The transient interaction between cytochrome c6 and photosystem I." Current Research in Structural Biology 2 **(2020)**: 171-179.

[182] Kruip, Jochen, Navassard V. Karapetyan, Irina V. Terekhova, and Matthias Rögner. "In vitro oligomerization of a membrane protein complex liposome-

based reconstitution of trimeric photosystem I from isolated monomers." Journal of Biological Chemistry 274, no. 26 **(1999)**: 18181-18188.

[183] Domonkos, Ildikó, Przemyslaw Malec, Anna Sallai, László Kovács, Kunihiro Itoh, Gaozhong Shen, Bettina Ughy et al. "Phosphatidylglycerol is essential for oligomerization of photosystem I reaction center." Plant physiology 134, no. 4 **(2004)**: 1471-1478.

[184] Karapetyan, Navassard V., Eberhard Schlodder, Rienk van Grondelle, and Jan P. Dekker. "The long wavelength chlorophylls of photosystem I." In Photosystem I, pp. 177-192. Springer, Dordrecht, **2006**.

[185] Liu, Ji-Feng. "Theoretical reconsideration on the hydrogen bonding and coordination interactions of chlorophyll a in aqueous solution." Journal of Porphyrins and Phthalocyanines 15, no. 03 **(2011)**: 202-210.

[186] Toporik, H., Khmelnitskiy, A., Dobson, Z., Riddle, R., Williams, D., Lin, S., ... & Mazor, Y. (2020). The structure of a red-shifted photosystem I reveals a red site in the core antenna. Nature communications, 11(1), 1-13.

[187] Pintilie, G., Zhang, K., Su, Z., Li, S., Schmid, M.F. and Chiu, W., Measurement of atom resolvability in cryo-EM maps with Q-scores. Nature methods, 17 (3), 328-334 (2020).113, 6097-108 (2009). doi:10.1021/jp811339p.

[188] Nord, M., Webster, R. W., Paton, K. A., McVitie, S., McGrouther, D., MacLaren, I., & Paterson, G. W. (2020). Fast Pixelated Detectors in Scanning Transmission Electron Microscopy. Part I: Data Acquisition, Live Processing, and Storage. Microscopy and Microanalysis, 26(4), 653-666.

[189] Liao, M., Cao, E., Julius, D., & Cheng, Y. (2014). Single particle electron cryo-microscopy of a mammalian ion channel. Current opinion in structural biology, 27, 1-7.

[190] Baker, M. R., Fan, G., & Serysheva, I. I. (2015). Single-particle cryo-EM of the ryanodine receptor channel in an aqueous environment. European journal of translational myology, 25(1), 35.

[191] Chen, J., Noble, A. J., Kang, J. Y., & Darst, S. A. (2019). Eliminating effects of particle adsorption to the air/water interface in single-particle cryo-electron microscopy: Bacterial RNA polymerase and CHAPSO. Journal of structural biology: X, 1, 100005.

[192] Chae, P. S. et al. A new class of amphiphiles bearing rigid hydrophobicgroups for solubilization and stabilization of membrane proteins. Chem.- A Eur. J. 18, 9485–9490 (2012).

[193] Mazor, Y., Borovikova A., Greenberg I., Nelson N., Crystal structure of plant Photosystem I at 3 Angstrom resolution, PDB ID: 4RKU, (2014) doi: 10.2210/pdb4rku/pdb

[194] J. Appl. Cryst. (2007). 40, 658-674. Phaser crystallographic software. McCoy, A.J., Grosse-Kunstleve, R.W., Adams, P.D., Winn, M.D., Storoni, L.C., & Read, R.J.

[195] Murshudov, G. N., Skubák, P., Lebedev, A. A., Pannu, N. S., Steiner, R. A., Nicholls, R. A., ... & Vagin, A. A. (2011). REFMAC5 for the refinement of

macromolecular crystal structures. Acta Crystallographica Section D: Biological Crystallography, 67(4), 355-367.

[196] Klug, A., & Crowther, R. A. (1972). Three-dimensional image reconstruction from the viewpoint of information theory. Nature, 238(5365), 435-440.

[197] Retrieval of Crystallographically-Derived Molecular Geometry Information, I. J. Bruno, J. C. Cole, M. Kessler, Jie Luo, W. D. S. Motherwell, L. H. Purkis, B. R. Smith, R. Taylor, R. I. Cooper, S. E. Harris and A. G. Orpen, J. Chem. Inf. Comput. Sci., 44, 2133-2144, 2004 [DOI: 10.1021/ci049780b]

[198] Engel, B. D., Schaffer, M., Cuellar, L. K., Villa, E., Plitzko, J. M., & Baumeister, W. (2015). Native architecture of the Chlamydomonas chloroplast revealed by in situ cryo-electron tomography. Elife, 4, e04889.

List of **Publications**

Orkun Çoruh, Anna Frank, Hideaki Tanaka, Akihiro Kawamoto, Eithar El-Mohsnawy, Takayuki Kato, Keiichi Namba, Christoph Gerle, Marc M. Nowaczyk & Genji Kurisu, Cryo-EM structure of a functional monomeric Photosystem I from *Thermosynechococcus elongatus* reveals 'red' chlorophyll cluster, *Commnications Biology*, accepted for publication